Time Delays and Microlensing of Gravitationally Lensed Quasars

Karianne Dyrland

Thesis submitted for
Master of Science in Astronomy

Institute of Theoretical Astrophysics
Faculty of Mathematics and Natural Sciences

UNIVERSITY OF OSLO

June 2019

Abstract

The goal of this project was to determine time delays and the effects of microlensing in gravitationally lensed quasars. We have studied two gravitationally lensed quasars. The first is the sextuply cluster-lensed quasar SDSS J2222+2745, and we have measured the time delays between the three brightest images A, B and C. With respect to image A, the measured time delays are $\Delta t_{AB} = -42.44^{+1.44}_{-1.36}$ days, and $\Delta t_{AC} = 696.65^{+2.10}_{-2.00}$ days (95% confidence interval). This provides a significant improvement to existing results and one of the smallest fractional uncertainties measured for a time delay yet (in the AD time delay). We also see strong evidence of gravitational microlensing in both the B and C image, measured with A as a reference.

Secondly, the time delays in the quadruply lensed quasar PS1 J0147+4630 were measured for the first time. The time delays between the four images were found to be $\Delta t_{AB} = -2.21^{+2.08}_{-2.16}$, $\Delta t_{AC} = -5.28^{+2.16}_{-2.22}$ and $\Delta t_{AD} = -170.47 \pm 7.61$ days (95% confidence interval). We also found microlensing effects in all the images, i.e. images BCD with respect to A. The longest time delay is a good candidate for calculating the Hubble constant H_0, and by using the lens model from Shajib et al. (2019) and scaled uncertainties, we found a Hubble constant $H_0 = 79.5 \pm 7.95$ km s^{-1} Mpc^{-1} based on the itme delay measurement.

Acknowledgements

I would like to express my sincerest gratitude to my supervisor Håkon Dahle for guiding me through this project, for all the help and support and for bringing me along on an observing trip to the Nordic Optical Telescope in La Palma, which was a truly unforgettable experience. Furthermore I would like to thank my family for all the support in the world, my friends for keeping me sane and social these past few months, and my partner Trond Haakon for the constant love and encouragement. Finally, I would like express my gratitude towards all the people at the ITA, for including me in your community, and of course thanks to all the other master students for being there with me.

Contents

Abstract **iii**

Acknowledgements **v**

1 Introduction **1**
1.1 A Brief History of Gravitational Lensing 1
1.2 Background and Motivation 3
1.3 Overview 4

2 Theoretical Background **7**
2.1 Gravitational Lens Theory 8
2.1.1 Geometry and the Lens Equation 8
2.1.2 Multiple Images 12
2.2 Time Delays and the Hubble Constant 17
2.2.1 The Time Delay Function 17
2.2.2 Measuring the Hubble Constant 18

3 Data **23**
3.1 Observations 23
3.1.1 SDSS J2222+2745 24
3.1.2 PS1 J0147+4630 26
3.2 Photometry and Data Reduction 27
3.2.1 SDSS J2222+2745 27
3.2.2 PS1 J0147+4630 29

4 Methods **33**
4.1 Structure function 33
4.2 Time Delays 35
4.2.1 Polynomial Method 35
4.2.2 Model selection 37

5 Results **41**
5.1 Structure function 41
5.2 Time Delays and Microlensing 43
5.2.1 Light curve model 44
5.2.2 Model selection 46
5.2.3 Final light curve for SDSS J2222+2745 50
5.2.4 Final light curve for PS1 J0147+4630 53

6 Discussion **57**

7 Conclusion **63**

Bibliography **67**

A Photometry **81**

Chapter 1

Introduction

1.1 A Brief History of Gravitational Lensing

The idea that gravity has the ability to bend light was first suggested as early as 1704 by Isaac Newton himself. One hundred years later, von Soldner (1804) was the first to calculate the deflection angle a star would experience being deflected by the Sun. Another 100 years passed and Einstein (1911) confirmed Soldner's calculations using the equivalence principle. A few years later, Einstein (1915) revisited this and applied the full field equations of his new theory of General Relativity to the problem and found an angle twice as large, due to the curvature of the metric. During the total solar eclipse of May 1919, Eddington and Dyson launched an expedition to measure the deflection angle of the stars close to the Sun, if any, and determine whether light was influenced by gravity, either by Newtonian gravity or Einsteins relativity, or had no effect at all (Dyson et al., 1920). They proved that the deflection angle coincided well with Einstein's predictions and it became an immediate proof of General Relativity. The results was on the front pages everywhere and made Einsteins theory world-famous. An illustration of the deflection of star-light by the gravity of the Sun is shown in figure 1.1.

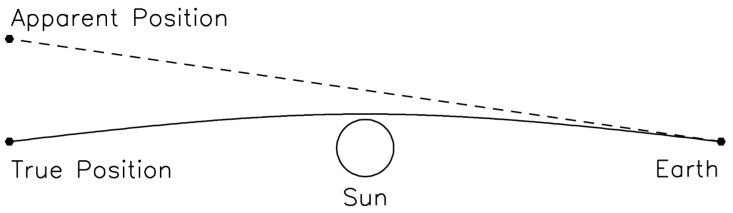

Figure 1.1: Angular deflection of a star by the Sun (Fig.1 in Narayan and Bartelmann (1996).)

Eddington (1920), Einstein (1936) and several other physicists had speculated that light from a distant source might travel around the star along multiple paths, and therefore appear as several images. Although they all agreed this *gravitational lensing* was practically impossible to observe due to the small angular separation between the images. Fritz Zwicky proposed that galaxies (or nebulae as they were known) would be massive enough to produce images at an observable angle, as well as act as a "cosmic telescope" and magnify distant sources (Zwicky, 1937a,b). The Norwegian astrophysicist Sjur Refsdal was a pioneer in the field on gravitational lensing. He suggested a practical application of the phenomenon by measuring the time delays between the images of a variable source and using them to constrain the expansion rate of the universe, i.e. the Hubble constant H_0 (Refsdal, 1964a,b). This became a much more promising task with the discovery of quasars (Schmidt, 1963), as they are very bright, point-like sources, and visible at cosmological distances giving them a great chance of being gravitationally lensed by foreground objects. Eventually, the first gravitationally lensed quasar QSO 0957+561 was discovered by Walsh et al. (1979) 16 years later. It can be seen as a double image formed by a massive foreground galaxy, and is known as the "Twin quasar".

Gravitational lensing has evolved to become a powerful tool in astrophysics and cosmology, Narayan and Bartelmann (1996) classify these applications under three broad categories: 1) The "cosmic telescope effect" magnifies dis-

tant objects and allow us to observe objects that are normally too distant or too faint to be within the resolution-limit of current telescopes. 2) It allows us to study the growth and structure of mass condensations in the universe, as it is independent of luminosity or composition and relies merely on the projected, two-dimensional mass distribution of the lens. 3) Through gravitational lensing and the time delays between quasar images, we can constrain several cosmological parameters: the Hubble constant H_0, the cosmological constant Λ, and the density parameters Ω.

The Hubble constant describes the expansion rate of the universe today and is an important parameter in cosmological models. It is defined through Hubble's law (see eq.(2.28)), which relates the recession velocity of distant objects to their distances. To measure H_0, an accurate method for determining cosmological distances is needed.

1.2 Background and Motivation

The applications of the time delay between multiple quasar images are of particular interest, as they provide a direct way of calculating cosmological distances and the Hubble constant (Refsdal, 1964b), and if we already know H_0 from other sources, we can constrain the mass density profile of the lensing galaxy or cluster Refsdal (2004). For this to be useful, we need accurately determined time delays with small fractional uncertainties. This requires images with either very long (> 150 days) time delays, very active quasars (i.e. highly variable), or a very having been monitored for a very long time (decades).

There are currently about 200 quasars that are known to be gravitationally lensed by galaxies (see https://www.ast.cam.ac.uk/ioa/research/lensedquasars/). However, we only know of four that are lensed by galaxy clusters, proving this is an remarkably rare phenomenon. The first two cases were SDSS J1004+4112 (Inada et al., 2003) and SDSS J1029+2623 (Inada et al., 2006). A third was discovered by Dahle et al. (2013); the sextuply lensed quasar

SDSS J2222+2745. And a fourth, SDSS J0909+4449 with three images, was newly discovered by Shu et al. (2018).

We will study two quasars in this project, that are being regularly monitored by the *Nordic Optical Telescope* (NOT). The first is the sextuply cluster-lensed quasar SDSS J2222+2745, mentioned above, where the three brightest images have been monitored for almost a decade, and still have significant uncertainties in their time delay estimates (Dahle et al., 2015). At least one of the images has a very long time delay, and the quasar is assumed to be highly variable. Meaning it provides an excellent candidate for a very accurate time delay measurement. The other is a quadruply lensed quasar PS1 J0147+4630, who's time delays have never been measured. It was discovered only two years ago by Berghea et al. (2017) and is the brightest multiply lensed quasar known so far. Recent predictions for the time delays done by Shajib et al. (2019) show that it should have at least one long time delay. The lens is a single galaxy, meaning accurately determined time delays in this system would provide an outstanding opportunity to measure the Hubble constant with small uncertainties, once we have a good lens model.

1.3 Overview

In this work our goal is to produce accurate time delay measurements of the two multiply imaged quasar systems SDSS J2222+2745 and PS1 J0147+4630, by utilizing the Legendre polynomial method by Kochanek et al. (2006). This technique models the intrinsic light curve of the quasar from photmetric data, while simultaneously measuring the relative microlensing effects seen in the individual images. Both our target quasars are estimated to have at least one long time delay (> 150 days), which will result in time delay measurements with small fractional uncertanties. Accurate time delays are crucial in determining the Hubble constant using the method demonstrated by Refsdal (1964b), and for constraining the mass density profile of the lens (e.g. Refsdal, 2004). Modeling the microlensing variations will both give us more

precise time delay determination, as they can significantly affect the time delays (Tie and Kochanek, 2018), and be used to estimate the mass of compact objects, as well as well as constrain the fraction of dark matter made up from these sources Press and Gunn (1973).

Chapter 2 describes the theoretical formalism of gravitational lensing, and Chapter 3 summarizes the monitoring campaigns of the quasars, as well as the photometric data reduction of the light curves. The results of the project are presented in Chapter 5 with a discussion following in Chapter 6. The conclusion and possible future prospects are given in Chapter 7.

Chapter 2

Theoretical Background

Gravitational lensing descibes a complicated physical system where the effect of general relativity merges with local perturbations. Lucky for us, we can usually assume an overall geometry that is described by the Friedmann-Lemaître-Robertson-Walker metric. The FLRW-metric is the solution to Einstein's field equations describing a universe adhering to the *cosmological principle*, which states that the universe is homogeneous and isotropic everywhere on large scales; meaning there is no preferred place in the universe. A light ray travels through unperturbed space and encounters an inhomogeneity local to the lens, after, it again follows an unperturbed path. Close to the lens, we can assume a locally flat, Minkowski spacetime weakly perturbed by a Newtonian gravitational potential caused by the mass distribution of the lens. This is valid for a small Newtonian potential, $\Phi \ll c^2$, and a small peculiar velocity of the lens, $v \ll c$. In almost all astrophysical cases of interest, these conditions are satisfied.

This chapter offers some basics and formalism of gravitational lensing, the formation of multiple images and their associated time delays. For more thorough reviews see the works by Refsdal and Surdej (1994); Narayan and Bartelmann (1996); Courbin et al. (2002) and Eigenbrod (2012). A discussion on the Hubble constant based on the method introduced by Refsdal (1964a) also follows.

2.1 Gravitational Lens Theory

2.1.1 Geometry and the Lens Equation

Deflection Angle

A ray of light propagating through a gravitational potential can be described in terms of a refractive index n (e.g. Schneider et al., 1992), given by

$$n = 1 - \frac{2}{c^2}\Phi = 1 + \frac{2}{c^2}|\Phi| \tag{2.1}$$

where Φ is the Newtonian potential, and c is the speed of light in vacuum. A refractive index $n > 1$ results in a slower traveling time for light passing through, just as with normal optics. The speed of light reduces to

$$v = \frac{c}{n} \simeq c - \frac{2}{c}|\Phi| \tag{2.2}$$

The effects are similar to a ray of light traveling through a glass prism. The reduced speed causes light rays to deflect, and will cause a delay in the arrival time relative to light traveling free through vacuum. The resulting gravitational time delay is given by the *Shapiro delay* (Shapiro, 1964),

$$\Delta t = \int_{\text{source}}^{\text{observer}} \frac{2}{c^3}|\Phi| dl \tag{2.3}$$

where we integrate over the light path from the source to the observer. We get the deflection angle of the light rays when integrating over the path of the gradient of n, perpendicular to the path of travel,

$$\overrightarrow{\hat{\alpha}} = -\int \vec{\nabla}_\perp n \; dl = \frac{2}{c^2}\int \vec{\nabla}_\perp \Phi \; dl. \tag{2.4}$$

This deflection given by equation (2.4) is usually very small, hence we can use

the small angle approximation. We can then integrate along an unperturbed path instead of along the deflected ray; the unperturbed path is represented by the dotted line, at $\angle\beta$, in figure 2.1.

Thin Screen Approximation

The lens itself is can also be considered thin, compared to the cosmological distances of the total path between the observer and lens, and between the lens and source. We can therefore project the mass distribution of the lens along the line-of-sight, in a plane perpendicular to the observer's line-of-sight (Narayan and Bartelmann, 1996). This is commonly called the *lens plane* and a visual representation can be seen in figure 2.1.

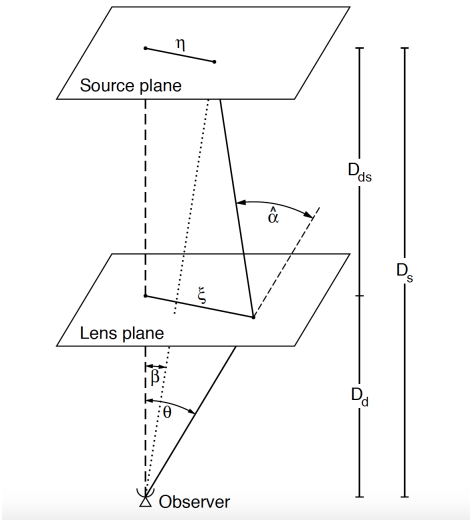

Figure 2.1: A light ray path that intersects the lens plane at $\vec{\xi}$. The angle β represents the unperturbed path, and $\angle\theta$ the source's apparent position. $\vec{\hat{\alpha}}(\vec{\xi})$ is the vector sum of deflection angles from point mass elements in the plane (see Eq.(2.6)). D_d, D_s, and D_{ds} are the angular diameter distances between the observer and lens, the observer and source, and the lens and the source, respectively. (Fig.11 from Bartelmann and Schneider, 2001)

The plane is a sheet of mass characterized by its surface mass density,

$$\Sigma(\vec{\xi}) = \int \rho(\vec{\xi}, z) dz, \tag{2.5}$$

where $\vec{\xi}$ is a two-dimensional vector representing the position where the light ray is deflected, and ρ is the mass density of the lens within the plane.

In the thin screen approximation the lens is made up of an ensemble of point masses with positions $\vec{\xi'}$. The total deflection angle of the light ray at $\vec{\xi}$ is the superposition of the deflection angles from all points,

$$\overrightarrow{\hat{\alpha}}(\vec{\xi}) = \frac{4G}{c^2} \int \frac{\left(\vec{\xi} - \vec{\xi'}\right) \Sigma\left(\vec{\xi'}\right)}{\left|\vec{\xi} - \vec{\xi'}\right|^2} d^2\xi'. \tag{2.6}$$

For the general case the deflection angle is a two-component vector. However, when considering the special case of a circularly symmetric lens, we consider it as a one-dimensional problem (Narayan and Bartelmann, 1996):

$$\hat{\alpha}(\xi) = \frac{4GM(\xi)}{c^2 \xi}, \tag{2.7}$$

where ξ is the distance to the center of symmetry and is called the impact parameter. Note that we can use the Schwarzschild radius,

$$R_{\mathrm{S}} = \frac{2GM}{c^2}, \tag{2.8}$$

to express the deflection angle as twice the inverse of the impact parameter, in units of the Schwarzschild radius (Narayan and Bartelmann, 1996). Equation (2.7) is a good approximation when $\xi \gg R_s$, i.e. we are considering small deflection angles $\hat{\alpha} \ll 1$ rad. This is usually satisfied for astrophysical cases where usually $\hat{\alpha} \sim 1" = 10^{-6}$ rad (Eigenbrod, 2012).

The mass enclosed within the radius ξ is given by

$$M(\xi) = 2\pi \int_0^{\xi} \Sigma\left(\xi'\right) \xi' d\xi'. \tag{2.9}$$

The Lens Equation

The geometry of a gravitational lens system is depicted in figure 2.2. Light rays from a source at a distance D_s pass by a concentration of mass located at D_d, crossing the lens plane at position ξ, and is deflected by the deflection angle $\hat{\alpha}$. Using the small angle approximation, the angular position of this is at $sin\theta \approx \theta = \xi/D_d$, which is also the angle at which an image I is projected. The true position of the source is given by η, and its corresponding angular position $\beta = \eta/D_s$, represents the unperturbed path. D_{ds} is the distance from the source plane to the lens plane.

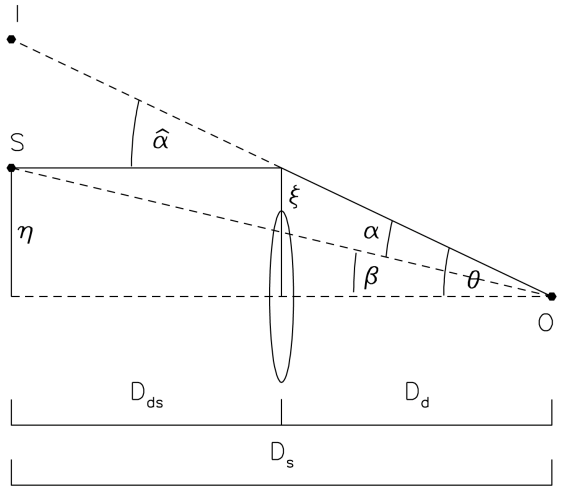

Figure 2.2: Geometry of a gravitational lens system. A light ray travels from a source S, crosses a lensing mass at ξ and is deflected by an angle $\hat{\alpha}$. The deflection corresponds to a change in apparent position by an angle α, seen from the vantage point of O. β gives the angle between the observer and the true position of the source, i.e. the unperturbed path, and θ gives the angle of the apparent position of S, from O, at the image I. D_s, D_d, and D_{ds} are the angular diameter distances between the observer and the source, the observer and the lens, and the lens and the source, respectively. (Fig.5 from Narayan and Bartelmann, 1996)

For convenience we will introduce the reduced deflection angle

$$\vec{\alpha} = \frac{D_{\mathrm{ds}}}{D_{\mathrm{s}}} \overrightarrow{\hat{\alpha}}\,. \tag{2.10}$$

From figure 2.2 and the definitions above we get the *lens equation*

$$\vec{\beta} = \vec{\theta} - \vec{\alpha}(\vec{\theta}), \tag{2.11}$$

which relates the positions of the source and its image. In the general case it is nonlinear, meaning we can have several images of the same source.

2.1.2 Multiple Images

Wavefronts

A more illustrative example of gravitational lensing and how multiple images form can be given in terms of wavefronts. Figure 2.3 shows an illustration of both the different regimes of lensing as well as light represented by propagating waves. They start out spherical and as they travel through a gravitational lens, they get deformed and slow down due to the effects of curvature. An observer will see an deformed image in the direction normal to the wavefront, and if the lens is strong enough, the wavefront will fold in on itself producing multiple images with respective time delays. For variable sources, e.g. quasars, these time delays are measurable with respect to each other and will be proportional to the distances between the folds. This gravitational time delay is the Shapiro delay seen in equation (2.3), and again in equation (2.23).

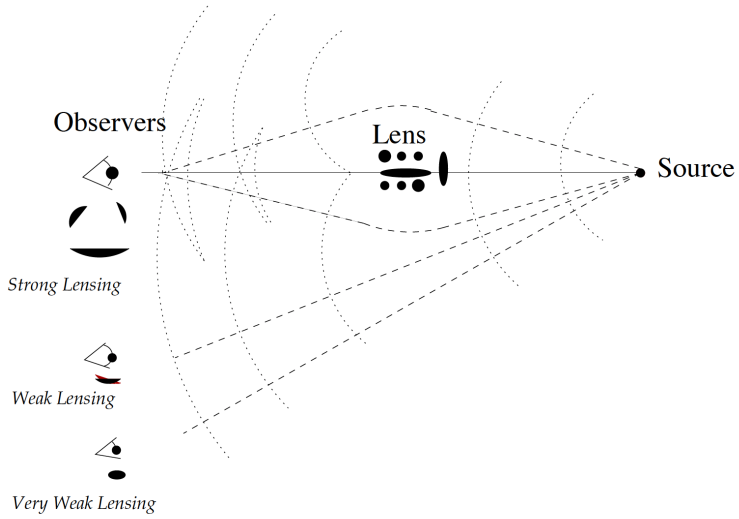

Figure 2.3: Illustration of wavefronts propagating from a background source, and the different regimes of lensing. Lensing by quasars are relevant in the strong regime, while lensed galaxies are important in the weak (Fig.1.1 from Courbin et al., 2002)

The Einstein Radius

For a circularly symmetric lens, the lens equation is given by

$$\beta(\theta) = \theta - \frac{D_{\rm ds}}{D_{\rm d} D_{\rm s}} \frac{4GM(\theta)}{c^2 \theta}, \tag{2.12}$$

where we have used equations (2.7) and (2.10). If we are considering a special case where the observer and the source both lie perfectly on the optical axis, i.e. $\beta = 0$, the rays would deflect symmetrically and produce a ring as seen by the observer. Solving the lens equation gives the radius of the ring

$$\theta_{\rm E} = \left(\frac{4GM\left(\theta_{\rm E}\right)}{c^2} \frac{D_{\rm ds}}{D_{\rm d} D_{\rm s}} \right)^{1/2}, \tag{2.13}$$

which is referred to as the *Einstein radius*. This is a very useful angular scale in other cases as well, as multiple images usually are seen at an angular

radius on the order of $\theta_{\rm E}$. It also represents the boundary where sources are multiply imaged or are only imaged once. From the Einstein radius we get the critical surface mass density,

$$\Sigma_{\rm cr} = \frac{c^2}{4\pi G}\frac{D_{\rm s}}{D_{\rm d}D_{\rm ds}}, \tag{2.14}$$

and *supercritical* lenses, meaning they have a surface mass density $\Sigma > \Sigma_{\rm cr}$, are typically able to produce multiple images of the same source (Narayan and Bartelmann, 1996).

Magnification

Another consequence of gravitational lensing is the magnification of images. The deflection of light from gravitational lenses preserves surface brightness, as a result of Liouville's theorem, but the apparent solid angle of the source changes. The amplification of the total flux recieved is defined as a ratio between the solid angles of the images and the source. Following the circularly symmetric lens, the *magnification* can be written as

$$\mu = \frac{\theta}{\beta}\frac{d\theta}{d\beta}. \tag{2.15}$$

More formally, the general definition is the inverse Jacobian of the transformation matrix between the source and the image or images. In the case of multiple images, the total magnification is the sum of the magnifications from all images (see e.g. Refsdal and Surdej, 1994; Eigenbrod, 2012).

Lensing by a Point Source

The point mass lens is a good representation of stellar sized lenses. For a point mass lens, the lens equation (eq.(2.11) can be rewritten using the Einstein radius (eq. (2.13))

$$\beta = \theta - \frac{\theta_{\rm E}^2}{\theta}. \tag{2.16}$$

Solving the lens equation produces the image positions, here we see that it has two solutions

$$\theta_{\pm} = \frac{1}{2}\left(\beta \pm \sqrt{\beta^2 + 4\theta_{\rm E}^2}\right). \tag{2.17}$$

The result is that a point mass lens will always produce two images of a background source, on either side of the lens. One image lies inside the Einstein radius, and the outer outside. The magnification is given by

$$\mu_{\pm} = \left[1 - \left(\frac{\theta_{\rm E}}{\theta_{\pm}}\right)^4\right]^{-1} = \frac{u^2+2}{2u\sqrt{u^2+4}} \pm \frac{1}{2}, \tag{2.18}$$

where $u = \beta/\theta_{\rm E}$ is the angular separation. Where $\theta_- < \theta_{\rm E}$, $\mu_- < 0$, meaning the magnification inside the ring is negative, while the image outside is positively magnified. The net magnification is the sum of the two, and is typically positive compared to the unlensed source (Narayan and Bartelmann, 1996). The angular separation of the two images is too small to resolve given today's optics, as predicted by Einstein (Einstein, 1936), but the total magnification can still be detected. As a stellar sized lens moves in front of a distant source, it results in a measurable variability, and is what we call *microlensing*. This type of variability was first observed in a multiply imaged quasar, QSO 2237+0305, by Irwin et al. (1989), and has been used to search for *Massive Astrophysical Compact Halo Objects* (MACHOs) (Paczynski, 1986) and determine the microlensing optical depth of the galactic bulge (Paczynski, 1991). It has also been useful in constraining the fraction of dark matter made up of compact masses. If present, they would produce easily observable lensing events, and the lack of evidence for microlensing events puts an upper limit on the matter fraction of compact objects (Press and Gunn, 1973). The lensing by point masses can also significantly affect the

time delay measurements of multiply imaged distant quasars (e.g. Tie and Kochanek, 2018); we will discuss this in more detail in following chapters.

Lensing by a Singular Isothermal Sphere

Another common lens model is the singular isothermal sphere, which is a good zeroth-order model for giant elliptical galaxies. It assumes the mass components all behave like the particles in an ideal gas with a combined gravitational potential. The Einstein Radius for an isothermal sphere is given by

$$\theta_{\mathrm{E}} = 4\pi \frac{\sigma_v^2}{c^2} \frac{D_{\mathrm{ds}}}{D_{\mathrm{s}}} = \hat{\alpha} \frac{D_{\mathrm{ds}}}{D_{\mathrm{s}}} = \alpha, \tag{2.19}$$

where σ_v^2 is the one-dimensional velocity dispersion of the stars in the sphere. If the background source lies within the Einstein radius, i.e. $\beta < \theta_{\mathrm{E}}$, in reference to the observers line-of-sight, we get multiple images. The equation then has two solutions

$$\theta_{\pm} = \beta \pm \theta_{\mathrm{E}}, \tag{2.20}$$

where the source, the images and the lens, lie on a straight line. The magnification of the images are given by

$$\mu_{\pm} = \frac{\theta_{\pm}}{\beta} = 1 \pm \frac{\theta_{\mathrm{E}}}{\beta} = \left(1 \mp \frac{\theta_{\mathrm{E}}}{\theta_{\pm}}\right)^{-1}. \tag{2.21}$$

If $\beta > \theta_{\mathrm{E}}$, the source lies outside the Einstein ring and we only get one image at $\theta = \theta_+ = \beta + \theta_{\mathrm{E}}$.

Because the lens, in this model, has no ellipticity, it can not produce *quads* (quadruple images). Adding some amount of ellipticity will solve this and also reproduce other configurations we observe (Courbin et al., 2002).

Refsdal (1964a) was the first to propose the method of measuring the time delays between the split images of variable sources (e.g. quasars), and using them to determine the Hubble constant in an independent way.

2.2 Time Delays and the Hubble Constant

2.2.1 The Time Delay Function

As light propagates through space, it travels at a finite velocity. The time it takes to reach an observer depends on the path the ray follows, which will differ depending on whether or not it has been gravitationally lensed. Cooke and Kantowski (1975) derived the time delay expression between lensed and unlensed sources and showed that this time delay is caused by two effects. The first is the *geometric* time delay, Δt_{geom}, which arises due to the fact that a light ray that has been bent will be longer than an unbent ray, and therefore travel farther. The delay is given by

$$c\Delta t_{geom} = (1 + z_d)\ \frac{D_d D_s}{D_{ds}}(\boldsymbol{\theta} - \boldsymbol{\beta})^2, \tag{2.22}$$

where z_d is the redshift of the lens. The second effect is the *gravitational* time delay, Δt_{grav}, which is known as the Shapiro delay (seen in eq.(2.3)). This is the effect caused by traveling through a gravitational potential and a light ray experiences a general relativistic time dilation, given by

$$c\Delta t_{grav} = -(1 + z_d)\ \hat{\psi}(\boldsymbol{\xi}) + \text{constant}. \tag{2.23}$$

where $\hat{\psi}(\boldsymbol{\xi})$ is the deflection potential (see Eigenbrod, 2012) The total time delay is then the sum of the two,

$$c\Delta t = (1 + z_d)\ \frac{D_d D_s}{D_{ds}}\left(\frac{1}{2}(\boldsymbol{\theta} - \boldsymbol{\beta})^2 - \psi(\boldsymbol{\theta})\right) + \text{constant}. \tag{2.24}$$

where $\psi(\boldsymbol{\theta})$ is the scaled deflection potential. As equation (2.24) measures the delay between source and image, it can not be measured because the source is unobservable. We can instead measure the relative time delay between two quasar images, A and B

$$\Delta t_B - \Delta t_A = \frac{(1+z_d)}{c}\,\frac{D_d D_s}{D_{ds}}\left(\frac{1}{2}(\boldsymbol{\theta}_B-\boldsymbol{\beta})^2\frac{1}{2}(\boldsymbol{\theta}_A-\boldsymbol{\beta})^2 - \psi_B(\boldsymbol{\theta}) + \psi_A(\boldsymbol{\theta})\right) \tag{2.25}$$

The equation depends on the angular diameter distances, which themselves depend on the redshift of the source and the lens, z_s and z_d respectively, the Hubble constant H_0, and the assumed cosmology of the universe through the relation (Fukugita et al., 1992),

$$D\left(z_s, z_d\right) = \frac{c}{H_o}\frac{1}{(1+z_d)}\int_{z_s}^{z_d}\frac{dz}{\left[\Omega_M(1+z)^3+\Omega_\Lambda\right]^{1/2}} \tag{2.26}$$

where the cosmological parameters are defined

$$\Omega_{\mathrm{M0}} \equiv \frac{8\pi G\rho_0}{3H_0^2}, \qquad \Omega_{\Lambda 0} \equiv \frac{\Lambda c^2}{3H_0^2} \tag{2.27}$$

The most interesting relation is that the time delays in equation **??** are directly proportional to H_0^{-1} and can therefore give us a direct measure of the Hubble constant (Refsdal, 1964b).

2.2.2 Measuring the Hubble Constant

The expansion of the universe was first observed by Edwin Hubble (1929), who demonstrated the relationship between the recession velocity v_r of nearby galaxies and their distances through the well-known Hubble's law

$$v_r = dH_0 \tag{2.28}$$

where d is the distance to the galaxy and H_0 is the Hubble constant, which states the rate of expansion of the universe today. The Hubble constant is a particularly valuable parameter as it directly relates to cosmological distances. If we are able to determine an accurate H_0, it would provide us with a scale for the universe.

There is not any method that can accurately measure distances at all scales, hence most measurements of cosmological distances make use of a *distance ladder*. A distance ladder is a collection of methods that work progressively on larger scales. Most are based on different distance indicators, usually objects that can be used as "standard candles", which are bright objects of known luminosities, e.g. cepheids and type Ia supernovae (SNIa). Cepheids are bright, young and pulsating stars that have a specific period-luminosity relation, where once we know the period, we can estimate the luminosity distance. This works well for distances in our own galaxy and local galaxies. Cepheids are also one of the few *primary indicators*, and set the zero-base for the distance ladder (Eigenbrod, 2012).

SNIa are white dwarf supernova explosions, which all have a common initial energy due to the Chandrasekhar mass, and hence, a known luminosity. This means we can determine their respective luminosity distances and find H_0 through Hubble's law (eq.2.28). Type Ia supernovae can be seen and used as a distance measure as far as $z \sim 2$ (Eigenbrod, 2012). At larger scales, several relations have been used to estimate luminosity distances, among these are the Tully-Fisher relation (Tully and Fisher, 1977), the Faber-Jackson relation (Faber and Jackson, 1976), and the surface brightness fluctuation method (Tonry and Schneider, 1988). However, all these methods are secondary measurements that rely on calibration through primary indicators, typically cepheids. This results in higher systematic errors as the uncertainties of each distance indicator are added (Eigenbrod, 2012). To constrain this, measurements of cepheids were made using the *Hubble Space Telescope*

to create an accurate local distance scale (Freedman et al., 2001). Recent results are given by Riess et al. (2019).

Other distance indicators are the "standard rulers", a length scale often measured by the baryon acoustic oscillations (BAO) in the early universe (Eisenstein, 2005). Measurements of the acoustic peak signature in the correlation function as a characteristic angle gives us an angular diameter distance as a function of redshift, which yields the Hubble parameter. Galaxy diameters have also been proposed by Marinoni et al. (2008) as a standard ruler. In addition, a single "standard siren" method have been used as a distance indicator, which is the measurement from the gravitational waves of binary neutron stars (The LIGO Scientific Collaboration et al., 2017). Methods that estimate the distances and the Hubble constant without using measured distance indicators include the measurements of the cosmic microwave background (CMB) anisotropies to constrain the cosmological parameters in the ΛCDM model (Planck Collaboration et al., 2018).

A direct way of measuring distances in the universe, and with it the Hubble constant, is through strong gravitational lensing. As discussed above, multiply imaged quasars experience a time delay Δt when passing through a large gravitational potential, which are directly proportional to the inverse Hubble constant H_0^{-1}, as seen in equations (2.24) and (2.26). The method was first proposed by Refsdal (1964b). In order to calculate H_0, two requirements are needed: 1) accurate time delay measurements between the images, which demands observations over a long time span and at an adequate sample rate, 2) an accurate model for the llensing mass distribution of the foreground galaxy, or galaxy cluster causing the lensing. We should also take both microlensing and line-of-sight structure into account, as they can both significantly affect the time delays Tie and Kochanek (2018); Bar-Kana (1996). The measurements may also weakly depend on the cosmological parameters, e.g. the flatness and density parameters, as we see in equation (2.26) (where we assumed a flat universe $\Omega_k = 0$). The estimation of the Hubble constant will be further discussed in chapter 6.

There is a tension between the results of *Planck* and the ones found using

other astrophysical methods, where there is a gap in the final estimates of the Hubble constant. The newest report from *Planck* estimate the Hubble constant to be $H_0 = 67.27 \pm 0.60$ km s^{-1} Mpc^{-1}, while recent distance ladder estimates by Riess et al. (2019) give $H_0 = 74.03 \pm 1.42$ km s^{-1} Mpc^{-1} in the local universe. The current difference between the Hubble constant measured locally by astrophysical methods, and the one inferred by *Planck* CMB and ΛCDM is 6.6 ± 1.5 km s^{-1} Mpc^{-1} (Riess et al., 2019). A figure showing historical measurements of the Hubble constant can be seen in figure 2.4

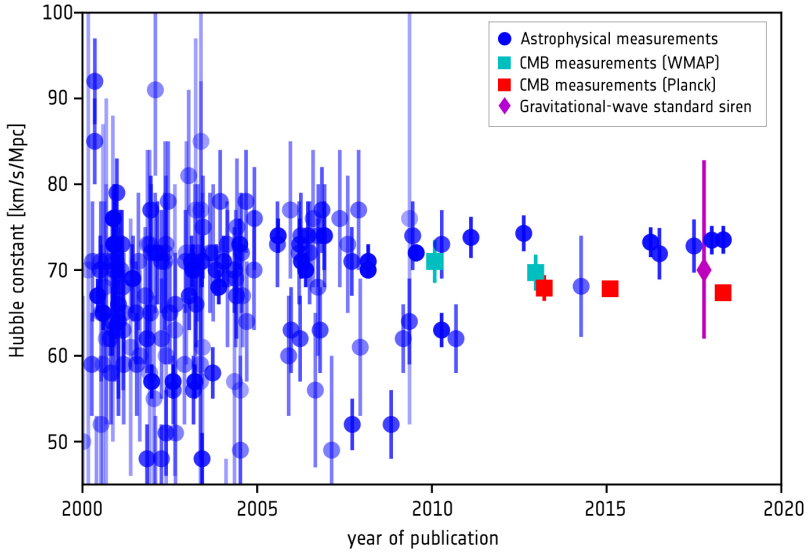

Figure 2.4: Measurements of the Hubble constant over the past two decades. (Credit: ESA and the Planck Collaboration)

Currently, the measurements from all these methods are constrained to the point where there has not yet been found any systematic error than can explain these discrepancies. This has led many to wonder whether we may need to include some new physics in the standard cosmological model(i.e. adding curvature or other dark energy models), for more on this see Planck Collaboration et al. (2018); Rusu et al. (2019) and the references therein.

Chapter 3

Data

The results of this thesis is based on data acquired from monitoring campaigns at the *Nordic Optical Telescope* (hereafter NOT). The projects aim to monitor gravitationally lensed quasars with a high sampling rate over a long time span to be able to measure the time delays between their multiple images. In this project we are interested in the two targets SDSS J2222+2745, a cluster-lensed sextuple quasar, and PS1 J0147+4630, a quad lensed by a massive elliptical galaxy. Both objects have at least one long (> 150 days) time delay, and the time delays of the latter have never been measured before now. This chapters covers the observation and the data reduction techniques used to produce the light curves for our two targets. All data points can be found in tables in Appendix A.

3.1 Observations

NOT is a 2.56 m optical telescope located at the summit of Roque de los Muchachos, La Palma, Canarias, Spain. The observations are made using the *Andalucia Faint Object Spectograph and Camera* (ALFOSC) instrument. It has a 2048×2068 pixel CCD detector with 32 bit intensity resolution, and a pixel scale of $0\farcs2138$ pixel^{-1}. The ALFOSC detector was replaced in 2016,

but the use of calibration stars in the reduction process should account for any dissimilarity in the flux. In the following section, we will discuss the observations of the two target quasars individually.

3.1.1 SDSS J2222+2745

The campaign to monitor SDSS J2222+2745 began in September 2012, after it was discovered by Dahle et al. (2013) through the *Sloan Giant Arcs Survey* (see Sharon et al., 2019, and references therein), which is based on public data from the *Sloan Digital Sky Survey* Blanton et al. (2017). Observational data from September 2012 up until January 2019 makes up the basis of our results. The quasar is located at a redshift $z = 2.8050 \pm 0.0006$ and is split into six distinct images (confirmed so far by Dahle et al., 2013) by a foreground galaxy cluster at $z = 0.4897 \pm 0.0032$ (redshifts measured by Sharon et al., 2017). The images have a maximum angular separation of $15\farcs1$, which is significantly larger than the typical $< 10\farcs$ of quasars lensed by single galaxies. An image of SDSS J2222+2745 from the *Hubble Space Telecope* can be seen in figure 3.1, where the quasar images are marked with arrows and their designated labels.

The three brightest images, A–C, are visible as blue stellar images sharing a clustercentric radius with a giant arc (physically unrelated to the quasar) south of the cluster. The central cluster galaxies are labeled G1–G3, and appear red in the image. Close to the core galaxies we see the three fainter quasar images, D–F. The latter images do not yet have sufficient data for measuring time delays, as their their flux is superimposed to their core galaxy companions and difficult to dissociate. Hence, in this thesis we will be using the data from images A, B and C, as they are sufficiently bright to be observed with ground-based telescopes.

The quasar is monitored in epochs with an average sampling frequency of one every 16.15 days. At each epoch a set of 3×600 second (sometimes 3×300 sec) exposures are captured using the SDSS g-band. This wavelength band is particularly useful for maximizing the signal-to-noise ratio of the blue

quasar images, relative to the redder cluster galaxies, and helps identify the signatures of the fainter D–F images within the superimposed flux. The visibility period of SDSS J2222+2745, i.e. when the target is above the horizon at night time, runs from late April to early January, leaving an average season gap of ~ 117 days for the 7 seasons we currently have.

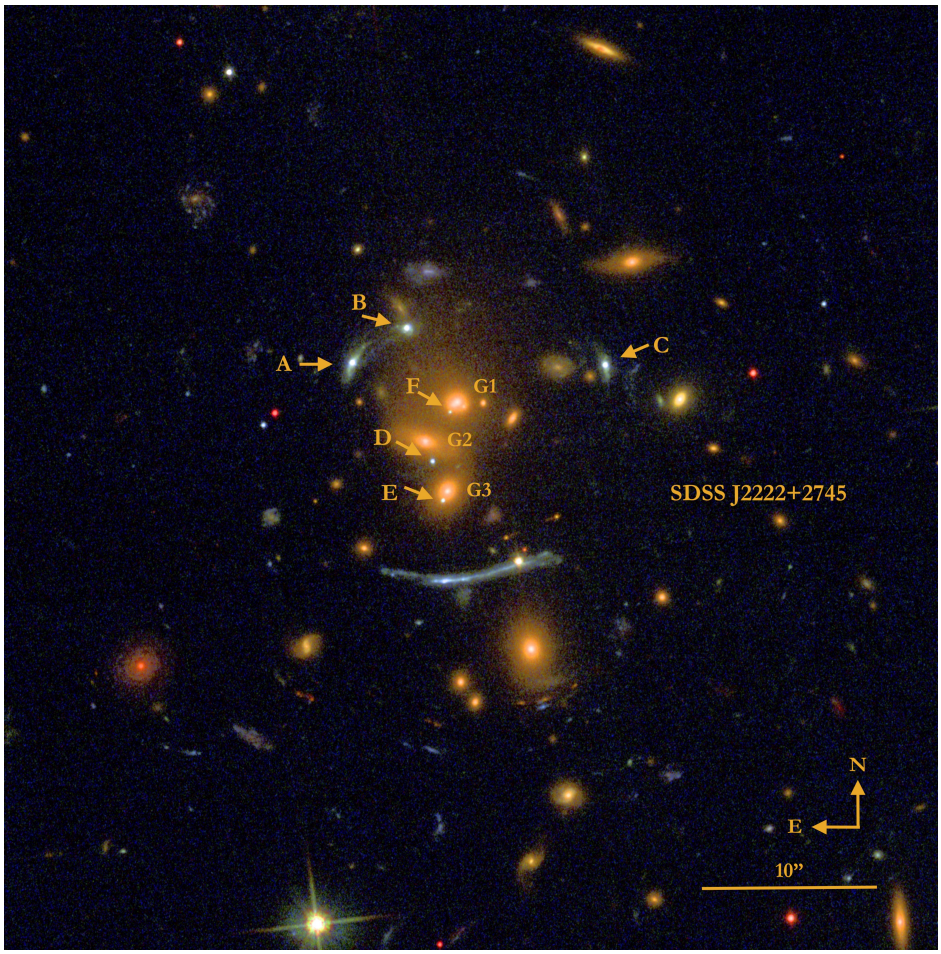

Figure 3.1: *HST* image of SDSS J2222+2745, based on images obtained with the F435W, F606W, and F814W filters of the ACS instrument. The gravitationally lensed quasar images are labeled A–F and the cluster core galaxies are labeled G1–G3. The quasar is at a measured redshift of $z = 2.805$ and the cluster at $z = 0.4897$. Other lensed objects can be seen in the field but are not labeled, the most prominent one being the giant arc south of the cluster core.

In addition to the data from ALFOSC, 3 epochs of data points were captured using the NOT instrument *MOSaic CAmera* (MOSCA), and 3 epochs by the *Gemini North Telescope* using the GMOS instrument. Images from both were acquired using the instruments' respective g-band.

3.1.2 PS1 J0147+4630

Our second target is a quadruple quasar, PS1 J0147+4630, appropriately nicknamed *Andromeda's parachute* due to its configuration. A close-up i-band image from the *Hubble Space Telescope* can be seen at the left-hand of figure 3.2, where the quasar images are lettered A–D, and the lensing galaxy G. A larger-field image from NOT is displayed on the right-hand side outlining the system. Accurate spectroscopic redshifts were measured by Lee (2017, 2018); the quasar is located at $z = 2.341 \pm 0.001$ and the lens at $z = 0.5716 \pm 0.0004$. The maximum angular separation between the four images is $3\farcs8$.

The system marked the first published gravitational lens discovery from the *Panoramic Survey Telescope and Rapid Response System* (Pan-STARRS1, hereafter PS1) images, by Berghea et al. (2017). PS1 is a wide-field imaging system located at the summit of Haleakala on the island of Maui, Hawaii. The first PS1 data were released in December 2016. The campaign to monitor PS1 J0147+4630 at NOT had its first measurement in August 2017. Our results are based on observations from then until March 2019, which marks the end of the second season observed by NOT. It will again be visible at the beginning of June, leaving us a seasonal gap of ~ 75 days. Each epoch consists of a set of 3×30 second exposures with an average sample rate of one epoch every 7.8 days.

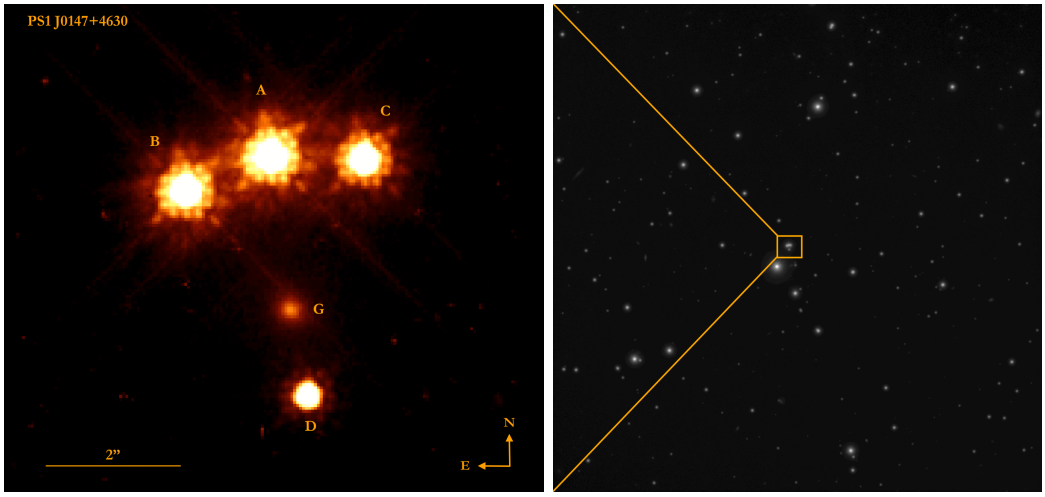

Figure 3.2: Images of PS1 J0147+4630. The quasar images are labeled A–D and the lensing galaxy is named G. The quasar is at a redshift $z = 2.341$ and the lens galaxy at $z = 0.5716$. Left: Close-up image captured by the *Hubble Space Telescope* in September 2017, using the i-band (near infrared) filter F814W. Right: Combined image from the photometric measurements from the *Nordic Optical Telescope*, captured with the ALFOSC instrument in the R-band filter.

3.2 Photometry and Data Reduction

Standard techniques for de-biasing and flat fielding were used on all the ALFOSC photometric data for both quasars, where the flat fields typically are the median of a set of three exposures taken during twilight on the same night as the quasar images. The ALFOSC instrument is cosmetically clean, hence we are able to treat the three exposures from the same epoch as individual measurements, rather than combining the set. In this section, the photometric methods used for each of the quasars will be discussed separately.

3.2.1 SDSS J2222+2745

The data reduction of SDSS J2222+2745 was done by Håkon Dahle following the desciption given in Dahle et al. (2015). The flux of the quasar images and five reference stars were measured using a fixed circular aperture of diameter

2.25", and the uncertainties were determined by measuring the photometric scatter within the exposure's respective epoch, then fitting the result as a function of signal-to-noise of the quasar images. Exposures where FWHM seeing was worse than 1.″2, or where there was a high level of background sky, were excluded. The final sample has 116 epochs and 313 total exposures.

The magnitudes of the quasar images in each exposure were calibrated using SDSS magnitudes of five comparison stars, chosen for their invariability and color match to the quasar. The resulting light curves of images A, B and C of quasar SDSS J2222+2745 can be seen in figure 3.3.

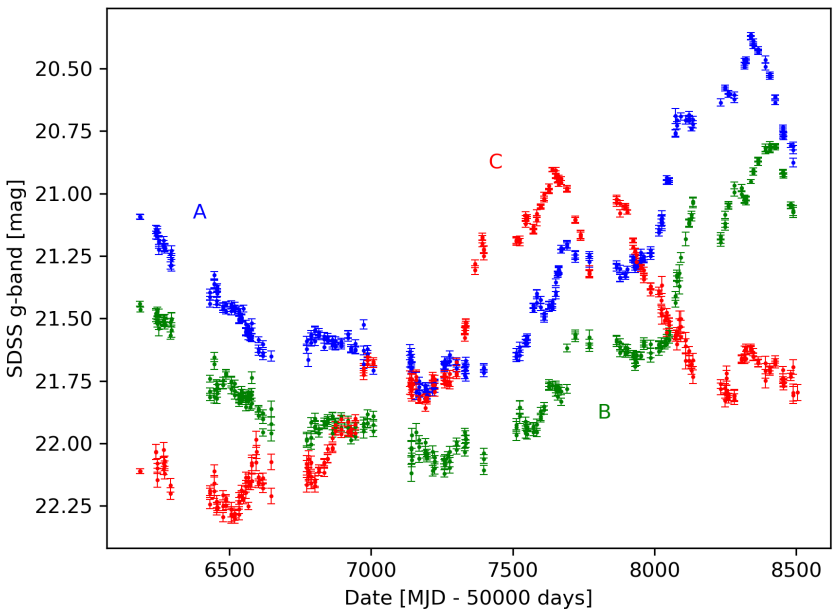

Figure 3.3: Photometric light curves for the three brightest components of the sextuply lensed quasar SDSS J2222+2745. Image A is represented by blue points, image B by green and image C by red. The errorbars show the photometric uncertainties.

The light curves show a significant flux variability over the 7 year time span, and an immediately apparent, time- and magnitude shifted, correlation. By visual inspection, image C seems to be leading image A by approximately 700 days, while image A leads the B component with $\sim 40-50$ days. During the

first 3.5 years (from day 6000-7250 in MJD units) of observations, images A and B are fading, while C is brightening to become the brightest component of the three, while the others experience a minimum. After this images A and B follow a similar trend to that component C had during the first half of the time span, and reach a maximum in 2018 (MJD $\sim$ 8400) similar to the one we saw in image C during the 2016 season (at MJD $\sim$ 7600).

3.2.2 PS1 J0147+4630

The quasar PS1 J0147+4630 contain four images that are located very close together in the field. To be able to separate and measure these individually, we will use the DAOPHOT package in IRAF (see Massey and Davis, 1992) designed for stellar photometry in crowded fields and do a sophisticated point-spread-function (PSF) fitting. Because quasars are bright, point-like sources, they can be fitted well within the PSF profile of a star. The philosophy and the basic algorithms of the DAOPHOT program can be found in Stetson (1987), and a thorough step-by-step guide is given by Massey and Davis (1992).

A few preparing steps were needed before our raw exposures were ready for photometric reduction. The quasar was first centered in the frame of each image using a technique by Håkon Dahle, originally developed for weak lensing photometry. The method uses a large number of reference stars (typically 50-100) in the frame to exactly align the exposures with respect to each other (using a second-order polynomial transformation in x and y, using linear interpolation between pixels to assign flux to the pixels in the new image, while preserving the original total flux and pixel size). Next, the edges were cropped from each frame to avoid any distortions in our PSF that may occur due to being far away from the optical axis. Lastly, we needed the full-width at half-maximum (FWHM) of a star and its PSF fitting radius, as well as the characteristics of the chip, e.g. read-noise and gain, as input in the DAOPHOT parameter files. Using a combined image from all the exposures, we utilized the IRAF command `imexam` to measure the FWHM of

the brightest, unsaturated star in the field and its PSF radius, where nearly all of the star's flux should be included. Making this radius large enough is necessary for fitting fainter stars to account for the wings of a neighboring bright star. The radius should typically be close to 10 times larger than the FWHM value. The chip characteristics should all be found in the FITS file headers.

The function `daofind` produces a list of coordinates for most of the stars (including the star-like quasar images) in the field plus an assigned ID number, while `phot` performs a basic aperture photometry on the same stars. This sets a zero-point for our PSF and determines the sky values. Next, a PSF is constructed using the DAOPHOT `psf` function. It is an interactive routine that steps through the star list assembled by `daofind`, shows a surface plot profile of the star and let us choose whether or not to accept it as a "PSF star". The stars chosen constitute the basis for the PSF and should be relatively bright and isolated, hence the crowded quasar images make unfit candidates. With a satisfying PSF (for more complicated fields, Massey and Davis (1992) provides additional steps), we run the function `allstar`, which will perform a PSF fitting to every identified star in the field. The output is the final DAOPHOT photometry file, giving the measured magnitudes and photometric uncertainties for each star, including our quasar images. This last step is repeated for each individual exposure.

The photometry files need to be calibrated before we can combine them to a single data set. We will use four stars in the field to calibrate the magnitudes, where a calibration star should show very little variability and have a color resembling the quasar images. First, be sure to note the ID numbers, designated by DAOPHOT, of the calibration stars and the quasar images (confirmed by their coordinates). For each exposure, the average magnitude of the calibration stars are subtracted from all magnitudes and a normalization average is added $m_N = 16.694$, which will normalize all the measured magnitudes to one collective average. The time of observation are found in the fits file header of the respective exposure. The calibrated magnitudes and their respective observation time is combined into a complete

data set.

The photometric uncertainties calculated by DAOPHOT may be underestimated, as all the exposures are treated individually, and not compared with their respective epochs. To account for this, we compared the spread of each epoch with the uncertainties measured by DAOPHOT, and found that they were in good agreement below a threshold of $\sigma \geq 0.12$ mag. For a spread larger than this, DAOPHOT would systematically underestimate the uncertainties. To give our data more conservative errors, we replaced the photometric uncertainties σ_{phot} measured by DAOPHOT, with the standard deviation in all cases where $\sigma \geq 0.12$ mag and $\sigma > \sigma_{phot}$. For image A this accounted for $\sim 5\%$ of the uncertainties, while for image D, which is much fainter it accounted for $\sim 40\%$. Finally, to remove outliers from our evaluation, we exclude measurements that have an uncertainty $\sigma_i > 0.04$ mag. The resulting light curves of the four quasar images of PS1 J0147+4630 are shown in figure 3.4.

From the light curves we see that the quasar images are bright but significantly less variable than our other target, SDSS J2222+2745 (see figure 3.3). However, some apparently correlated variation can be seen in the A–C light curves, most noticeably a "dip" around day ~ 8350 (MJD), which correspond to the second half of 2018. Image D might be experiencing the same pattern towards the end of the observing period (~ 8550 days). The time delays of PS1 J0147+4630 have never before been measured, only predicted by mass distribution models for the lens, where images A–C are expected have relatively short time delays, of only a few days, while image D is expected to follow the others by about 200 days (Berghea et al., 2017; Shajib et al., 2019). From studying the figure and visually moving the light curves, they do indeed seem to reflect this estimation. The results for our measurements of the time delays are presented in chapter 5.

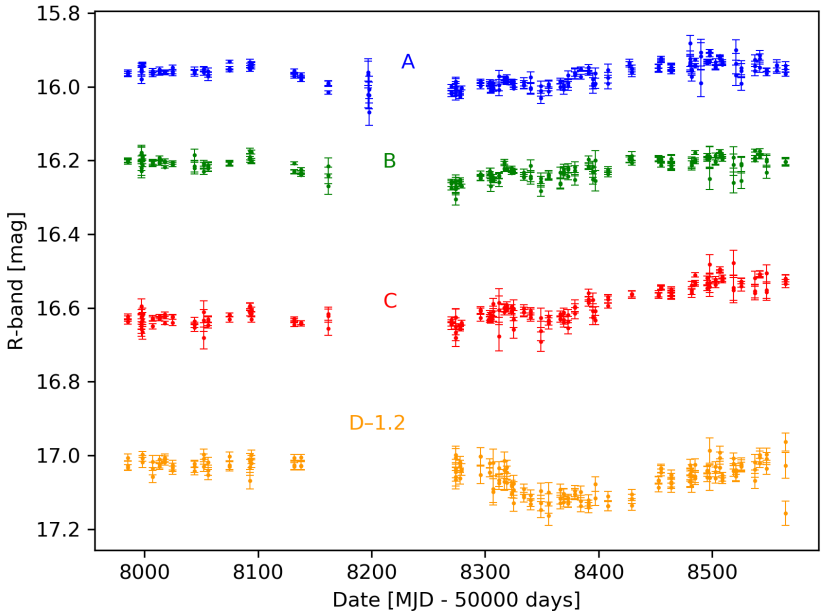

Figure 3.4: Photometric light curves for the four quasar images A–D of the gravitationally lensed quasar PS1 J0147+4630. Image A is seen in blue, image B in green, image C in red and image D in yellow. The errorbars are the uncertainties based on the photometric errors and the standard deviation within each epoch. The measurements are calibrated with the magnitudes of five comparison stars, and normalized to a common average. The image D light curve is moved up on the y-axis by -1.2 mag.

Chapter 4

Methods

The luminosities of quasars are known to be variable in several bands of wavelength and on a wide range of timescales. A quasar will typically vary on the order of 10% on timescales of months to years (Vanden Berk et al., 2004). The physical origin of these fluctuations is still unknown, but some promising sources include accretion disc instabilities (e.g. Kawaguchi et al. (1998); Pereyra et al. (2005)), starburst events (e.g. Aretxaga et al. (1997)) and gravitational microlensing of the quasar (e.g. Zackrisson et al. (2003)).

This section presents the methods used to utilize this property to measure the quasar variability and the time delays of strongly gravitationally lensed quasars that have been split into multiple images.

4.1 Structure function

We want to define the variability of a quasar in terms of a statistical measure of the difference in magnitude at different epochs. One of the primary tools to characterize this phenomenon is the structure function. It is closely related to the autocorrelation function (see Simonetti et al., 1985; Hook et al., 1994) and measures the variability as a function of the time between measurements, i.e. the rest-frame time lag $\tau = t_j - t_i$.

The structure function is given by

$$S(\tau) = \sqrt{\frac{\pi}{2} \sum_{i<j} \mid m_j - m_i \mid^2 - \sigma_j^2 - \sigma_i^2} \tag{4.1}$$

where m_j specifies the magnitude measured at epoch t_j with a measurement uncertainty of σ_j. The scaling factor $\pi/2$ and the absolute value of the magnitude difference is added to make it more robust against outliers in the data (Vanden Berk et al., 2004; Bauer et al., 2009).

There are two common ways to parametrize the structure function and both are fitted to a binned structure function, with bins $\Delta\tau = \tau + d\tau$. The first is an asymptotic function, i.e. a constant minus an exponential (e.g. Hook et al., 1994; Vanden Berk et al., 2004). The second is a power law

$$S(\Delta\tau) = V_0 \left(\frac{\Delta\tau}{\Delta\tau_0} \right)^{\gamma} \tag{4.2}$$

where V_0 is the amplitude at $\Delta\tau_0$ days. Both V_0 and $\Delta\tau$ are constant parameters that will be determined during the fit of the function. γ is the slope of the structure function, and the fit will appear as a straight line in a log-log plot with a steady rise (Vanden Berk et al., 2004; Fohlmeister et al., 2008). The structure function has also been observed to flatten after long time-lags typically larger than 5 years (Cristiani et al., 1996; Hook et al., 1994).

In this project we will be using the power law parametrization of the structure function as it is the most popular in the literature we will be using for comparison, and usually the one that provides the best fit in all wavelength bands based on χ^2 fit statistics (Vanden Berk et al., 2004). The slope of the power law is a measure of the variability of the quasar and will be compared to both theoretical models (e.g. Kawaguchi et al., 1998; Aretxaga et al., 1997) and large observational studies (e.g. Vanden Berk et al., 2004; de Vries et al., 2005; Wilhite et al., 2007).

4.2 Time Delays

The variability of quasars provides us with a powerful tool to measure the time delays between different images of gravitationally lensed quasars. Every quasar will have a unique light curve based on the intrinsic variations of the quasar, and this will be represented in each duplicate image with a shift in time and magnitude, and possibly an image-specific small-amplitude variation due to microlensing caused by stars along the path. There are several methods for predicting the time delays of quasars, where two of the most widely used have been simple χ^2-minimization and the minimal dispersion method (Pelt et al., 1994, 1996). However, these methods do not include corrections for microlensing in the model (except as a static change between seasons), which significantly can affect the time delay measurements (Tie and Kochanek, 2018). This motivates us to apply a newer method that is able to model both intrinsic variation and the uncorrelated microlensing in its estimation of the time delays and its uncertainties for all images, resulting in a model that will fit the data much better.

4.2.1 Polynomial Method

Our main approach of analyzing the quasar light curves and estimating the time delays is based on the method by Kochanek et al. (2006) using Legendre polynomials. Other notable examples of this method being used is by Fohlmeister et al. (2007, 2013), Poindexter et al. (2007), and Vuissoz et al. (2007, 2008). The advantage of this method is that it models the intrinsic variation of the source as well as the microlensing experienced by the individual images separately as two different Legendre series – one higher order for the intrinsic magnitude, and one smoother curve representing the slow photometric microlensing variations in each image.

We first assume that the intrinsic variability of the quasar is well represented by the brightest quasar image. These variations are then approximated by a Legendre series given by

$$s(t) \simeq \sum_{m=0}^{N_{src}} a_m P_m \left[\frac{t - t_c}{\delta t} \right] \tag{4.3}$$

where $s(t)$ represents the magnitude of the source as a function of time t. N_{src} is the polynomial order of the fit, and a_m and P_m are the mth order of coefficients and Legendre polynomials respectively. Legendre polynomials are orthogonal and are only defined within the interval $[-1, 1]$ and the time series is normalized using the midpoint $t_c = (t_N + t_1)/2$ and the half-width $\delta t = (t_N - t_1)/2$ of the time series. The intrinsic variation of the source may be represented by any of the images in the system; it should not affect the time delay measurements. However, dimmer images typically have higher photometric uncertainties and may be more affected by microlensing as the intrinsic flux is weaker (Kochanek et al., 2006).

The microlensing variations are represented by a lower order Legendre series,

$$\Delta\mu(t) = \sum_{m=0}^{N_\mu} c_m P_m \left[\frac{t - t_c}{\delta t} \right] \tag{4.4}$$

where N_μ is the polynomial order of the series, c_m and P_m are the mth order of coefficients and Legendre polynomials, respectively. t_c and δt are defined as above. This lower order polynomial series (usually order 3 or less) models slow and long-term microlensing, as the short-scale effects of microlensing (on timescales of weeks) are not seen as a systematic effect, but rather as an added source of noise (Vuissoz et al., 2007). Assuming the intrinsic variation is well represented by $s(t)$, this term incorporates both a static relative magnification and the differential variations caused by microlensing. However, this does not identify the microlensing specific to each image, as it is measured as the difference relative to the reference image. Any variety found in image i may actually be a combination of the differential effects between the reference image and image i. For our purpose this is not an issue though, as the time delay measurements are affected by the total variation between the image pair (Kochanek et al., 2006; Vuissoz et al., 2007)

The light curve of all the images i is then approximated as a model consisting of the two Legendre series given by

$$m_i(t_j) \simeq s(t_j + \Delta t_i) + \Delta\mu_i(t_j) \tag{4.5}$$

where $s(t_j + \Delta t_i)$ is the intrinsic variability at time t_j shifted by the time delay Δt_i for image i. $\Delta\mu_i$ combines the static shift in magnitude and the differential microlensing variations of image i with respect to the reference image.

The observations m_{ij} of image i at time t_j are then fitted to the model using by the ordinary fitting statistic,

$$\chi^2 = \sum_{i=1}^{N_{im}} \sum_{j=1}^{N_{obs}} \left[\frac{m_{ij} - s\left(t_j + \Delta t_i\right) - \Delta\mu_i\left(t_j\right)}{\sigma_{ij}} \right]^2 \tag{4.6}$$

where N_{im} is the number of images, N_{obs} the number of observations, and σ_{ij} the photometric uncertainties for image i at time t_j. The time delay Δt_i between each image pair $A - i$ (where A is representing the reference image used in equation (4.3)) is one of the parameters of the fit, as well as the variations in flux ratio $\Delta\mu_i$. The best model will be the one where we see no significant positive change in the fit by increasing the number of parameters in the model.

4.2.2 Model selection

The uncertainties in the time delays depend on the characteristics of the interpolation of the light curves and are usually smaller than the true uncertainties (Fohlmeister et al., 2013). We will therefore be comparing our measured time delays to the previous measurements for SDSS J2222+2745 (Dahle et al., 2015), and the predicted values for PS1 J0147+4630 (Shajib et al., 2019). Uncertainties may also be underestimated due to the restriction of the final model, as the number of parameters in the source and microlens-

ing models have a large effect on the time delay estimates (Poindexter et al., 2007). Therefore we will be applying information criteria to our models to better determine the number of parameters in our Legendre series and to let us estimate an average confidence interval that includes several different models.

Information Criteria

We will evaluate our polynomial models using the Akaike information criterion (Akaike, 1974) and the Bayesian information criterion (Schwarz, 1978).

Their general definitions are given by

$$\mathrm{AIC} \equiv -2 \ln \mathcal{L}_{\max} + 2k \tag{4.7}$$

$$\mathrm{BIC} \equiv -2 \ln \mathcal{L}_{\max} + k \ln N_{obs} \tag{4.8}$$

where $k = N_s + N_\mu$ is the number of parameters in the model, N_{obs} is the number of observations and $\ln \mathcal{L}_{\max}$ is the log-likelihood at its maximum point defined as

$$\ln \mathcal{L}_{\max} = \ln(\mathcal{L}(\underline{\hat{\theta}})) = -\frac{1}{2} N_{obs} \ln\left(\hat{\sigma}^2\right) - \frac{N_{obs}}{2} \ln(2\pi) - \frac{N_{obs}}{2} \tag{4.9}$$

where $\sigma^2 = RSS/N_{obs}$ are the maximum likelihood (ML) estimators and $RSS = \sum_{i=1}^{N_{obs}} \hat{\epsilon}_i^2$ is the residual sum of squares with $\hat{\epsilon} = y_i - \hat{y}_i$ as the estimated residuals. For a full statistical explanation, see Burnham and Anderson (2002), and for an explanation tailored to astronomers see Takeuchi (2000).

The best fit is the one that minimizes the information criteria; negative numbers are preferred. The left-hand term - the log-likelihood - rewards a good fit, and will generally improve as more parameters are added. The second term penalizes more parameters in the model, i.e. it grows for an increasing

number of parameters. The AIC/BIC will decrease as the fit improves, but start to increase again when the model adds too many parameters without being able to improve the fit significantly. The BIC treats new parameters more harshly than the more liberal AIC, and will usually choose a model of fewer parameters. The total size of the AIC and BIC values themselves give us little information as they are all strongly dependent on sample size and only comparable to the other AIC/BIC values for models on the same data set. However, they will give us a useful ranking system for the different models fitted to each light curve, i.e. the different set of parameters used in equations (4.3) and (4.4).

A more informative value are the relative AIC- and BIC-differences,

$$\Delta_{i,AIC} = AIC_i - AIC_{min} \tag{4.10}$$

$$\Delta_{i,BIC} = BIC_i - BIC_{min} \tag{4.11}$$

which allows us to compare the quality of models on different sets of data. The model estimated to be best has $\Delta_i \equiv 0$ and models with $\Delta_i > 10$ will generally have little support (Burnham and Anderson, 2002). However, these limits often chooses a model that has too few parameters for our purpose, as we need to capture the intrinsic variations of the quasar light curves through a higher order polynomial (eq.(4.3)). This and the process of choosing an acceptable model will be further discussed in chapters 5 and 6.

Relative Likelihood

When we have an idea of the best models for each light curve, we use that information to evaluate each time delay fit. The *relative likelihood* of a model evaluates each model given the data set and is proportional to the probability that one time delay is a better fit than the previous one,

$$\mathcal{L}(y_i|\Delta t, m) \propto \exp(-\frac{1}{2}\Delta\chi^2) \tag{4.12}$$

The best model has a probability $\mathcal{L} = 1$. A possible issue with choosing just one model is that it may underestimate the uncertainties. The time delay and its uncertainties can be significantly affected by the choice of model parameters, either by the intrinsic model or by the choice of microlensing variation (Tie and Kochanek, 2018). We will evaluate the relative likelihood of different models and discuss confidence intervals on an averaged time delay estimate (e.g. Poindexter et al., 2007; Fohlmeister et al., 2013) in chapter 6.

Chapter 5

Results

5.1 Structure function

To get a measure of the intrinsic variability of the source quasar we used the combined light curve from images A, B and C, where B and C have been shifted according to their time delays and magnitudes with respect to A, to calculate the structure function given by equation (4.1). The time delays used in this calculation are the ones found by Dahle et al. (2015), $\Delta t_B = 43.3$ days and $\Delta t_C = 702.2$ days, and the static magnitude shifts $\Delta m_B = 0.343$ mag and $\Delta m_C = 0.494$ mag. Microlensing is not included as it is not expected to have a significant effect on the structure function; the variation in magnitude caused by microlensing is very small compared to the intrinsic variations of the source (Fohlmeister et al., 2008). We confirm this by measuring the microlensing variations, see section 5.2.3.

The combined data set includes time-lags spanning from $\sim$ 0.01 days to $\sim$ 3200 days between the first and last epochs. The shortest rest-frame time lags τ are cut out ($\tau < 2$ days) because in this range the amplitude of the intrinsic variability is smaller than the noise, resulting in a 'flat' structure function (Bauer et al., 2009). Higher time lags ($\tau > \tau_{max}/2$) were also cut out since our three light curves do not overlap at larger intervals, hence may

not represent the intrinsic variability of the source completely. The final sample of rest-frame time lags and corresponding magnitude difference is 257 961 elements. The data was sorted with respect to increasing rest-frame time lag and binned into intervals with an approximately equal length in logarithmic scale $\Delta\tau = ln(\tau) + d(ln(\tau))$. The number of bins is chosen so we have a relatively large sample of measurements in each bin. The number of measurements in each bin ranges from 293 in the shortest time lag interval to 79 916 in the longest. Multiple bin sizes and interval-lengths were tested, which overall only had a very small effect on the result of the structure function slope.

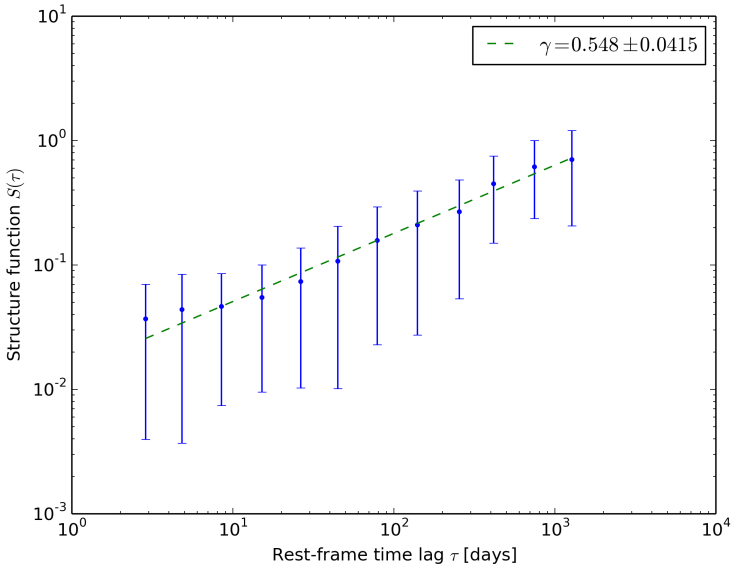

Figure 5.1: The binned structure function of quasar J2222+2745 in the g_{SDSS}-band against rest-frame time lag, plotted on double logaritmic axes. The structure function is calculated from the combined observations of the ABC images, corrected for time lag and static shift in magnitude. The power-law slope is fitted using least squares and have a slope $\gamma = 0.548 \pm 0.0415$. The errorbars represent the standard deviation from the mean in each bin.

The power-law slope is calculated using the parametrization given in equation (4.2) and fitted using least squares optimization. The uncertainty in the slope comes from the standard deviation errors on the parametrization. For SDSS

J2222+2745 I found a slope $\gamma = 0.548 \pm 0.0415$, which can be seen plotted in figure 5.1. In table 5.1 we see the results of this paper compared with the structure function slopes from several other studies, based on large sample observational surveys and theoretical models.

Structure function slope	
γ	Object
0.548 ± 0.0415	SDSS J2222+2745

Comparison with observational results		
γ	Reference	Sample size
0.239 ± 0.030	Vanden Berk et al. (2004)	$\sim 25,000$
0.153 ± 0.004	de Vries et al. (2005)	$\sim 35,000$
0.479 ± 0.010	Wilhite et al. (2007)	$\sim 8,000$
0.432 ± 0.024	Bauer et al. (2009)	$\sim 23,000$

Comparison with theoretical results		
γ	Reference	Model
0.44 ± 0.03	Kawaguchi et al. (1998)	Disk Instability
0.83 ± 0.08	Kawaguchi et al. (1998)	Starburst

Table 5.1: Structure function slopes for the results of this paper and compared with both large observational surveys and theoretical models.

This shows that SDSS J2222+2745 has a higher variability than the average, which ranges from $\gamma = 0.153 \pm 0.04$ (de Vries et al., 2005) to $\gamma = 0.479 \pm 0.01$ (Vanden Berk et al., 2004). However, de Vries et al. (2005) does argue that their quasar sample is heavily affected by measurement noise, which in turn lowers the structure function (de Vries et al., 2003). When they remove the "white noise" they get a slope of $\gamma = 0.30 \pm 0.01$. The theoretical models derived by Kawaguchi et al. (1998) have the slopes: $\gamma = 0.44 \pm 0.03$ for the disc instability model, and $\gamma = 0.83 \pm 0.08$ for the starburst model. The results from SDSS J2222+2745 lie somewhere in between that, and does not seem to suggest that either model would be a better explanation for the variability of the quasar.

5.2 Time Delays and Microlensing

The time delays are calculated using the polynomial methods of Kochanek et al. (2006) discussed in chapter 4.2. The method measures the time delays between lensed quasar images by making a fit to the light curves and

minimizing the distance between them.

The model light curve is created using Legendre polynomial series – one high order that models the intrinsic variations of the source (eq. (4.3)), and one low order that models the differential variations in the curves and with it the microlensing of each image (eq. (4.4)) – which are added together to form a smooth light curve (eq. (4.5)). The high order polynomial will be on the order of $N_{src} = 5 - 30$ and the low order series at $N_{\mu} = 0 - 5$. The implementation of the polynomial method requires four steps.

5.2.1 Light curve model

We start by choosing the image that should act as a reference to the source variability, this is usually the brightest image in the set, but could be any of them. For both our quasars, SDSS J2222+2745 and PS1 J0147+4630, we are using image A (the brightest) as the reference. In figure 5.2 we see the light curves of the A-images for both quasars. They are both fitted with a high order Legendre polynomial series given in equation (4.3). Simultaneously, the variations due to microlensing are modeled as a lower order Legendre series given by equation (4.4), and fitted to the data. The static shift is represented by the 0'th order polynomial. The total model is given by equation (4.5) and is fitted to the data after a time delay has been added. The coefficients of the Legendre series are fitted to the data using the `polynomial.legendre` functions in the python package `numpy`, which uses least-square methods to optimize the parameters (Oliphant, 2015). The modeled light curves are often split up between the multiple seasons of observing (e.g. Vuissoz et al., 2007; Fohlmeister et al., 2013; Tsvetkova et al., 2016). This was tested but produced results of higher uncertainties, especially for PS J0147+4630 as it has very low amplitudes of variability. The seasonal gaps for both our quasars are relatively short (130 and 73 days for SDSS J2222 and PS J0147+4630, respectively) and the rest of the curve has a high sampling rate over a long time span, which manages to produce a good model of the light curve even crossing the seasonal gaps.

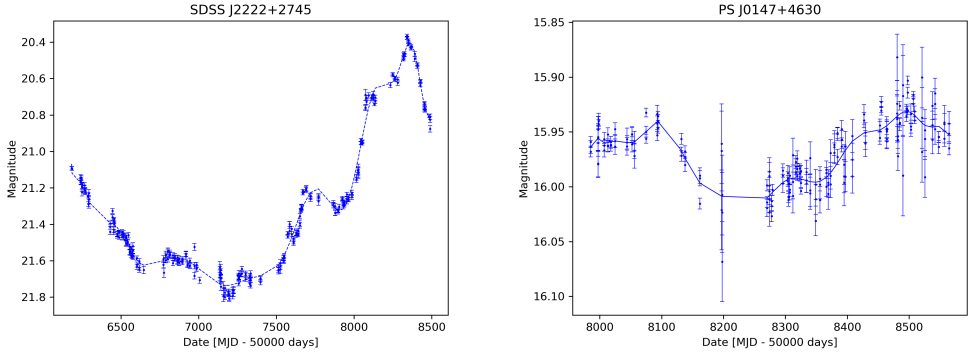

Figure 5.2: The measured magnitudes for the A-images for the quasars SDSS J2222+2745 (left) and PS1 J0147+4630 (right), along with the fitted model representing the intrinsic variations of the source. Th errorbars represent the measurement errors. The polynomial fitted to SDSS J2222+2745 have $N_{src} = 19$ (in eq.(4.3)), representing the polynomial orders used for fitting image B and C. For PS1 J0147+4630 the polynomial is also of the order $N_{src} = 19$, which proved to be a good model for fitting all three images, BCD.

Before fitting the model we need an array of time delays Δt for the code to step through. From the light curves seen in figures 3.3 and 3.4 it is possible to visually estimate approximately what the time delays should be. For SDSS J2222+2745 image B should be about 45 days behind image A, while image C is leading with about 700 days. This is also confirmed by previous estimations by Dahle et al. (2015), see table 5.2. Several were tested but the final series of time-delays spans from -100 to 0 days for image B, and from 650-750 days for image C. PS1 J0147+4630 is much less variable than J2222, and the data is from a much shorter time span, as it was discovered as recently as 2017. The variations are not as obvious as in J2222 but there is still some structure. It seems images ABC are within only a few days of each other, i.e. $\pm$10 days and image D is about 170-180 days behind image A. These rough estimations also coincides with the time delays predicted through lens modeling by Berghea et al. (2017) and Shajib et al. (2019), listed in table 5.2. For images B and C, the time delay array is therefore covering delays of $\pm$10 days, and for image D from -200 to -100 days. Each array covers 1000 steps. Several other step lengths were tested, but this was an overall

good value with respect to accurate predictions as well as computation time. This does result in different step-lengths for time delay series for the different images (ranging from 0.02 to 0.1), but they will all be short enough to get an accurate estimation of the time delay and its uncertainties.

SDSS J2222+2745 measurements			
Δt_{AB} (days)	Δt_{CA} (days)	Data	Reference
$42.0^{+1.1}_{-0.1}$	717.4 ± 0.5	NOT, Gemini	Dahle et al. (2015) (χ^2)
47.7 ± 6	722 ± 24	NOT, Gemini	Dahle et al. (2015) (Dispersion)
PS1 J0147+4630 predictions			
Δt_{AB}	Δt_{AC}	Δt_{AD}	Reference
0.1	1.7	226.2	Berghea et al. (2017)
-2.1 ± 0.3	-7 ± 1	-193 ± 18	Shajib et al. (2019)

Table 5.2: Previously measured time delays for SDSS J2222+2745, and time delays predicted by different lens modeling techniques for PS1 J0147+4630.

5.2.2 Model selection

The best model is the one that minimizes the χ^2 (eq.(4.6)) between the data and the model. However, in our case, models with too few parameters in N_{src} will not be able to capture the details of the intrinsic variation of the light curves, and models with too many parameters in either N_{src} or N_μ will produce oscillations that do not accurately reflect the light curve. We generally see an overly smooth model for orders $N_{src} \lesssim 15$ in the light curves for all our different images for both of our quasars. We also frequently get unacceptable oscillations for models with either $N_{src} \gtrsim 30$ or $N_\mu > 3$. As mentioned in section 4.2, the microlensing variation represented by N_μ is a slow photometric effect and realistically will not be a higher than a 3rd order polynomial as any variations happening on short time scales are considered an additional source of noise. These behaviors help guide us to selecting an acceptable model. In addition, the curves are analyzed using two statistical information criteria; the Akaike Information Criterion (AIC) and the Bayesian Information Criterion (BIC), a description can be found in section 4.2.2. The AIC and BIC are given by equations (4.7) and (4.8), and their differences, ΔAIC and ΔBIC, by equations (4.10) and (4.11). Their advantage compared to standard χ^2 statistics, is that in addition to rewarding

a goodness-of-fit, they both penalize an increasing number of parameters. They are both minimized when adding more parameters fail to significantly improve the fit. We will be using the AIC- and BIC-differences to compare the possible models available for each quasar image light curve. They are calculated for each time delay model in addition to the standard χ^2, and the minimum value for ΔAIC and ΔBIC from every time-delay series Δt_i are plotted against their respective intrinsic model parameters N_{src}, for every order of microlensing N_μ tested. The shapes of the plots are very similar for each of the separate images. However, the Bayesian criterion typically gives a harder penalty for adding new parameters and therefore favors smaller models, while the Akaike criterion is more liberal. The plots can be seen in figures 5.3 and 5.4 for SDSS J2222+2745 and PS1 J0147+4630, respectively.

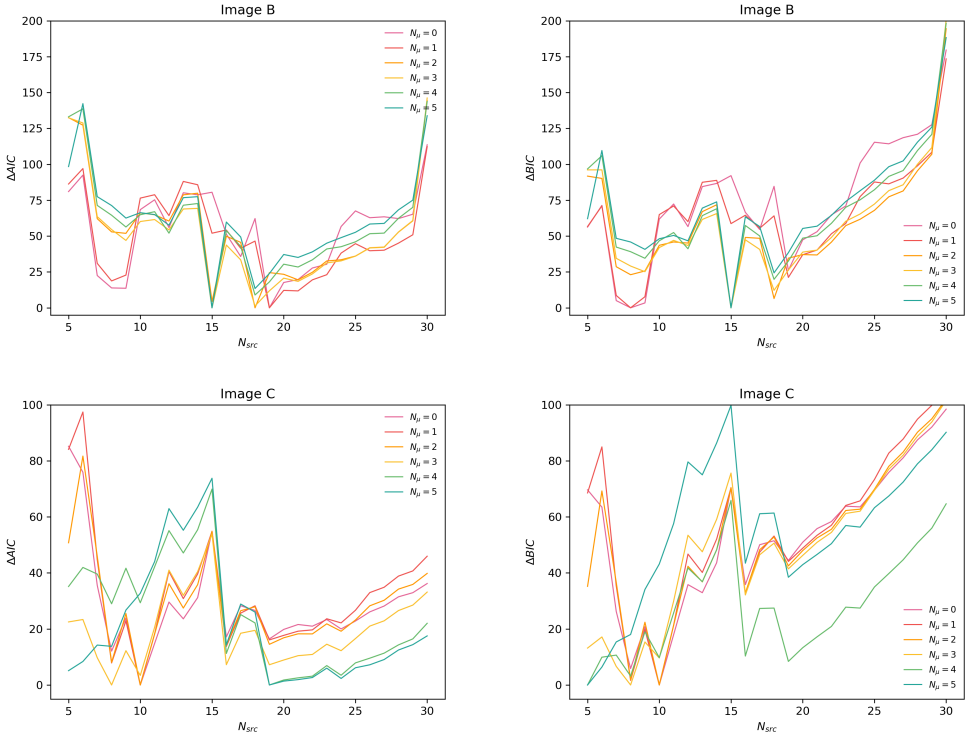

Figure 5.3: Δ AIC and Δ BIC plots for SDSS J2222+2745.

Studying the information criteria plots for SDSS J2222+2745, image B, we see that the best models are probably at $N_{src} = 15, 18, 19$. As mentioned,

the models with $N_{src} < 15$ are too smooth to represent the light curve details accurately, even though they statistically have good fits (compared to number of parameters). It is also apparent that microlensing models of orders $N_\mu \geq 2$ are preferred, and even though the 0th and 1st order compares to the others at $N_{src} = 19$, we can see from the χ^2-statistics that $N_\mu = 2$ still greatly improves the fit (where for $N_{src} = 19$, $\chi^2 = 3338$ for $N_\mu = 1$ and $\chi^2 = 2158$ for $N_\mu = 2$). Models of higher orders does not significantly improve the fit or the criteria. This implies that image B shows high microlensing variation in the 2nd order, hence we will be using $N_\mu = 2$ for our final model. For image C, the same applies to the lower order models for the intrinsic variation as for image B, and the best models seem to be in the range $N_{src} = 19 - 24$. After this the value continues to rise steadily as new parameters are added without improving the goodness-of-fit. We will be using $N_{src} = 19$ for both image B and image C in our final estimations. As for microlensing in image C, the higher order polynomials seem to produce the best models, however, they also produce an unrealistic amount of oscillations in between the data points, as well as shape the curve into a new form. Looking at the χ^2-values from our tests, adding the 2nd order polynomial gives the best fit (where we have $\chi^2 = 1293$ for $N_\mu = 1$ and $\chi^2 = 1196$ for $N_\mu = 2$, given $N_{src} = 19$).

For our second quasar, PS1 J0147+4630, the information criteria plots are seen in figure 5.4. All images have really low values at $N_{src} < 15$, but again, these light curves are all overly smooth and do not capture the observed light curve. The values for PS1 J0147+4630 are especially low as the quasar has very low amplitude variation, and resembles a straight line *more* than the highly variable SDSS J2222+2745 (as seen in section 5.1). Image B and image C both have minima at $N_{src} = 17, 19$ that suggests good models. For both images, $N_{src} = 19$ has the best χ^2-statistic so we will be using that for our final models. Microlensing in image B does not seem to be particularly strong, all models are fairly consistent. However, adding a first order model does improve χ^2 significantly, from $\chi^2 = 423$ for $N_\mu = 0$ to $\chi^2 = 297$ for $N_\mu = 1$, given $N_{src} = 19$, so we will adopt a linear model for image B.

For image C, the $\Delta AIC/\Delta BIC$ plots show a more obvious improvement

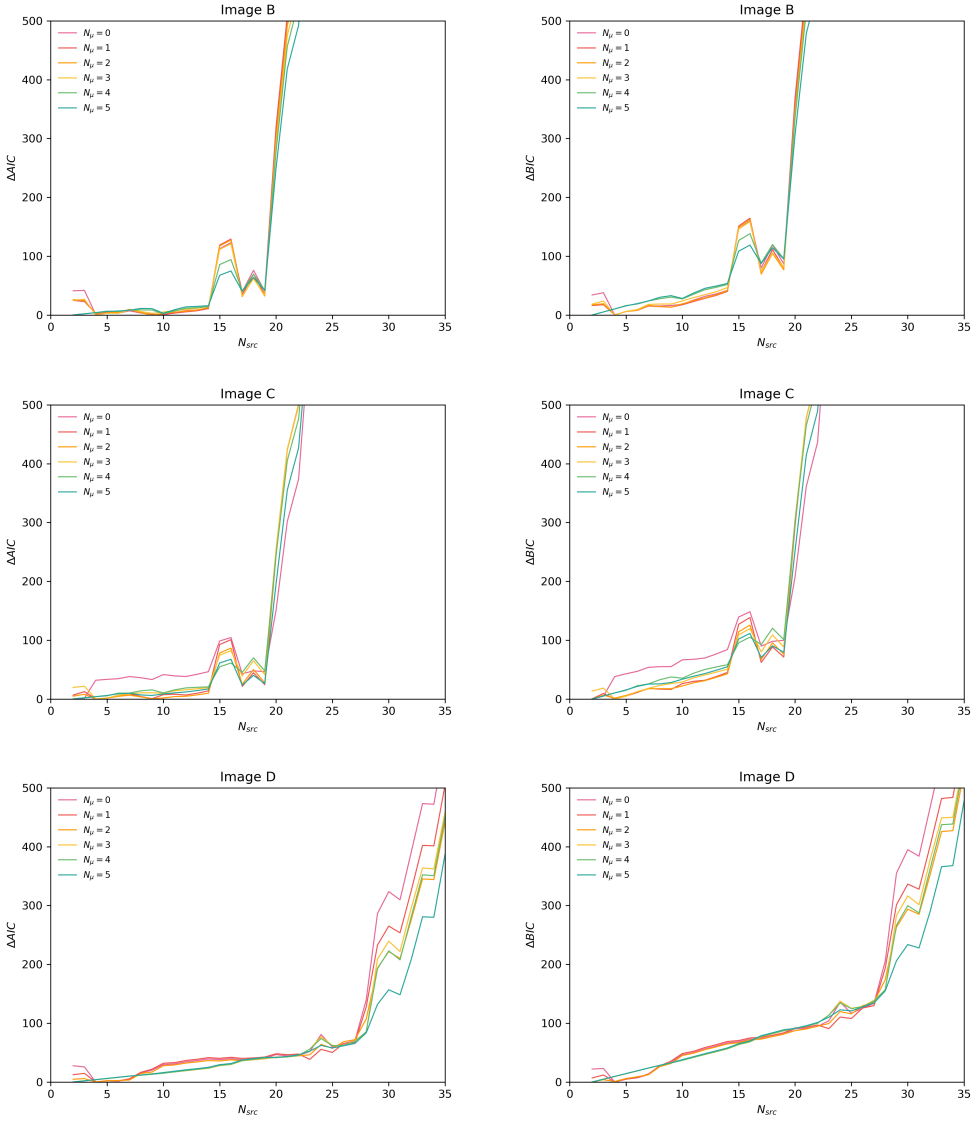

Figure 5.4: Δ AIC and Δ BIC plots for PS1 J0147+4630.

from $N_\mu = 0$ to $N_\mu = 1$. Higher orders of microlensing do not improve the fit, neither for the $\Delta AIC/\Delta BIC$ values nor the χ^2 values, hence we will be using a liner model for image C as well. Image D suggests relatively good models $N_{src} < 27$. However, the higher order models produce large oscillations in the data, meaning it adds amplitude variations that are not real to our intrinsic light curve. By studying both statistics, we conclude that

$N_{src} = 19$ is a good model. This means $N_{src} = 19$ is a good polynomial order for all of our light curves. The microlensing in image D is pretty consistent when looking at the $\Delta AIC/\Delta BIC$ plots, but shows an improvement for both first and second order microlensing in the χ^2 fit. The third order polynomial provide even better values, but when plotting it shows that the curve has been exaggerated to fit the data, and does not represent a realistic change. We will therefore use $N_\mu = 2$ for our last image.

In summary, the best models are chosen using the following guidelines: 1) Find the models with minimized AIC/BIC values. 2) Choose a subset of these models with not too few parameters (smooting does not capture detail) or too many (oscillations create fake amplitudes), this gives us lower and upper limits. 3) If the AIC/BIC between two microlensing models are ∼equal, check the chi-squared value and see whether adding an extra parameter offers a significant improvement in the fit. If not, use the model with fewer parameters.

5.2.3 Final light curve for SDSS J2222+2745

In figure 5.7 we see the superimposed light curve for quasar SDSS J2222+2745, where the best-fitting time delays have been added, and the differential microlensing models have been subtracted from the BC images. The final light curve models have the parameters $N_{src} = 19$ and $N_\mu = 2$ for both images. Our final time delay estimates for SDSS J2222+2745 are

$$\Delta t_{AB} = -42.44^{+1.44}_{-1.36}\ (^{+3.4\%}_{-3.2\%})\ \text{days}$$
$$\Delta t_{AC} = 696.65^{+2.10}_{-2.00}\ (\pm 0.3\%)\ \text{days}$$

which means image C leads A, and image A leads B. The uncertainties correspond to their 95% confidence intervals. The delays are close to their expected values and produces a good fit for the curve.

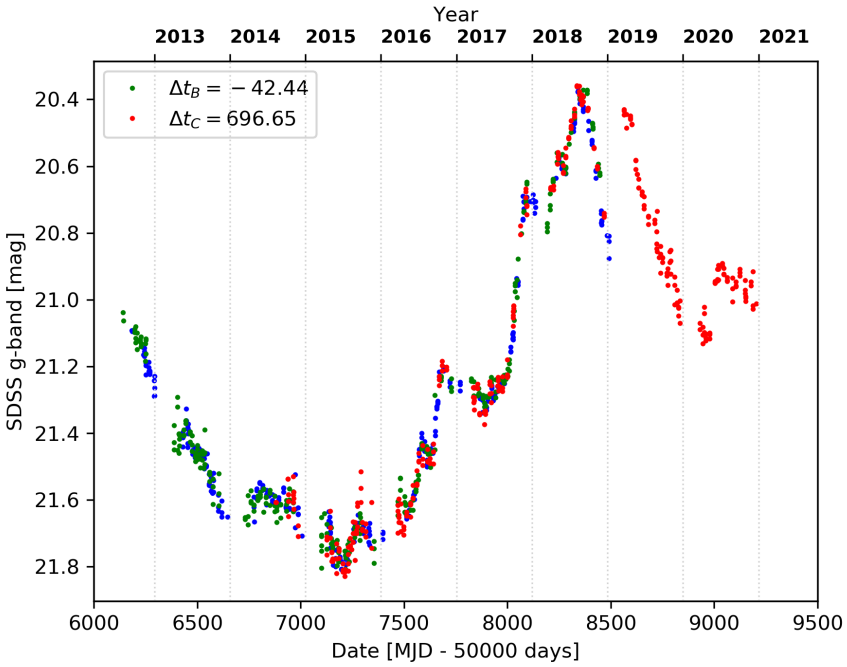

Figure 5.5: The final light curve for the three quasar images of SDSS J2222+2745. Image B and C have been shifted by their respective best-fitting time delays and flux ratios, and the differential microlensing model have been subtracted. The blue dots correspond to image A, the green to image B and the red to image C. The axes are given relative to image A.

The differential microlensing light curves are seen in figure 5.6. Their corresponding microlensing models $\Delta\mu_i$ (eq.(4.4)) are given by

$$\Delta\mu_B(t) = 0.353 \cdot P_0 + 0.032 \cdot P_1 + 0.074 \cdot P_2$$
$$\Delta\mu_C(t) = 0.515 \cdot P_0 - 0.035 \cdot P_1 + 0.095 \cdot P_2$$

which is a Legendre polynomial series where P_m are the Legendre polynomials of order m. The coefficients have all been optimized by least-square methods of the fit. The first term correspond to the 0'th order flux ratio. The uncertainties are given by the root-mean-square error, $RMSE = \sqrt{RSS/N_{obs}}$, where RSS is the residual sum-of-squares from the fit. They represent the

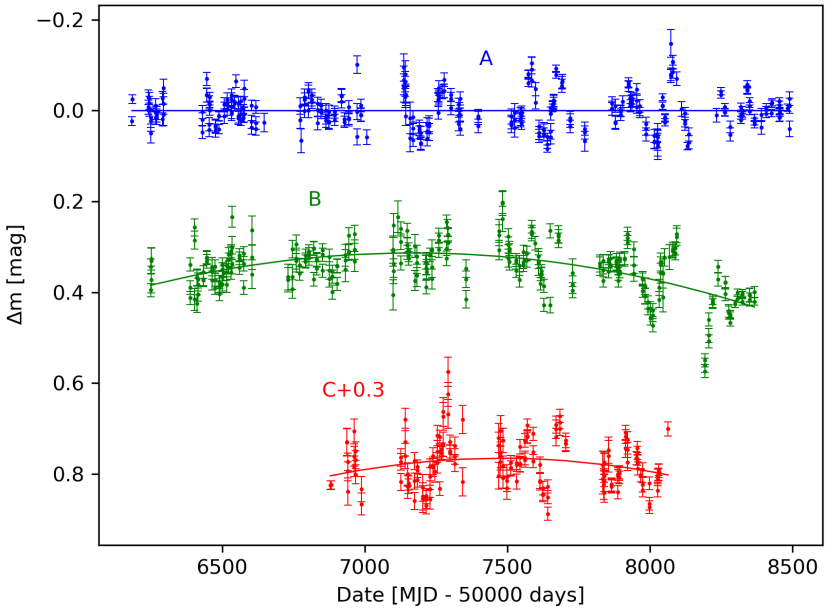

Figure 5.6: Microlensing variability in SDSS J2222+2745. The plot shows the residuals left after subtracting the intrinsic model $s(t)$ from our data and represent the microlensing variability, with respect to image A. The fitted curves are the differential light curve models, $\Delta\mu$. We have only included the parts of images B and C that overlap with image A. The blue dots correspond to image A, the green to image B and the red to image C. Image C has been shifted 0.3 mag down (in positive direction) on the y-axis to avoid clutter.

differences between the model and the data. For SDSS J2222+2745, the uncertainties are $RMSE_B = \pm 0.045$ and $RMSE_C = \pm 0.050$ for the coefficients in $\Delta\mu$. The microlensing curves show some short-term intrinsic patterns that were not included in the source model. If we were to account for this we would need a higher order polynomial for the fit of the light curves, which would also have resulted in "fake" oscillations in amplitude being added. Image A shows a constant trend, as this is the reference image, and image B and C display a clear quadratic variation. This is a typical microlensing pattern where an image have been magnified in the span of a few years as a lensing object has crossed their path. Since we see the same trend in both B and C

images, it could suggest that the microlensing is actually happening to image A as the curves only show the differential patterns with respect to A.

5.2.4 Final light curve for PS1 J0147+4630

The final light curve for quasar PS1 J0147+4630 is shown in figure 5.7. Images B, C and D have been shifted in time by their time delays relative to image A, and the microlensing variations have been subtracted from the curve. We have used the parameters $N_{src} = 19$ and $N_\mu = 1$ for images B and C, and $N_{src} = 19$ and $N_\mu = 2$ for image D. The final time delays are

$$\Delta t_{AB} = -2.21^{+2.08}_{-2.16}\ (^{+94.1\%}_{-97.7\%})\ \text{days}$$
$$\Delta t_{AC} = -5.28^{+2.16}_{-2.22}\ (^{+40.9\%}_{-42.1\%})\ \text{days}$$
$$\Delta t_{AD} = -170.47 \pm 7.61\ (4.5\%)\ \text{days}$$

where image A leads, and the others follow in the order BCD. The uncertainties correspond to their 95% confidence intervals. Images ABC are very close together, while image D experiences a much stronger time delay. This is expected from the geometry as image D appears much closer to the lens galaxy and will be more affected by the gravitational effects. All these delays match well both with our own initial estimates, as well as previous predictions (see table 5.2). In the figure, the left-end tail of the image D light curve trails down because we have subtracted the microlensing effects from the whole curve, even though this part of the curve was not included in the fitting (due to no overlap).

The differential light curve is plotted in figure 5.8, where the best-fit models have been subtracted from the data set without taking microlensing into account. The curves have been shifted with their estimated time delays, and only the observations overlapping with image A are included. The residuals are also fitted with their respective microlensing model curve,

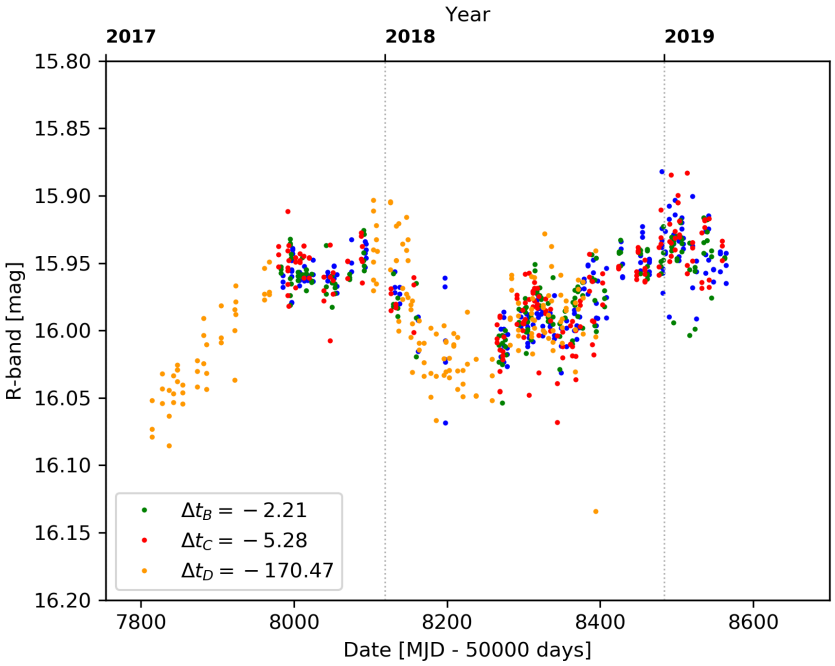

Figure 5.7: The final R-band light curve for the four quasar images of PS1 J0147+4630. Images B, C and D have been shifted in time by their best-fit estimated time delays, and the differential magnitude variation, which includes the effects of microlensing, has been subtracted. Image A is shown in blue, image B in green, image C in red and image D in yellow. The axes are given relative to image A. Observations with measurement errors higher than 0.04 mag have been cut from the evaluation to prevent noisy light curves.

$$\Delta\mu_B(t) = 0.252 \cdot P_0 + 0.005 \cdot P_1$$
$$\Delta\mu_C(t) = 0.635 \cdot P_0 - 0.050 \cdot P_1$$
$$\Delta\mu_D(t) = 2.243 \cdot P_0 - 0.092 \cdot P_1 - 0.072 \cdot P_2$$

where P_m are the Legendre polynomials of order m. The coefficients have the uncertainties $RMSE_B = \pm 0.016$, $RMSE_C = \pm 0.019$ and $RMSE_D = \pm 0.029$, representing the root-mean-square errors. Again, image A is the reference image and therefore has a constant fit. Image B shows a weak linear fading over the observational time-span, while image C experiences a relatively strong linear magnification. This seems to be a clear indication of microlensing effects. Image D is linearly magnified as well, this increases about half way in our measurements resulting in a second order fit. The curves all show some amplitude variations that are intrinsic effects that are happening on time-scales too short to be included in the polynomial fit to the reference light curve.

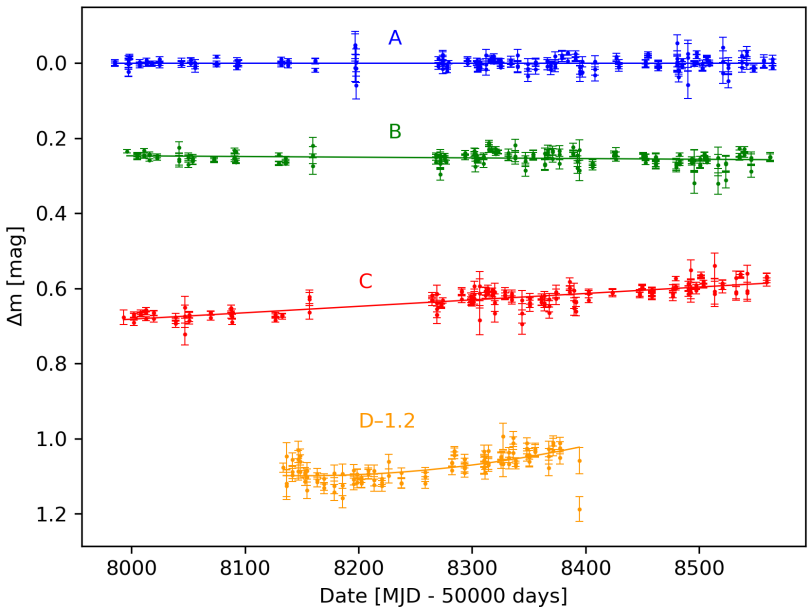

Figure 5.8: Microlensing variability in PS1 J0147+4630. The best-fit intrinsic models have been subtracted from the measurements and the curves have been shifted in time using their respective time delays. Only measurements that overlap with the reference image A are included in the plot. The differential light curves are superimposed as a fit to the residuals. Image A is represented by blue points, image B by green, image C by red and image D by yellow. The much fainter image D was shifted -1.2 mag up on the y-axis.

Chapter 6

Discussion

The respective time delays of the three brightest quasar images of SDSS J2222+2745 were measured to be $\Delta t_{AB} = -42.44^{+1.44}_{-1.36}$ $(^{+3.4\%}_{-3.2\%})$ days, and $\Delta t_{AC} = 696.65^{+2.10}_{-2.00}$ $(\pm 0.3\%)$ days at 95% confidence, using the polynomial method by Kochanek et al. (2006). They have fractionally small uncertainties, especially the AC time delay, which might be the smalles measured uncertainty for a time delay yet. The time delays have also greatly improved the results by Dahle et al. (2015). The small fractional uncertainty is a result of a close to decade-long data set and a particularly variable source. Due to the extended observing time, the A and C light curves now share a large overlapping area, compared to the 2015 results. The structure function was also measured for this quasar, showing it is indeed more variable than the average value of a quasar (see Section 5.1). The AB time delay have a higher fractional uncertainty, mostly due to a shorter time delay, but still offers a great improvement to the previous results. Both the B and C light curve in SDSS J2222+2745 show signs of a second order microlensing event (see figure 5.6). Because the quasar is further from the critical line (meaning it will be less magnified) than what is often seen in quasars lensed by single galaxies, we can also expect a slower microlensing variation Diego et al. (2018). The observed microlensing in the B and C curves show signs of being temporarily magnified on the scale of several years (> 4 years). Note that the microlens-

ing curves seen in figure 5.6 are differential with respect to image A, meaning it may actually be image A that experiences a microlensing event. This might be likely due to B and C following a similar trend. However, it is most likely a combination of all.

The final time delays of PS1 J0147+4630 are $\Delta t_{AB} = -2.21^{+2.08}_{-2.16}$ $(^{+94.1\%}_{-97.7\%})$, $\Delta t_{AC} = -5.28^{+2.16}_{-2.22}$ $(^{+40.9\%}_{-42.1\%})$ and $\Delta t_{AD} = -170.47 \pm 7.61$ (4.5%) days, at 95% confidence. This marks the first time these time delays have been measured, as previously they were only estimated through lens model predictions. The first prediction was done with a simple lens model by Berghea et al. (2017), and the second by a more complicated model by Shajib et al. (2019). We have confirmed that images A, B and C lie very close in time, with a total time delay between them < 10 days. The short A-C time delays produce very large fractional uncertainties. Time delay effects from microlensing is an absolute error, rather than fractional, and can therefore be very significant in small time delays. This effect is especially common in four-image systems, because they have a high degree of symmetry (Tie and Kochanek, 2018). To be able to reduce the fractional uncertainties on the time delays, we will need to monitor the images for a very long time ($\sim$ decades), if not we would need a much more variable quasar (Eigenbrod et al., 2005). The AD time delay, however, is significantly longer. This was expected from the image configurations, as image D lies much closer to the lens galaxy on the optical axis, meaning it will be the most affected by the relativistic time dilation effects. This long delay also produces much smaller fractional uncertainties than the others, which makes it (along with the relatively simple lens model) an excellent candidate for estimating the Hubble constant.

As mentioned in chapter 4, a possible issue with limiting the final estimate to a single model is that the uncertainties may be underestimated (Poindexter et al., 2007). Microlensing variations especially, might have a substantial effect on the time delay measurements (e.g. Tie and Kochanek, 2018). To evaluate this, we study the effects of the time delay model parameters using relative likelihoods (see eq (4.12) and discussion in section 4.2.2).

For SDSS J2222+2745, the relative likelihoods for some of the statistically

best light curve models (following the discussion in section 5.2.2) are plotted in figure 6.2. In the left-hand figure, we see the relative likelihood plots for image B, for models with the polynomial orders $N_{src} = 18, 19$ and for different degrees of microlensing $N_\mu = 0 - 2$ (as discussed, higher orders than this are not useful). We see from studying the plot that image B is a good example on time delays varying with the model parameters. The confidence interval estimated for our results does not cover the gap in model discrepancy. However, the models are not all statistically equal, and this plot reflect our discussion in section 5.2.2 well. The models $(N_{src}, N_\mu) = (18, 0)$, (18,1) and (19,0) give poor fits to the data, ruling our zero orders of microlensing, and possibly a linear model. As we see from the plot, these are the models furthest from our final estimate. (18,2) is a relatively good model, as we have seen that the differential light curve indeed show signs of a second order microlensing term (see figure 5.6). (19,1) seems to provide a relatively good model, but a linear microlensing trend is ruled out in favour of a quadratic by the data.

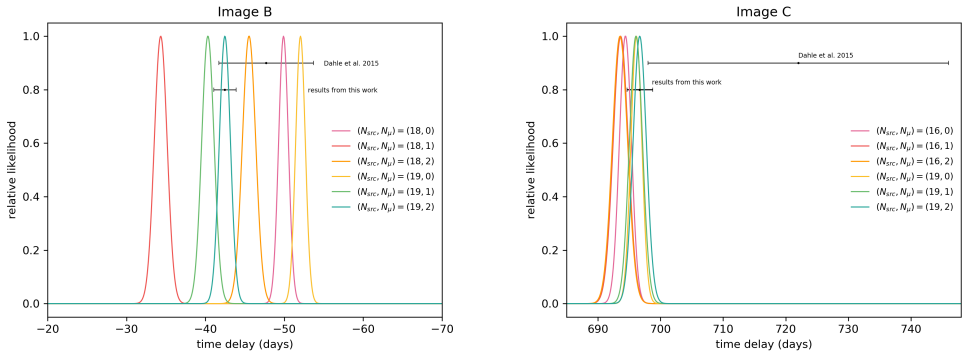

Figure 6.1: Relative likelihood plots for each time delay in SDSS J2222+2745, for different parameter sets in the light curve model. Left-hand side shows the time delays between image A and B, while the right hand side show the AC time delay. The errorbars indicate the uncertainties estimated in this work as well as the one meaured by Dahle et al. (2015).

Image C in SDSS J2222+2745 is a very long time delay, hence it will be much more robust against microlensing effects (Tie and Kochanek, 2018). This becomes apparent from the right-hand plot of figure 6.2, where the relative likelihood in image C is plotted for a few models. The light curve

for image C is relatively stable, and depends more on the choice of intrinsic model N_{src} rather than microlensing. In section 5.2.2, we argued that a model with $N_{src} = 16$ might be overly smooth, meaning it includes less detail of intrinsic variations in the light curve. This can also make it less accurate by smooting over important details needed for precise fitting, which might be an explanation for the small discrepancy seen between the intrinsic models. The quasar is also highly variable, as shown by the structure function, making the intrinsic variations easier to measure between the curves. The long time delay of image C and the high variability of the quasar, combined with a long term monitoring campaign produce relatively consistent results for all models image C.

For PS1 J0147+4630 the relative likelihooda are plotted in figure 6.2. On the left-hand side we have image B, where the short time delays give us a large fractional error. The estimated uncertainty in the predictions by Shajib et al. (2019) are secondary errors from the lens model parameters, where small fractional uncertainties translate to very small errors in the cases of short time delays. The same thing happens with the predicted uncertainty in image C, seen in the right-hand panel. For our measured results, we see that the estimated time delay in image C is mostly affected the choice of microlensing parameter N_{μ}. In figure 5.8 we see that image C experiences a clear linear magnification over time, evidently indicating a microlensing event. Both first and second order polynomials in microlensing provide relatively good fits for the image C time delays, in the intrinsic models seem to match the data well. The least favored models are clearly the ones where no microlensing is present, i.e. $N_{\mu} = 0$, and they are also strongly ruled out by the data.

In the bottom panel, image D shows an opposite effect due to the much longer time delay. The uncertainties in the predicted time delays are much more conservative, due to a similar fractional uncertainty as in images B and C, while having a much larger time delay. For our results, the time delay measurement for image D show a clear relation between microlensing model and time delay. Adding a first or second order term for microlensing is clearly improving the fit (see discussion in section 5.2.2), while a model

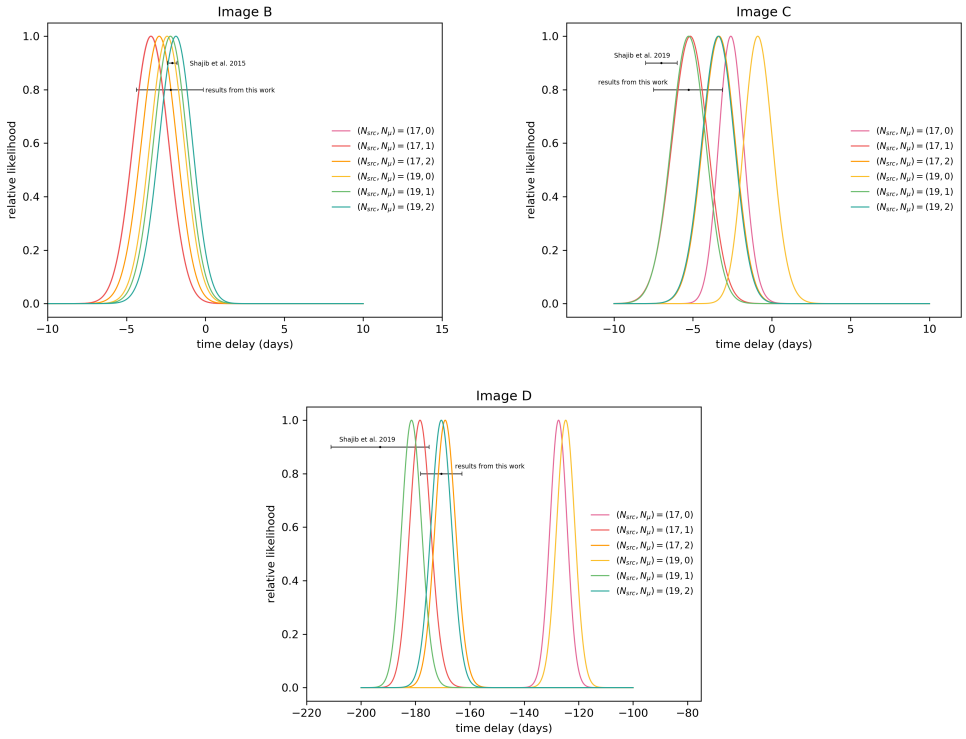

Figure 6.2: Relative likelihood plots for the time delays of PS1 0147+4630.

with no microlensing have no support in the data.

The analysis of the relative likelihood curves show that the measured uncertainties in the time delays should be interpreted conservatively, due to the fact that they are evaluated based only on one final model. However, some models are clearly statistically better than others and we should keep in mind the discussion from Section 5.2.2. To do a more conservative estimation of the uncertainties, one could add the information criteria described in Section 4.2.2 to the time delay likelihoods to be used as weights, and then estimate an average time delay, based on multiple models (e.g. Poindexter et al., 2007). However, the final result may not give the best measurements of the time delay. The statistical criteria tend to penalize a higher number of parameters harshly, and for the purpose of modeling intrinsic light curves and measuring time delays, often provides models too smooth to capture the intricate details in the source variability.

Measuring accurate time delays of gravitationally lensed quasars have been of high interest, as the time delay is directly, inversely proportional to the Hubble constant $\Delta t \propto H_0^{-1}$. They are also useful in determining the mass profiles of the lens, if we already have an accurate Hubble constant measured from other sources. The long image D time delay of PS1 J0147+4630 is a particularly good candidate for estimating the Hubble constant, given a good lens model. For the purpose of comparing our results, we can use the lens model results from Shajib et al. (2019) to find a scale factor we can use to estimate uncertainties. Shajib et al. (2019) are assuming a Hubble constant $H_0 = 70$ km s^{-1} Mpc^{-1}, and have an estimated time delay for image D $\Delta t_{AD} = -193 \pm 18$ days. Transforming the uncertainties of our measured time delay to this scale, we get $\Delta t_{AD} = -170.47 \pm 15.8$ days. Combining this implied lens uncertainty with our observed, $\sigma = \sqrt{\sigma_{lens}^2 + \sigma_{obs}^2}$, we get a time delay with scaled uncertainties $\Delta t_{AD} = -170.47 \pm 17.53$ days. Using this scale, we can find an estimated Hubble constant of $H_0 = 79.5 \pm 7.95$ km s^{-1} Mpc^{-1}. This crude, but interesting, estimation lies within the range of today's best measurements by astrophysical methods (see the discussion in Section 2.2.2).

Chapter 7

Conclusion

The aim of this thesis has been to measure the time delays between multiply imaged gravitationally lensed quasars, while simultaneously determining the degree of microlensing events affecting the individual images, and as a result their time delays. The motivation behind getting accurate time delay estimations, with a small fractional uncertainty, is their usefulness in constraining the mass density profiles of lens galaxies and clusters, and providing a direct measure of the Hubble constant, independent of other techniques.

The time delays of the three brigtest images, ABC, in the sextuply cluster-lensed quasar SDSS J2222+2745 have been measured and significantly improved previous results. The delays between the images, with respect to image A are $\Delta t_{AB} = -42.44^{+1.44}_{-1.36}$ days, and $\Delta t_{AC} = 696.65^{+2.10}_{-2.00}$ days (95% confidence interval). A slow (> 4 years), second order microlensing effect was measured in both image B and image C, as a differential curve with respect to A. The fractional uncertainties in the longest time delay, AC, is at 0.3%, which is one of the most accurately determined time delays yet. This is a combined result of a decade-long data set, and a highly variable quasar. In addition to having taken microlensing into account. We also proved the high variability of the quasar by measuring the structure function (Vanden Berk et al., 2004).

Secondly, the time delays in the quadruply lensed quasar PS1 J0147+4630 were measured for the first time. The time delays between the four images were found to be $\Delta t_{AB} = -2.21^{+2.08}_{-2.16}$, $\Delta t_{AC} = -5.28^{+2.16}_{-2.22}$ and $\Delta t_{AD} = -170.47 \pm 7.61$ days (95% confidence interval). The three brightest images, ABC, are very close together in time (< 10 days), while the fainter image D has a much longer time delay. The long time delay is good for getting a small fractional uncertainty (4.5%) despite the short observation span, which is very desirable for astrophysical applications. By using the lens model from Shajib et al. (2019) and scaled uncertainties, we found a Hubble constant $H_0 = 79.5 \pm 7.95$ km s^{-1} Mpc^{-1}. The effects of microlensing were measured in all all three images B, C and D, with respect to A, in varying degree. Image B had a very weak increase in magnitude over the span of the observation period of two years, while images C and D both experienced a relatively strong brightening. The configuration of the four images have a very small maximum angular separation ($3\farcs8$), but accurate magnitudes were found using crowded field photometry with the DAOPHOT program in IRAF.

Outlook

Looking at the results from SDSS J2222+2745, the highly accurate time delays provide an excellent opportunity for determining the cluster mass profile (Refsdal, 2004). This can be achieved by combining them with mass constraints from the positions and redshift of additional lensed, unrelated objects in the system measured by Sharon et al. (2017). If we got accurate photometry of the much fainter D-F images, which are partially hidden behind the central galaxies in the cluster, their time delays could be measured and provide an additional constraint on the mass density profile of the cluster. Even further constraints on the lens parameters may come from future observations by the European Extremely Large Telescope and the James Webb Space Telescope. With an accurate lens model, the time delays might even be able to provide a measure of the Hubble constant. This would provide a very interesting results as clusters are in a regime of dark matter, which would

provide a different set of systematic uncertainties.

With the long time delay measured in PS1 J0147+4630, the system provides an extraordinary candidate for calculating the Hubble constant independently of other methods, through the technique first described by Refsdal (1964b). An important future task would be to constrain the mass profile of the lensing galaxy, as well as possible line-of-sight perturbations to be able to measure an accurate H_0, with small fractional uncertainties. This would be a valuable contribution to the discrepancy between the measurements of the HUbble constant from the CMB and from local distance scales (e.g. Cepheids), which is a topic of high tension in the community today. Both methods are so precise that they are currently unable to explain the discrepancy, this means there may be some systematic error that have yet to be accounted for, or we need to add some new physics to the standard cosmological model (e.g. dark energy models or decaying dark matter, see e.g. Planck Collaboration et al. (2018); Rusu et al. (2019) and the references therein).

To reduce the uncertainties in the time delays of PS1 J0147+4630, however, a longer time span of data sets are needed. Because, as we have shown, the three brightest images, ABC, are so close together in time, and their flux is dominating the system, a good strategy would be to get the combined light curve from integrated light of public surveys (e.g. Zwicky Transient Facility). They could be monitored with a high cadence ($\sim$ 3 days) and a high S/N, but with poor spatial resolution. Then we could do intensive monitoring of the fainter D image whenever a raid change in magnitude is predicted.

Bibliography

Akaike, H.

1974. A new look at the statistical model identification. *IEEE Transactions on Automatic Control*, 19(6):716–723.

Aretxaga, I., R. C. Fernandes, and R. J. Terlevich

1997. QSO variability: probing the Starburst model. *Monthly Notices of the Royal Astronomical Society*, 286(2):271–283.

Bar-Kana, R.

1996. Effect of Large-Scale Structure on Multiply Imaged Sources. *The Astrophysical Journal*, 468(17).

Bartelmann, M. and P. Schneider

2001. Weak gravitational lensing. *Physics Reports*, 340(4-5):291–472.

Bauer, A., C. Baltay, P. Coppi, N. Ellman, J. Jerke, D. Rabinowitz, and R. Scalzo

2009. Quasar Optical Variability in the Palomar-QUEST Survey. *The Astrophysical Journal*, 696(2):1241–1256.

Berghea, C. T., G. J. Nelson, C. E. Rusu, C. R. Keeton, and R. P. Dudik

2017. Discovery of the First Quadruple Gravitationally Lensed Quasar Candidate with Pan-STARRS. *The Astrophysical Journal*, 844(90):9.

Blanton, M. R., M. A. Bershady, B. Abolfathi, F. D. Albareti, C. A. Prieto, A. Almeida, J. Alonso-García, F. Anders, S. F. Anderson, B. Andrews, E. Aquino-Ortíz, A. Aragón-Salamanca, M. Argudo-Fernández, E. Armengaud, E. Aubourg, V. Avila-Reese, C. Badenes, S. Bailey, K. A.

Barger, J. Barrera-Ballesteros, C. Bartosz, D. Bates, F. Baumgarten, J. Bautista, R. Beaton, T. C. Beers, F. Belfiore, C. F. Bender, A. A. Berlind, M. Bernardi, F. Beutler, J. C. Bird, D. Bizyaev, G. A. Blanc, M. Blomqvist, A. S. Bolton, M. Boquien, J. Borissova, R. van den Bosch, J. Bovy, W. N. Brandt, J. Brinkmann, J. R. Brownstein, K. Bundy, A. J. Burgasser, E. Burtin, N. G. Busca, M. Cappellari, M. L. D. Carigi, J. K. Carlberg, A. C. Rosell, R. Carrera, B. Cherinka, E. Cheung, Y. G. M. Chew, C. Chiappini, P. D. Choi, D. Chojnowski, C.-H. Chuang, H. Chung, R. F. Cirolini, N. Clerc, R. E. Cohen, J. Comparat, L. da Costa, M.-C. Cousinou, K. Covey, J. D. Crane, R. A. C. Croft, I. Cruz-Gonzalez, D. G. Cuadra, K. Cunha, G. J. Damke, J. Darling, R. Davies, K. Dawson, A. de la Macorra, N. De Lee, T. Delubac, F. Di Mille, A. Diamond-Stanic, M. Cano-Díaz, J. Donor, J. J. Downes, N. Drory, H. d. M. des Bourboux, C. J. Duckworth, T. Dwelly, J. Dyer, G. Ebelke, D. J. Eisenstein, E. Emsellem, M. Eracleous, S. Escoffier, M. L. Evans, X. Fan, E. Fernández-Alvar, J. G. Fernandez-Trincado, D. K. Feuillet, A. Finoguenov, S. W. Fleming, A. Font-Ribera, A. Fredrickson, G. Freischlad, P. M. Frinchaboy, L. Galbany, R. Garcia-Dias, D. A. García-Hernández, P. Gaulme, D. Geisler, J. D. Gelfand, H. Gil-Marín, B. A. Gillespie, D. Goddard, V. Gonzalez-Perez, K. Grabowski, P. J. Green, C. J. Grier, J. E. Gunn, H. Guo, J. Guy, A. Hagen, C. Hahn, M. Hall, P. Harding, S. Hasselquist, S. L. Hawley, F. Hearty, J. I. G. Hernández, S. Ho, D. W. Hogg, K. Holley-Bockelmann, J. A. Holtzman, P. H. Holzer, J. Huehnerhoff, T. A. Hutchinson, H. S. Hwang, H. J. Ibarra-Medel, G. d. S. Ilha, I. I. Ivans, K. Ivory, K. Jackson, T. W. Jensen, J. A. Johnson, A. Jones, H. Jönsson, E. Jullo, V. Kamble, K. Kinemuchi, D. Kirkby, F.-S. Kitaura, M. Klaene, G. R. Knapp, J.-P. Kneib, J. A. Kollmeier, I. Lacerna, R. R. Lane, D. Lang, D. R. Law, D. Lazarz, J.-M. L. Goff, F.-H. Liang, C. Li, H. LI, M. Lima, L. Lin, Y.-T. Lin, S. B. de Lis, C. Liu, M. A. C. d. I. Lizaola, D. Long, S. Lucatello, B. Lundgren, N. K. MacDonald, A. D. Machado, C. L. MacLeod, S. Mahadevan, M. A. G. Maia, R. Maiolino, S. R. Majewski, E. Malanushenko, V. Malanushenko, A. Manchado, S. Mao, C. Maraston, R. Marques-Chaves, K. L. Masters, C. K. McBride, R. M. McDer-

mid, B. McGrath, I. D. McGreer, N. M. Peña, M. Melendez, A. Merloni, M. R. Merrifield, S. Meszaros, A. Meza, I. Minchev, D. Minniti, T. Miyaji, S. More, J. Mulchaey, F. Müller-Sánchez, D. Muna, R. R. Munoz, A. D. Myers, P. Nair, K. Nandra, J. C. do Nascimento, A. Negrete, M. Ness, J. A. Newman, R. C. Nichol, D. L. Nidever, C. Nitschelm, P. Ntelis, J. E. O'Connell, R. J. Oelkers, A. Oravetz, D. Oravetz, Z. Pace, N. Padilla, N. Palanque-Delabrouille, P. A. Palicio, K. Pan, T. Parikh, I. Pâris, C. Park, A. Y. Patten, S. Peirani, M. Pellejero-Ibanez, S. Penny, W. J. Percival, I. Perez-Fournon, P. Petitjean, M. M. Pieri, M. Pinsonneault, A. Pisani, R. Poleski, F. Prada, A. Prakash, A. B. d. A. Queiroz, M. J. Raddick, A. Raichoor, S. B. Rembold, H. Richstein, R. A. Riffel, R. Riffel, H.-W. Rix, A. C. Robin, C. M. Rockosi, S. Rodríguez-Torres, A. Roman-Lopes, C. Román-Zúñiga, M. Rosado, A. J. Ross, G. Rossi, J. Ruan, R. Ruggeri, E. S. Rykoff, S. Salazar-Albornoz, M. Salvato, A. G. Sánchez, D. S. Aguado, J. R. Sánchez-Gallego, F. A. Santana, B. X. Santiago, C. Sayres, R. P. Schiavon, J. d. S. Schimoia, E. F. Schlafly, D. J. Schlegel, D. P. Schneider, M. Schultheis, W. J. Schuster, A. Schwope, H.-J. Seo, Z. Shao, S. Shen, M. Shetrone, M. Shull, J. D. Simon, D. Skinner, M. F. Skrutskie, A. Slosar, V. V. Smith, J. S. Sobeck, F. Sobreira, G. Somers, D. Souto, D. V. Stark, K. Stassun, F. Stauffer, M. Steinmetz, T. Storchi-Bergmann, A. Streblyanska, G. S. Stringfellow, G. Suárez, J. Sun, N. Suzuki, L. Szigeti, M. Taghizadeh-Popp, B. Tang, C. Tao, J. Tayar, M. Tembe, J. Teske, A. R. Thakar, D. Thomas, B. A. Thompson, J. L. Tinker, P. Tissera, R. Tojeiro, H. H. Toledo, S. de la Torre, C. Tremonti, N. W. Troup, O. Valenzuela, I. M. Valpuesta, J. Vargas-González, M. Vargas-Magaña, J. A. Vazquez, S. Villanova, M. Vivek, N. Vogt, D. Wake, R. Walterbos, Y. Wang, B. A. Weaver, A.-M. Weijmans, D. H. Weinberg, K. B. Westfall, D. G. Whelan, V. Wild, J. Wilson, W. M. Wood-Vasey, D. Wylezalek, T. Xiao, R. Yan, M. Yang, J. E. Ybarra, C. Yèche, N. Zakamska, O. Zamora, P. Zarrouk, G. Zasowski, K. Zhang, G.-B. Zhao, Z. Zheng, Z.-M. Zhou, G. B. Zhu, M. Zoccali, H. Zou, G. Zasowski, K. Zhang, G.-B. Zhao, Z. Zheng, Z. Zheng, X. Zhou, Z.-M. Zhou,

G. B. Zhu, M. Zoccali, and H. Zou
2017. Sloan Digital Sky Survey IV: Mapping the Milky Way, Nearby Galaxies, and the Distant Universe. *The Astronomical Journal*, 154(1):35.

Burnham, K. P. and D. R. Anderson
2002. *Model Selection and Multimodel Inference: A Practical Information-Theoretic Approach*. Springer.

Cooke, J. H. and R. Kantowski
1975. Time Delay for Multiply Imaged Quasars. *The Astrophysical Journal*, 195:L11.

Courbin, F., P. Saha, P. L. Schechter, and D. Minniti
2002. Quasar Lensing. In *Gravitational Lensing: An Astrophysical Tool*, chapter 1, Pp. 1–54. Springer Berlin Heidelberg.

Cristiani, S., S. Trentini, F. La Franca, and P. Andreani
1996. The optical variability of QSOs. II. The wavelength dependence. *Astronomy and Astrophysics*, 321:123–128.

Dahle, H., M. D. Gladders, K. Sharon, M. B. Bayliss, and J. R. Rigby
2015. Time Delay Measurements for the Cluster-lensed Sextuple Quasar SDSS J2222+2745. *The Astrophysical Journal*, 813(1):9.

Dahle, H., M. D. Gladders, K. Sharon, M. B. Bayliss, E. Wuyts, L. E. Abramson, B. P. Koester, N. Groeneboom, T. E. Brinckmann, M. T. Kristensen, M. O. Lindholmer, A. Nielsen, J.-K. Krogager, and J. P. U. Fynbo
2013. SDSSJ2222+2745: A Gravitationally Lensed Sextuple Quasar with Maximum Image Separation of 15."1; Discovered in the Sloan Giant Arcs Survey. *The Astrophysical Journal*, 773(2):146.

de Vries, W., B. Becker, and R. White
2003. Long-Term Variability of Sloan Digital Sky Survey Quasars. *The Astronomical Journal*, 126(3):1217–1226.

de Vries, W. H., R. H. Becker, R. L. White, and C. Loomis
2005. Structure Function Analysis of Long-Term Quasar Variability. *The Astronomical Journal*, 129(2):615–629.

Diego, J. M., N. Kaiser, T. Broadhurst, P. L. Kelly, S. Rodney, T. Morishita, M. Oguri, T. W. Ross, A. Zitrin, M. Jauzac, J. Richard, L. Williams, J. Vega-Ferrero, B. Frye, and A. V. Filippenko
2018. Dark Matter under the Microscope: Constraining Compact Dark Matter with Caustic Crossing Events. *The Astrophysical Journal*, 857(1):25.

Dyson, F. W., A. S. Eddington, and C. Davidson
1920. IX. A Determination of the Deflection of Light by the Sun's Gravitational Field, from Observations Made at the Total Eclipse of May 29, 1919. *Royal Society of London Philosophical Transactions Series A*, 220(571-581):291–333.

Eddington, A. S.
1920. *Space, Time and Gravitation: An Outline of the General Relativity Theory*. Cambridge University Press.

Eigenbrod, A.
2012. *Gravitational lensing of quasars*, 1st edition. EPFL Press.

Eigenbrod, A., F. Courbin, C. Vuissoz, G. Meylan, P. Saha, and S. Dye
2005. COSMOGRAIL: the COSmological MOnitoring of GRAvItational Lenses I. How to sample the light curves of gravitationally lensed quasars to measure accurate time delays. *Astronomy and Astrophysics, Volume 436, Issue 1, June II 2005, pp.25-35*, 436:25–35.

Einstein, A.
1911. On the Influence of Gravitation on the Propagation of Light. *Annalen der Physik*, 35:898–908.

Einstein, A.
1915. Die Feldgleichungen der Gravitation. *Sitzungsberichte der Königlich Preußischen Akademie der Wissenschaften*, Pp. 844–847.

Einstein, A.
1936. Lens-Like Action of a Star by the Deviation of Light in the Gravitational Field. *Science*, 84(2188):506–507.

Eisenstein, D.
2005. Dark energy and cosmic sound. *New Astronomy Reviews*, 49(7-9):360–365.

Faber, S. M. and R. E. Jackson
1976. Velocity dispersions and mass-to-light ratios for elliptical galaxies. *The Astrophysical Journal*, 204(1):668–683.

Fohlmeister, J., C. S. Kochanek, E. E. Falco, C. W. Morgan, and J. Wambsganss
2008. The Rewards of Patience: An 822 Day Time Delay in the Gravitational Lens SDSS J1004+4112. *The Astrophysical Journal*, 676(2):761–766.

Fohlmeister, J., C. S. Kochanek, E. E. Falco, J. Wambsganss, N. Morgan, C. W. Morgan, E. O. Ofek, D. Maoz, C. R. Keeton, J. C. Barentine, G. Dalton, J. Dembicky, W. Ketzeback, R. McMillan, and C. S. Peters
2007. A Time Delay for the Cluster-lensed Quasar SDSS J1004+4112. *The Astrophysical Journal*, 662(1):62–71.

Fohlmeister, J., C. S. Kochanek, E. E. Falco, J. Wambsganss, M. Oguri, and X. Dai
2013. A Two-Year Time Delay for the Lensed Quasar SDSS J1029+2623. *The Astrophysical Journal*, 764(2):8.

Freedman, W. L., B. F. Madore, B. K. Gibson, L. Ferrarese, D. D. Kelson, S. Sakai, J. R. Mould, R. C. Kennicutt, Jr., H. C. Ford, J. A. Graham, J. P. Huchra, S. M. G. Hughes, G. D. Illingworth, L. M. Macri, and P. B. Stetson
2001. Final Results from the Hubble Space Telescope Key Project to Measure the Hubble Constant. *The Astrophysical Journal*, 553(1):47–72.

Fukugita, M., T. Futamase, M. Kasai, and E. L. Turner
1992. Statistical properties of gravitational lenses with a nonzero cosmological constant. *The Astrophysical Journal*, 393(1):3–21.

Hook, I. M., R. G. McMahon, B. J. Boyle, and M. J. Irwin

1994. The Variability of Optically Selected Quasars. *Monthly Notices of the Royal Astronomical Society*, 268(2):305–320.

Hubble, E.
1929. A relation between distance and radial velocity among extra-galactic nebulae. *Proceedings of the National Academy of Sciences*, 15(3):168–173.

Inada, N., M. Oguri, T. Morokuma, M. Doi, N. Yasuda, R. H. Becker, G. T. Richards, C. S. Kochanek, I. Kayo, K. Konishi, H. Utsunomiya, M.-S. Shin, M. A. Strauss, E. S. Sheldon, D. G. York, J. F. Hennawi, D. P. Schneider, X. Dai, and M. Fukugita
2006. SDSS J1029+2623: A Gravitationally Lensed Quasar with an Image Separation of 22.5 Arcseconds. *The Astrophysical Journal*, 653(2):L97–L100.

Inada, N., M. Oguri, B. Pindor, J. F. Hennawi, K. Chiu, W. Zheng, S. I. Ichikawa, M. D. Gregg, R. H. Becker, Y. Suto, M. A. Strauss, E. L. Turner, C. R. Keeton, J. Annis, F. J. Castander, D. J. Eisenstein, J. A. Frieman, M. Fukugita, J. E. Gunn, D. E. Johnston, S. M. Kent, R. C. Nichol, G. T. Richards, H. W. Rix, E. S. Sheldon, N. A. Bahcall, J. Brinkmann, Z. Ivezic, D. Q. Lamb, T. A. McKay, D. P. Schneider, and D. G. York
2003. A Gravitationally Lensed Quasar with Quadruple Images Separated by 14.62 Arcseconds. *Nature*, 426(6968):810–812.

Irwin, M. J., R. L. Webster, P. C. Hewett, R. T. Corrigan, and R. I. Jedrzejewski
1989. Photometric variations in the Q2237 + 0305 system - First detection of a microlensing event. *The Astronomical Journal*, 98:1989.

Kawaguchi, T., S. Mineshige, M. Umemura, and E. L. Turner
1998. Optical Variability in Active Galactic Nuclei: Starbursts or Disk Instabilities? *The Astrophysical Journal*, 504:671–679.

Kochanek, C. S., N. D. Morgan, E. E. Falco, B. A. Mcleod, J. N. Winn, J. Dembicky, and B. Ketzeback
2006. The Time Delays of Gravitational Lens HE 0435-1223: An Early-

Type Galaxy with a Rising Rotation Curve. *The Astrophysical Journal*, 640(1):47–61.

Lee, C.-H.
2017. Accurate spectroscopic redshift of the multiply lensed quasar PSOJ0147 from the Pan-STARRS survey. *Astronomy & Astrophysics*, 605:4.

Lee, C.-H.
2018. A closer look at the quadruply lensed quasar PSOJ0147: spectroscopic redshifts and microlensing effect. *Monthly Notices of the Royal Astronomical Society, Volume 475, Issue 3, p.3086-3089*, 475(3):3086–3089.

Marinoni, C., A. Saintonge, R. Giovanelli, M. P. Haynes, K. L. Masters, O. L. Fevre, A. Mazure, P. Taxil, and J. M. Virey
2008. Geometrical tests of cosmological models. I. Probing dark energy using the kinematics of high-redshift galaxies. *Astronomy and Astrophysics*, 478(1):43–55.

Massey, P. and L. E. Davis
1992. A User's Guide to Stellar CCD Photometry with IRAF. Technical report.

Narayan, R. and M. Bartelmann
1996. Lectures on Gravitational Lensing. *astro-ph/9606001*.

Oliphant, T. E.
2015. *Guide to NumPy 2nd*, 2nd edition. USA: CreateSpace Independent Publishing Platform.

Paczynski, B.
1986. Gravitational microlensing by the galactic halo. *The Astrophysical Journal*, 304:1–5.

Paczynski, B.
1991. Gravitational microlensing of the Galactic bulge stars. *The Astrophysical Journal*, 371:L63–L67.

Pelt, J., W. Hoff, R. Kayser, S. Refsdal, and T. Schramm
1994. Time delay controversy on QSO 0957+561 not yet decided. *Astronomy and Astrophysics*, 286:775–785.

Pelt, J., R. Kayser, S. Refsdal, and T. Schramm
1996. The light curve and the time delay of QSO 0957+561. *Astronomy and Astrophysics*, 305:97.

Pereyra, N. A., D. E. V. Berk, D. A. Turnshek, D. J. Hillier, B. C. Wilhite, R. G. Kron, D. P. Schneider, and J. Brinkmann
2005. Characteristic QSO Accretion Disk Temperatures from Spectroscopic Continuum Variability. *The Astrophysical Journal*, 642(1):87–95.

Planck Collaboration, N. Aghanim, Y. Akrami, M. Ashdown, J. Aumont, C. Baccigalupi, M. Ballardini, A. J. Banday, R. B. Barreiro, N. Bartolo, S. Basak, R. Battye, K. Benabed, J. P. Bernard, M. Bersanelli, P. Bielewicz, J. J. Bock, J. R. Bond, J. Borrill, F. R. Bouchet, F. Boulanger, M. Bucher, C. Burigana, R. C. Butler, E. Calabrese, J. F. Cardoso, J. Carron, A. Challinor, H. C. Chiang, J. Chluba, L. P. L. Colombo, C. Combet, D. Contreras, B. P. Crill, F. Cuttaia, P. de Bernardis, G. de Zotti, J. Delabrouille, J. M. Delouis, E. Di Valentino, J. M. Diego, O. Doré, M. Douspis, A. Ducout, X. Dupac, S. Dusini, G. Efstathiou, F. Elsner, T. A. Enßlin, H. K. Eriksen, Y. Fantaye, M. Farhang, J. Fergusson, R. Fernandez-Cobos, F. Finelli, F. Forastieri, M. Frailis, E. Franceschi, A. Frolov, S. Galeotta, S. Galli, K. Ganga, R. T. Génova-Santos, M. Gerbino, T. Ghosh, J. González-Nuevo, K. M. Górski, S. Gratton, A. Gruppuso, J. E. Gudmundsson, J. Hamann, W. Handley, D. Herranz, E. Hivon, Z. Huang, A. H. Jaffe, W. C. Jones, A. Karakci, E. Keihänen, R. Keskitalo, K. Kiiveri, J. Kim, T. S. Kisner, L. Knox, N. Krachmalnicoff, M. Kunz, H. Kurki-Suonio, G. Lagache, J. M. Lamarre, A. Lasenby, M. Lattanzi, C. R. Lawrence, M. L. Jeune, P. Lemos, J. Lesgourgues, F. Levrier, A. Lewis, M. Liguori, P. B. Lilje, M. Lilley, V. Lindholm, M. López-Caniego, P. M. Lubin, Y. Z. Ma, J. F. Macías-Pérez, G. Maggio, D. Maino, N. Mandolesi, A. Mangilli, A. Marcos-Caballero, M. Maris, P. G. Martin, M. Martinelli, E. Martínez-González, S. Matarrese, N. Mauri, J. D. McEwen, P. R.

Meinhold, A. Melchiorri, A. Mennella, M. Migliaccio, M. Millea, S. Mitra, M. A. Miville-Deschênes, D. Molinari, L. Montier, G. Morgante, A. Moss, P. Natoli, H. U. Nørgaard-Nielsen, L. Pagano, D. Paoletti, B. Partridge, G. Patanchon, H. V. Peiris, F. Perrotta, V. Pettorino, F. Piacentini, L. Polastri, G. Polenta, J. L. Puget, J. P. Rachen, M. Reinecke, M. Remazeilles, A. Renzi, G. Rocha, C. Rosset, G. Roudier, J. A. Rubiño-Martín, B. Ruiz-Granados, L. Salvati, M. Sandri, M. Savelainen, D. Scott, E. P. S. Shellard, C. Sirignano, G. Sirri, L. D. Spencer, R. Sunyaev, A. S. Suur-Uski, J. A. Tauber, D. Tavagnacco, M. Tenti, L. Toffolatti, M. Tomasi, T. Trombetti, L. Valenziano, J. Valiviita, B. Van Tent, L. Vibert, P. Vielva, F. Villa, N. Vittorio, B. D. Wandelt, I. K. Wehus, M. White, S. D. M. White, A. Zacchei, and A. Zonca
2018. Planck 2018 results. VI. Cosmological parameters. *arXiv:1807.06209*.

Poindexter, S., N. Morgan, C. S. Kochanek, and E. E. Falco
2007. Mid-IR Observations and a Revised Time Delay for the Gravitational Lens System Quasar HE 1104-1805. *The Astrophysical Journal*, 660(1):146–151.

Press, W. H. and J. E. Gunn
1973. Method for Detecting a Cosmological Density of Condensed Objects. *The Astrophysical Journal*, 185:397.

Refsdal, S.
1964a. On the Possibility of Determining Hubble's Parameter and the Masses of Galaxies from the Gravitational Lens Effect. *Monthly Notices of the Royal Astronomical Society*, 128(4):307–310.

Refsdal, S.
1964b. The Gravitational Lens Effect. *Monthly Notices of the Royal Astronomical Society*, 128(4):295–306.

Refsdal, S.
2004. Determination of H0 and the Mass Distribution in the Lensing Galaxy from the Time Delay Effect. In *Thinking, Observing and Mining the Universe*, Pp. 231–235. World Scientific Publishing Co.

Refsdal, S. and J. Surdej
1994. Gravitational lenses. *Reports on Progress in Physics*, 57(2):117–185.

Riess, A. G., S. Casertano, W. Yuan, L. M. Macri, and D. Scolnic
2019. Large Magellanic Cloud Cepheid Standards Provide a 1% Foundation for the Determination of the Hubble Constant and Stronger Evidence for Physics beyond ΛCDM. *The Astrophysical Journal*, 876(1):85.

Rusu, C. E., K. C. Wong, V. Bonvin, D. Sluse, S. H. Suyu, C. D. Fassnacht, J. H. H. Chan, S. Hilbert, M. W. Auger, A. Sonnenfeld, S. Birrer, F. Courbin, T. Treu, G. C. F. Chen, A. Halkola, L. V. E. Koopmans, P. J. Marshall, and A. J. Shajib
2019. H0LiCOW XII. Lens mass model of WFI2033-4723 and blind measurement of its time-delay distance and H0. *arXiv:1905.09338 (submitted to MNRAS)*.

Schmidt, M.
1963. 3C 273 : A Star-Like Object with Large Red-Shift. *Nature*, 197:1040.

Schneider, P., J. Ehlers, and E. E. Falco
1992. *Gravitational Lenses*, Astronomy and Astrophysics Library. Berlin, Heidelberg: Springer Berlin Heidelberg.

Schwarz, G.
1978. Estimating the Dimension of a Model. *The Annals of Statistics*, 6(2):461–464.

Shajib, A. J., S. Birrer, T. Treu, M. W. Auger, A. Agnello, T. Anguita, E. J. Buckley-Geer, J. H. H. Chan, T. E. Collett, F. Courbin, C. D. Fassnacht, J. Frieman, I. Kayo, C. Lemon, H. Lin, P. J. Marshall, R. McMahon, A. More, N. D. Morgan, V. Motta, M. Oguri, F. Ostrovski, C. E. Rusu, P. L. Schechter, T. Shanks, S. H. Suyu, G. Meylan, T. M. C. Abbott, S. Allam, J. Annis, S. Avila, E. Bertin, D. Brooks, A. Carnero Rosell, M. Carrasco Kind, J. Carretero, C. E. Cunha, L. N. da Costa, J. De Vicente, S. Desai, P. Doel, B. Flaugher, P. Fosalba, J. García-Bellido, D. W. Gerdes, D. Gruen, R. A. Gruendl, G. Gutierrez, W. G. Hartley, D. L.

Hollowood, B. Hoyle, D. J. James, K. Kuehn, N. Kuropatkin, O. Lahav, M. Lima, M. A. G. Maia, M. March, J. L. Marshall, P. Melchior, F. Menanteau, R. Miquel, A. A. Plazas, E. Sanchez, V. Scarpine, I. Sevilla-Noarbe, M. Smith, M. Soares-Santos, F. Sobreira, E. Suchyta, M. E. C. Swanson, G. Tarle, and A. R. Walker
2019. Is every strong lens model unhappy in its own way? Uniform modelling of a sample of 13 quadruply+ imaged quasars. *Monthly Notices of the Royal Astronomical Society*, 483(4):5649–5671.

Shapiro, I. I.
1964. Fourth Test of General Relativity. *Physical Review Letters*, 13(26):789–791.

Sharon, K., M. B. Bayliss, H. Dahle, S. J. Dunham, M. K. Florian, M. D. Gladders, T. L. Johnson, G. Mahler, R. Paterno-Mahler, J. R. Rigby, K. E. Whitaker, M. Akhshik, B. P. Koester, K. Murray, and E. Wuyts
2019. Strong Lens Models for 37 Clusters of Galaxies from the SDSS Giant Arcs Survey. *arXiv:1904.05940*.

Sharon, K., M. B. Bayliss, H. Dahle, M. K. Florian, M. D. Gladders, T. L. Johnson, R. Paterno-Mahler, J. R. Rigby, K. E. Whitaker, and E. Wuyts
2017. Lens Model and Time Delay Predictions for the Sextuply Lensed Quasar SDSS J2222+2745. *The Astrophysical Journal*, 835(1):15.

Shu, Y., R. Marques-Chaves, N. W. Evans, and I. Pérez-Fournon
2018. SDSS J0909+4449: A Large-Separation Strongly Lensed Quasar at z˜2.8 with Three Images. *Monthly Notices of the Royal Astronomical Society*, 481(1):L136–L140.

Simonetti, J. H., J. M. Cordes, and D. S. Heeschen
1985. Flicker of extragalactic radio sources at two frequencies. *The Astrophysical Journal*, 296:46.

Stetson, P. B.
1987. DAOPHOT - A computer program for crowded-field stellar photometry. *Publications of the Astronomical Society of the Pacific*, 99(613):191.

Takeuchi, T. T.
2000. Application of the Information Criterion to the Estimation of Galaxy Luminosity Function. *Astrophysics and Space Science*, 271(3):213–226.

The LIGO Scientific Collaboration, The Virgo Collaboration, The 1M2H Collaboration, The Dark Energy Camera GW-EM Collaboration, The DES Collaboration, The DLT40 Collaboration, The Las Cumbres Observatory Collaboration, The VINROUGE Collaboration, and T. MASTER Collaboration
2017. A gravitational-wave standard siren measurement of the Hubble constant. *Nature*, 551(7678):85–88.

Tie, S. S. and C. S. Kochanek
2018. Microlensing makes lensed quasar time delays significantly time variable. *Monthly Notices of the Royal Astronomical Society*, 473:80–90.

Tonry, J. and D. P. Schneider
1988. A new technique for measuring extragalactic distances. *The Astronomical Journal*, 96:807.

Tsvetkova, V. S., V. M. Shulga, and L. A. Berdina
2016. A simple method to determine the time delays in presence of microlensing: application to HE 0435-1223 and PG1115+080. *Monthly Notices of the Royal Astronomical Society*, 461(4):3714–3723.

Tully, R. B. and J. R. Fisher
1977. A new method of determining distances to galaxies. *Astronomy and Astrophysics*, 54(3):661–673.

Vanden Berk, D. E., B. C. Wilhite, R. G. Kron, S. F. Anderson, R. J. Brunner, P. B. Hall, Ž. Ivezić, G. T. Richards, D. P. Schneider, D. G. York, J. V. Brinkmann, D. Q. Lamb, R. C. Nichol, and D. J. Schlegel
2004. The Ensemble Photometric Variability of ˜25,000 Quasars in the Sloan Digital Sky Survey. *The Astrophysical Journal*, 601(2):692–714.

von Soldner, J. G.

1804. On the Deflection of a Light Ray from its Rectilinear Motion. *Berliner Astronomisches Jahrbuch*, Pp. 161–172.

Vuissoz, C., F. Courbin, D. Sluse, G. Meylan, V. Chantry, E. Eulaers, C. Morgan, M. E. Eyler, C. S. Kochanek, J. Coles, P. Saha, P. Magain, and E. E. Falco

2008. COSMOGRAIL: the COSmological MOnitoring of GRAvItational Lenses VII. Time delays and the Hubble constant from WFI J2033-4723. *Astronomy and Astrophysics*, 488:481–490.

Vuissoz, C., F. Courbin, D. Sluse, G. Meylan, M. Ibrahimov, I. Asfandiyarov, E. Stoops, A. Eigenbrod, L. Le Guillou, H. Van Winckel, and P. Magain

2007. COSMOGRAIL: the COSmological MOnitoring of GRAvItational Lenses V. The time delay in SDSS J1650+4251. *Astronomy and Astrophysics*, 464:845–851.

Walsh, D., R. F. Carswell, and R. J. Weymann

1979. 0957 + 561 A, B: twin quasistellar objects or gravitational lens? *Nature*, 279(5712):381–384.

Wilhite, B. C., R. J. Brunner, C. J. Grier, D. P. Schneider, and D. E. V. Berk

2007. On the variability of quasars: a link between Eddington ratio and optical variability? *Monthly Notices of the Royal Astronomical Society*, 383:1232–1240.

Zackrisson, E., N. Bergvall, T. Marquart, and P. Helbig

2003. Can Microlensing Explain the Long-Term Optical Variability of Quasars? *Astronomy and Astrophysics*, 408:17–25.

Zwicky, F.

1937a. Nebulae as Gravitational Lenses. *Physical Review*, 51:290.

Zwicky, F.

1937b. On the Probability of Detecting Nebulae Which Act as Gravitational Lenses. *Physical Review*, 51:679.

Appendix A

Photometry

Table A.1

g-band Photometry of the Three Brightest Images in SDSS J2222+2745

MJD	Image A	Image B	Image C
6182.963	21.092 ± 0.009	21.441 ± 0.009	22.111 ± 0.009
6185.985	21.094 ± 0.009	21.465 ± 0.009	22.111 ± 0.009
6240.930	21.144 ± 0.016	21.490 ± 0.023	22.034 ± 0.031
6240.934	21.166 ± 0.015	21.481 ± 0.020	22.034 ± 0.030
6244.907	21.170 ± 0.014	21.473 ± 0.017	22.145 ± 0.030
6244.911	21.145 ± 0.014	21.520 ± 0.014	22.080 ± 0.019
6244.915	21.155 ± 0.014	21.507 ± 0.014	22.100 ± 0.021
6250.908	21.190 ± 0.021	21.540 ± 0.029	22.101 ± 0.023
6250.912	21.224 ± 0.021	21.490 ± 0.027	22.080 ± 0.022
6250.916	21.197 ± 0.022	21.515 ± 0.030	22.025 ± 0.027
6266.907	21.187 ± 0.014	21.509 ± 0.015	22.122 ± 0.021
6266.911	21.214 ± 0.014	21.513 ± 0.015	22.089 ± 0.020
6266.914	21.203 ± 0.015	21.508 ± 0.019	22.070 ± 0.020
6270.830	21.218 ± 0.015	21.529 ± 0.014	22.168 ± 0.028
6270.834	21.213 ± 0.015	21.518 ± 0.014	22.201 ± 0.024
6270.838	21.224 ± 0.015	21.499 ± 0.014	22.189 ± 0.019
6291.815	21.242 ± 0.015	21.516 ± 0.017	22.243 ± 0.019
6291.819	21.288 ± 0.014	21.568 ± 0.015	22.198 ± 0.019
6294.893	21.229 ± 0.019	21.501 ± 0.025	22.191 ± 0.028
6294.897	21.264 ± 0.023	21.547 ± 0.029	22.160 ± 0.031
6294.901	21.288 ± 0.024	21.506 ± 0.028	22.111 ± 0.025
6430.182	21.396 ± 0.015	21.792 ± 0.015	22.234 ± 0.026
6430.189	21.441 ± 0.015	21.815 ± 0.015	22.261 ± 0.026
6430.197	21.413 ± 0.015	21.741 ± 0.014	22.233 ± 0.025
6446.168	21.363 ± 0.015	21.683 ± 0.020	22.254 ± 0.015
6446.175	21.362 ± 0.016	21.814 ± 0.024	22.260 ± 0.016

Continued on next page

Table A.1 – *Continued from previous page*

MJD	Image A	Image B	Image C
6446.182	21.327 ± 0.014	21.655 ± 0.018	22.260 ± 0.016
6454.178	21.430 ± 0.014	21.821 ± 0.019	22.207 ± 0.019
6454.182	21.443 ± 0.015	21.763 ± 0.018	22.251 ± 0.018
6454.186	21.382 ± 0.014	21.764 ± 0.018	22.295 ± 0.018
6457.183	21.388 ± 0.007	21.767 ± 0.014	22.220 ± 0.016
6457.190	21.401 ± 0.011	21.800 ± 0.014	22.249 ± 0.016
6457.198	21.373 ± 0.011	21.778 ± 0.014	22.227 ± 0.016
6477.090	21.452 ± 0.015	21.765 ± 0.014	22.289 ± 0.030
6477.097	21.455 ± 0.014	21.749 ± 0.014	22.265 ± 0.030
6477.105	21.463 ± 0.014	21.767 ± 0.014	22.283 ± 0.030
6488.130	21.444 ± 0.010	21.721 ± 0.015	22.288 ± 0.020
6488.137	21.472 ± 0.010	21.728 ± 0.015	22.302 ± 0.018
6488.145	21.443 ± 0.010	21.719 ± 0.015	22.281 ± 0.017
6507.150	21.470 ± 0.016	21.781 ± 0.021	22.213 ± 0.017
6507.158	21.455 ± 0.016	21.757 ± 0.021	22.262 ± 0.018
6507.165	21.445 ± 0.015	21.751 ± 0.020	22.235 ± 0.019
6518.141	21.451 ± 0.015	21.761 ± 0.015	22.285 ± 0.021
6518.148	21.471 ± 0.014	21.808 ± 0.014	22.212 ± 0.020
6518.156	21.459 ± 0.013	21.789 ± 0.014	22.208 ± 0.019
6533.039	21.475 ± 0.014	21.812 ± 0.014	22.187 ± 0.019
6533.050	21.502 ± 0.015	21.824 ± 0.015	22.220 ± 0.023
6533.058	21.507 ± 0.015	21.820 ± 0.015	22.197 ± 0.023
6533.065	21.466 ± 0.014	21.837 ± 0.015	22.137 ± 0.022
6543.103	21.497 ± 0.014	21.799 ± 0.015	22.172 ± 0.024
6543.110	21.496 ± 0.014	21.830 ± 0.015	22.169 ± 0.014
6543.118	21.501 ± 0.014	21.788 ± 0.015	22.251 ± 0.015
6549.054	21.461 ± 0.014	21.815 ± 0.017	22.137 ± 0.014
6557.850	21.555 ± 0.014	21.811 ± 0.017	22.162 ± 0.014
6557.854	21.552 ± 0.014	21.853 ± 0.017	22.170 ± 0.014
6557.858	21.523 ± 0.015	21.826 ± 0.018	22.088 ± 0.031
6565.970	21.573 ± 0.012	21.800 ± 0.015	22.078 ± 0.031
6565.977	21.559 ± 0.013	21.829 ± 0.014	22.149 ± 0.027
6565.985	21.531 ± 0.011	21.811 ± 0.015	21.984 ± 0.032
6573.944	21.579 ± 0.010	21.810 ± 0.015	22.077 ± 0.032
6573.951	21.560 ± 0.010	21.806 ± 0.015	22.034 ± 0.027
6573.958	21.579 ± 0.009	21.853 ± 0.015	22.135 ± 0.015
6578.051	21.520 ± 0.018	21.737 ± 0.023	22.160 ± 0.018
6578.055	21.542 ± 0.020	21.806 ± 0.025	22.156 ± 0.014
6578.059	21.577 ± 0.017	21.841 ± 0.022	22.179 ± 0.018
6602.891	21.634 ± 0.015	21.868 ± 0.014	22.163 ± 0.017
6602.899	21.621 ± 0.014	21.889 ± 0.015	22.139 ± 0.020
6602.906	21.585 ± 0.011	21.862 ± 0.015	22.074 ± 0.031
6618.884	21.650 ± 0.014	21.956 ± 0.015	22.211 ± 0.031
6618.888	21.638 ± 0.014	21.880 ± 0.015	22.082 ± 0.032
6618.891	21.602 ± 0.014	21.903 ± 0.016	22.165 ± 0.029
6646.872	21.651 ± 0.021	21.958 ± 0.031	22.098 ± 0.029
6773.210	21.622 ± 0.019	21.862 ± 0.031	22.132 ± 0.035

Continued on next page

Table A.1 – *Continued from previous page*

MJD	Image A	Image B	Image C
6773.217	21.591 ± 0.019	21.921 ± 0.027	22.062 ± 0.034
6777.215	21.666 ± 0.026	21.988 ± 0.027	22.118 ± 0.031
6788.186	21.572 ± 0.015	21.983 ± 0.028	22.111 ± 0.033
6788.193	21.597 ± 0.015	21.916 ± 0.019	22.160 ± 0.022
6788.201	21.566 ± 0.018	22.003 ± 0.020	22.133 ± 0.022
6802.187	21.551 ± 0.015	21.977 ± 0.028	22.077 ± 0.027
6802.195	21.592 ± 0.016	21.900 ± 0.021	22.154 ± 0.024
6802.202	21.547 ± 0.016	21.932 ± 0.023	22.170 ± 0.025
6815.173	21.556 ± 0.015	21.937 ± 0.024	22.146 ± 0.026
6815.181	21.570 ± 0.015	21.942 ± 0.015	22.113 ± 0.016
6815.188	21.565 ± 0.015	21.960 ± 0.015	22.112 ± 0.016
6835.176	21.614 ± 0.014	21.942 ± 0.015	22.101 ± 0.016
6835.184	21.584 ± 0.015	21.927 ± 0.014	22.076 ± 0.015
6835.191	21.571 ± 0.015	21.914 ± 0.014	22.080 ± 0.015
6847.162	21.584 ± 0.014	21.924 ± 0.015	22.117 ± 0.016
6847.169	21.574 ± 0.014	21.901 ± 0.015	22.022 ± 0.016
6847.179	21.589 ± 0.014	21.916 ± 0.015	22.062 ± 0.016
6864.105	21.584 ± 0.015	21.908 ± 0.016	22.060 ± 0.016
6864.112	21.601 ± 0.014	21.959 ± 0.015	22.017 ± 0.015
6864.120	21.608 ± 0.014	21.890 ± 0.015	21.979 ± 0.015
6874.056	21.610 ± 0.014	21.892 ± 0.015	22.022 ± 0.016
6874.063	21.612 ± 0.015	21.914 ± 0.015	21.950 ± 0.015
6874.070	21.588 ± 0.015	21.934 ± 0.014	21.952 ± 0.014
6894.020	21.610 ± 0.012	21.916 ± 0.015	21.926 ± 0.014
6894.028	21.592 ± 0.014	21.937 ± 0.014	21.963 ± 0.014
6894.035	21.599 ± 0.015	21.902 ± 0.014	21.903 ± 0.014
6918.088	21.576 ± 0.014	21.892 ± 0.014	21.943 ± 0.014
6918.096	21.565 ± 0.014	21.909 ± 0.018	21.951 ± 0.017
6918.103	21.563 ± 0.015	21.956 ± 0.018	21.915 ± 0.017
6928.011	21.619 ± 0.015	21.938 ± 0.019	21.953 ± 0.018
6928.019	21.620 ± 0.014	21.952 ± 0.014	21.956 ± 0.014
6928.026	21.625 ± 0.013	21.987 ± 0.015	21.944 ± 0.015
6944.979	21.600 ± 0.014	21.942 ± 0.014	21.959 ± 0.014
6944.986	21.628 ± 0.015	21.933 ± 0.015	21.923 ± 0.014
6944.993	21.625 ± 0.014	21.973 ± 0.014	21.960 ± 0.014
6973.943	21.683 ± 0.018	21.933 ± 0.015	21.900 ± 0.015
6973.950	21.627 ± 0.018	21.931 ± 0.024	21.699 ± 0.019
6973.958	21.524 ± 0.019	21.920 ± 0.024	21.726 ± 0.019
6986.896	21.643 ± 0.015	21.952 ± 0.027	21.709 ± 0.021
6986.903	21.642 ± 0.014	21.883 ± 0.018	21.654 ± 0.015
6986.911	21.623 ± 0.014	21.920 ± 0.017	21.683 ± 0.014
7007.822	21.707 ± 0.016	21.918 ± 0.017	21.668 ± 0.014
7137.209	21.680 ± 0.031	21.892 ± 0.019	21.680 ± 0.016
7137.213	21.635 ± 0.030	21.925 ± 0.022	21.681 ± 0.016
7137.217	21.663 ± 0.031	21.952 ± 0.021	21.672 ± 0.016
7141.226	21.651 ± 0.031	22.023 ± 0.032	21.741 ± 0.031
7142.194	21.667 ± 0.023	22.118 ± 0.033	21.772 ± 0.032

Continued on next page

Table A.1 – *Continued from previous page*

MJD	Image A	Image B	Image C
7142.198	21.700 ± 0.024	22.019 ± 0.030	21.788 ± 0.034
7142.202	21.677 ± 0.022	22.050 ± 0.030	21.743 ± 0.024
7143.207	21.696 ± 0.024	22.067 ± 0.027	21.744 ± 0.025
7143.211	21.744 ± 0.020	21.966 ± 0.026	21.782 ± 0.024
7143.214	21.696 ± 0.018	21.955 ± 0.035	21.772 ± 0.024
7158.197	21.795 ± 0.030	21.986 ± 0.016	21.809 ± 0.022
7158.204	21.750 ± 0.035	22.061 ± 0.015	21.742 ± 0.019
7169.188	21.750 ± 0.014	22.014 ± 0.017	21.734 ± 0.029
7169.195	21.775 ± 0.014	22.044 ± 0.015	21.747 ± 0.035
7169.203	21.800 ± 0.014	22.029 ± 0.016	21.822 ± 0.014
7191.154	21.771 ± 0.014	21.996 ± 0.016	21.824 ± 0.014
7191.161	21.777 ± 0.014	22.052 ± 0.014	21.826 ± 0.014
7191.168	21.783 ± 0.014	22.039 ± 0.015	21.818 ± 0.014
7196.183	21.784 ± 0.015	22.059 ± 0.015	21.822 ± 0.014
7196.190	21.809 ± 0.014	22.110 ± 0.022	21.857 ± 0.014
7196.197	21.807 ± 0.014	22.034 ± 0.025	21.828 ± 0.014
7218.080	21.794 ± 0.016	22.071 ± 0.023	21.817 ± 0.014
7218.087	21.763 ± 0.016	22.099 ± 0.025	21.819 ± 0.014
7218.094	21.777 ± 0.019	22.057 ± 0.025	21.740 ± 0.015
7225.041	21.764 ± 0.017	22.066 ± 0.016	21.731 ± 0.016
7225.048	21.760 ± 0.018	22.079 ± 0.014	21.767 ± 0.019
7225.055	21.778 ± 0.018	22.121 ± 0.015	21.767 ± 0.017
7256.088	21.687 ± 0.014	22.066 ± 0.015	21.744 ± 0.017
7258.077	21.725 ± 0.014	22.087 ± 0.017	21.794 ± 0.018
7258.084	21.697 ± 0.015	22.081 ± 0.021	21.748 ± 0.014
7258.091	21.696 ± 0.015	22.069 ± 0.024	21.746 ± 0.014
7260.148	21.691 ± 0.014	22.047 ± 0.015	21.723 ± 0.015
7260.155	21.687 ± 0.015	22.034 ± 0.022	21.733 ± 0.015
7260.162	21.670 ± 0.016	22.072 ± 0.023	21.763 ± 0.014
7270.997	21.675 ± 0.015	22.098 ± 0.022	21.749 ± 0.015
7278.155	21.670 ± 0.015	22.006 ± 0.016	21.748 ± 0.016
7278.162	21.670 ± 0.015	22.026 ± 0.017	21.753 ± 0.015
7278.169	21.646 ± 0.015	21.995 ± 0.017	21.756 ± 0.016
7302.085	21.680 ± 0.014	21.955 ± 0.014	21.766 ± 0.016
7302.092	21.700 ± 0.014	22.015 ± 0.015	21.722 ± 0.015
7302.099	21.671 ± 0.014	22.036 ± 0.016	21.726 ± 0.014
7330.022	21.727 ± 0.015	21.967 ± 0.018	21.719 ± 0.014
7330.030	21.708 ± 0.014	22.001 ± 0.014	21.674 ± 0.014
7330.037	21.684 ± 0.014	21.981 ± 0.014	21.545 ± 0.014
7331.963	21.693 ± 0.014	21.984 ± 0.015	21.552 ± 0.015
7333.897	21.736 ± 0.015	22.106 ± 0.019	21.577 ± 0.015
7333.904	21.705 ± 0.015	22.063 ± 0.018	21.534 ± 0.014
7333.911	21.670 ± 0.014	22.039 ± 0.019	21.525 ± 0.013
7397.827	21.701 ± 0.014	21.935 ± 0.023	21.515 ± 0.013
7397.834	21.696 ± 0.014	21.926 ± 0.025	21.518 ± 0.015
7397.842	21.718 ± 0.015	21.968 ± 0.021	21.281 ± 0.016
7513.177	21.637 ± 0.016	21.855 ± 0.024	21.306 ± 0.018

Continued on next page

Table A.1 – *Continued from previous page*

MJD	Image A	Image B	Image C
7513.184	21.656 ± 0.018	21.857 ± 0.028	21.173 ± 0.015
7513.191	21.650 ± 0.015	21.892 ± 0.028	21.183 ± 0.014
7525.179	21.630 ± 0.018	21.959 ± 0.020	21.199 ± 0.014
7525.186	21.647 ± 0.021	21.930 ± 0.017	21.224 ± 0.014
7525.194	21.615 ± 0.020	21.912 ± 0.018	21.251 ± 0.014
7546.124	21.586 ± 0.015	21.939 ± 0.015	21.226 ± 0.014
7546.131	21.600 ± 0.014	21.934 ± 0.016	21.192 ± 0.014
7546.138	21.597 ± 0.014	21.964 ± 0.018	21.186 ± 0.014
7550.186	21.599 ± 0.014	21.936 ± 0.014	21.191 ± 0.015
7550.193	21.583 ± 0.014	21.954 ± 0.014	21.184 ± 0.014
7550.200	21.575 ± 0.014	21.931 ± 0.014	21.195 ± 0.015
7573.135	21.448 ± 0.008	21.956 ± 0.017	21.122 ± 0.014
7573.142	21.468 ± 0.008	21.925 ± 0.022	21.086 ± 0.014
7573.149	21.449 ± 0.009	21.894 ± 0.014	21.100 ± 0.012
7585.208	21.437 ± 0.015	21.900 ± 0.015	21.093 ± 0.008
7585.215	21.399 ± 0.015	21.871 ± 0.015	21.106 ± 0.013
7585.223	21.413 ± 0.027	21.851 ± 0.015	21.151 ± 0.008
7599.085	21.454 ± 0.014	21.852 ± 0.016	21.131 ± 0.008
7599.092	21.425 ± 0.014	21.867 ± 0.016	21.154 ± 0.008
7611.104	21.501 ± 0.015	21.769 ± 0.015	21.105 ± 0.009
7611.111	21.480 ± 0.014	21.774 ± 0.014	21.080 ± 0.014
7611.118	21.494 ± 0.014	21.758 ± 0.014	21.108 ± 0.021
7627.999	21.446 ± 0.015	21.768 ± 0.015	21.055 ± 0.008
7628.007	21.457 ± 0.015	21.781 ± 0.015	21.050 ± 0.008
7628.014	21.448 ± 0.014	21.769 ± 0.018	21.053 ± 0.008
7640.059	21.451 ± 0.008	21.785 ± 0.026	21.003 ± 0.008
7640.066	21.460 ± 0.008	21.813 ± 0.014	21.019 ± 0.008
7640.073	21.434 ± 0.008	21.792 ± 0.014	21.026 ± 0.008
7651.927	21.407 ± 0.015	21.785 ± 0.015	20.989 ± 0.008
7651.934	21.355 ± 0.014	21.784 ± 0.015	20.994 ± 0.008
7651.941	21.394 ± 0.017	21.778 ± 0.015	20.970 ± 0.008
7658.989	21.327 ± 0.008	21.791 ± 0.014	20.903 ± 0.008
7658.997	21.321 ± 0.008	21.833 ± 0.014	20.906 ± 0.008
7659.004	21.319 ± 0.008	21.618 ± 0.016	20.932 ± 0.008
7662.028	21.311 ± 0.014	21.782 ± 0.017	20.907 ± 0.012
7662.035	21.306 ± 0.014	21.565 ± 0.019	20.923 ± 0.014
7662.042	21.303 ± 0.013	21.578 ± 0.016	20.946 ± 0.008
7670.047	21.230 ± 0.008	21.568 ± 0.014	20.946 ± 0.008
7670.061	21.216 ± 0.008	21.576 ± 0.030	20.950 ± 0.008
7691.958	21.205 ± 0.014	21.602 ± 0.019	20.963 ± 0.008
7691.965	21.213 ± 0.015	21.615 ± 0.017	20.944 ± 0.008
7691.973	21.202 ± 0.015	21.592 ± 0.020	20.935 ± 0.008
7720.842	21.248 ± 0.015	21.586 ± 0.019	20.941 ± 0.008
7720.849	21.243 ± 0.014	21.615 ± 0.016	20.956 ± 0.008
7720.856	21.261 ± 0.014	21.595 ± 0.014	20.986 ± 0.008
7770.823	21.273 ± 0.022	21.639 ± 0.014	20.984 ± 0.010
7770.831	21.254 ± 0.014	21.617 ± 0.014	20.979 ± 0.011

Continued on next page

Table A.1 – *Continued from previous page*

MJD	Image A	Image B	Image C
7770.838	21.246 ± 0.014	21.640 ± 0.014	21.104 ± 0.014
7867.199	21.295 ± 0.015	21.619 ± 0.014	21.105 ± 0.015
7867.206	21.285 ± 0.015	21.635 ± 0.014	21.106 ± 0.010
7867.213	21.297 ± 0.014	21.619 ± 0.014	21.164 ± 0.015
7879.181	21.338 ± 0.014	21.634 ± 0.014	21.164 ± 0.017
7879.188	21.336 ± 0.015	21.642 ± 0.014	21.172 ± 0.017
7879.195	21.301 ± 0.015	21.650 ± 0.014	21.311 ± 0.022
7897.173	21.323 ± 0.013	21.652 ± 0.014	21.323 ± 0.015
7897.180	21.331 ± 0.013	21.666 ± 0.014	21.319 ± 0.014
7897.188	21.322 ± 0.012	21.693 ± 0.014	21.038 ± 0.014
7904.156	21.304 ± 0.013	21.677 ± 0.014	21.022 ± 0.014
7924.098	21.256 ± 0.010	21.675 ± 0.014	21.027 ± 0.015
7924.105	21.265 ± 0.011	21.650 ± 0.014	21.080 ± 0.014
7924.112	21.261 ± 0.008	21.646 ± 0.014	21.039 ± 0.012
7931.152	21.302 ± 0.014	21.649 ± 0.014	21.058 ± 0.008
7931.159	21.293 ± 0.013	21.651 ± 0.014	21.047 ± 0.008
7931.167	21.284 ± 0.013	21.610 ± 0.014	21.054 ± 0.008
7937.136	21.280 ± 0.013	21.592 ± 0.014	21.074 ± 0.008
7937.143	21.293 ± 0.013	21.601 ± 0.014	21.075 ± 0.008
7937.151	21.285 ± 0.013	21.639 ± 0.018	21.187 ± 0.008
7953.083	21.236 ± 0.012	21.656 ± 0.018	21.215 ± 0.008
7953.091	21.274 ± 0.014	21.603 ± 0.016	21.189 ± 0.008
7953.098	21.261 ± 0.014	21.605 ± 0.015	21.231 ± 0.012
7963.172	21.264 ± 0.009	21.632 ± 0.015	21.231 ± 0.011
7963.179	21.266 ± 0.011	21.607 ± 0.015	21.273 ± 0.012
7963.186	21.252 ± 0.014	21.595 ± 0.018	21.247 ± 0.011
7985.966	21.238 ± 0.014	21.617 ± 0.017	21.274 ± 0.011
7985.973	21.250 ± 0.014	21.617 ± 0.017	21.299 ± 0.013
7985.980	21.227 ± 0.014	21.608 ± 0.015	21.289 ± 0.014
8015.883	21.156 ± 0.015	21.595 ± 0.015	21.298 ± 0.014
8015.890	21.142 ± 0.015	21.601 ± 0.014	21.332 ± 0.010
8015.897	21.155 ± 0.014	21.578 ± 0.014	21.307 ± 0.012
8024.990	21.103 ± 0.014	21.552 ± 0.014	21.343 ± 0.014
8024.997	21.116 ± 0.014	21.563 ± 0.014	21.371 ± 0.014
8025.004	21.104 ± 0.014	21.585 ± 0.014	21.373 ± 0.014
8026.885	21.098 ± 0.029	21.409 ± 0.017	21.396 ± 0.014
8026.892	21.119 ± 0.029	21.436 ± 0.018	21.400 ± 0.014
8026.900	21.113 ± 0.028	21.352 ± 0.022	21.390 ± 0.014
8043.987	20.936 ± 0.008	21.333 ± 0.018	21.428 ± 0.015
8043.994	20.955 ± 0.008	21.327 ± 0.020	21.464 ± 0.015
8044.001	20.955 ± 0.008	21.371 ± 0.032	21.479 ± 0.015
8051.955	20.948 ± 0.008	21.318 ± 0.032	21.366 ± 0.034
8051.962	20.945 ± 0.008	21.256 ± 0.019	21.488 ± 0.034
8051.969	20.956 ± 0.008	21.182 ± 0.027	21.507 ± 0.014
8073.927	20.761 ± 0.014	21.117 ± 0.015	21.476 ± 0.015
8073.934	20.757 ± 0.014	21.120 ± 0.014	21.500 ± 0.015
8073.942	20.689 ± 0.030	21.121 ± 0.014	21.557 ± 0.014

Continued on next page

Table A.1 – *Continued from previous page*

MJD	Image A	Image B	Image C
8079.980	20.706 ± 0.014	21.085 ± 0.014	21.513 ± 0.014
8079.987	20.728 ± 0.014	21.095 ± 0.015	21.512 ± 0.014
8079.994	20.707 ± 0.015	21.038 ± 0.019	21.526 ± 0.014
8093.894	20.692 ± 0.015	21.032 ± 0.019	21.574 ± 0.017
8110.832	20.706 ± 0.016	21.172 ± 0.014	21.565 ± 0.017
8122.838	20.708 ± 0.015	21.196 ± 0.014	21.603 ± 0.022
8122.845	20.702 ± 0.014	21.183 ± 0.016	21.554 ± 0.017
8122.852	20.686 ± 0.014	21.085 ± 0.015	21.566 ± 0.019
8130.847	20.741 ± 0.008	21.133 ± 0.014	21.504 ± 0.033
8136.845	20.723 ± 0.014	21.120 ± 0.015	21.536 ± 0.034
8136.852	20.705 ± 0.014	21.043 ± 0.011	21.573 ± 0.019
8234.226	20.636 ± 0.015	21.049 ± 0.012	21.533 ± 0.026
8249.201	20.583 ± 0.008	21.052 ± 0.010	21.502 ± 0.032
8249.208	20.575 ± 0.008	20.996 ± 0.015	21.669 ± 0.032
8262.179	20.607 ± 0.008	20.968 ± 0.014	21.612 ± 0.031
8262.186	20.595 ± 0.008	20.977 ± 0.013	21.586 ± 0.030
8262.193	20.607 ± 0.008	20.979 ± 0.014	21.670 ± 0.020
8281.142	20.606 ± 0.013	21.003 ± 0.014	21.668 ± 0.018
8281.150	20.623 ± 0.014	21.026 ± 0.014	21.630 ± 0.018
8318.180	20.495 ± 0.008	21.022 ± 0.014	21.685 ± 0.015
8318.187	20.466 ± 0.008	21.019 ± 0.008	21.683 ± 0.015
8318.194	20.485 ± 0.008	21.037 ± 0.008	21.709 ± 0.016
8323.162	20.468 ± 0.008	21.022 ± 0.008	21.666 ± 0.026
8323.170	20.472 ± 0.008	20.953 ± 0.008	21.734 ± 0.027
8323.177	20.460 ± 0.008	20.906 ± 0.008	21.762 ± 0.017
8341.179	20.375 ± 0.008	20.919 ± 0.008	21.781 ± 0.024
8341.186	20.364 ± 0.008	20.866 ± 0.008	21.802 ± 0.017
8341.193	20.378 ± 0.008	20.862 ± 0.008	21.779 ± 0.019
8349.126	20.412 ± 0.008	20.881 ± 0.008	21.828 ± 0.025
8349.133	20.390 ± 0.008	20.827 ± 0.015	21.796 ± 0.029
8349.140	20.401 ± 0.008	20.818 ± 0.015	21.739 ± 0.030
8366.065	20.421 ± 0.008	20.817 ± 0.015	21.720 ± 0.030
8366.072	20.429 ± 0.008	20.825 ± 0.008	21.802 ± 0.015
8366.079	20.435 ± 0.008	20.804 ± 0.012	21.824 ± 0.015
8391.083	20.492 ± 0.015	20.824 ± 0.013	21.815 ± 0.015
8391.090	20.465 ± 0.014	20.811 ± 0.008	21.811 ± 0.023
8408.031	20.527 ± 0.008	20.818 ± 0.008	21.823 ± 0.021
8408.039	20.521 ± 0.008	20.807 ± 0.008	21.806 ± 0.023
8408.046	20.536 ± 0.008	20.912 ± 0.008	21.659 ± 0.015
8426.963	20.636 ± 0.008	20.915 ± 0.008	21.664 ± 0.015
8426.970	20.615 ± 0.008	20.925 ± 0.008	21.666 ± 0.016
8426.978	20.613 ± 0.008	20.931 ± 0.008	21.663 ± 0.017
8452.895	20.770 ± 0.008	21.054 ± 0.008	21.628 ± 0.017
8452.902	20.742 ± 0.008	21.052 ± 0.008	21.658 ± 0.017
8452.909	20.734 ± 0.008	21.041 ± 0.008	21.629 ± 0.014
8454.900	20.762 ± 0.008	21.068 ± 0.021	21.618 ± 0.014
8454.908	20.776 ± 0.008	21.076 ± 0.021	21.661 ± 0.014

Continued on next page

Table A.1 – *Continued from previous page*

MJD	Image A	Image B	Image C
8454.915	20.765 ± 0.008	21.076 ± 0.020	21.623 ± 0.014

Note. The Modern Julian Days (MJD) column gives the date of observation relative to MJD = 50 000.

Table A.2

R-band Photometry of the Four Images in PS1 J0147+4630

MJD	Image A	Image B	Image C	Image D
7985.157	15.959 ± 0.005	16.199 ± 0.006	16.629 ± 0.007	18.227 ± 0.013
7985.157	15.964 ± 0.006	16.204 ± 0.006	16.623 ± 0.007	18.233 ± 0.008
7985.158	15.968 ± 0.005	16.201 ± 0.005	16.638 ± 0.006	18.206 ± 0.010
7997.166	15.979 ± 0.012	16.183 ± 0.016	16.657 ± 0.020	18.222 ± 0.068
7997.167	15.979 ± 0.008	16.228 ± 0.009	16.649 ± 0.011	18.290 ± 0.026
7997.167	15.956 ± 0.007	16.208 ± 0.008	16.639 ± 0.011	18.231 ± 0.027
7997.169	15.955 ± 0.007	16.221 ± 0.008	16.637 ± 0.009	18.282 ± 0.022
7997.170	15.960 ± 0.010	16.179 ± 0.012	16.624 ± 0.019	18.147 ± 0.040
7997.170	15.948 ± 0.012	16.182 ± 0.012	16.595 ± 0.018	18.067 ± 0.041
7998.199	15.940 ± 0.004	16.212 ± 0.004	16.665 ± 0.005	18.208 ± 0.008
7998.200	15.939 ± 0.006	16.193 ± 0.007	16.620 ± 0.008	18.219 ± 0.014
7998.201	15.943 ± 0.004	16.190 ± 0.005	16.631 ± 0.005	18.197 ± 0.008
8007.161	15.967 ± 0.006	16.210 ± 0.007	16.650 ± 0.007	18.236 ± 0.011
8007.161	15.963 ± 0.005	16.204 ± 0.006	16.631 ± 0.006	18.258 ± 0.010
8007.162	15.957 ± 0.006	16.207 ± 0.007	16.628 ± 0.007	18.217 ± 0.012
8013.142	15.962 ± 0.006	16.207 ± 0.006	16.623 ± 0.006	18.230 ± 0.008
8013.143	15.952 ± 0.006	16.205 ± 0.007	16.628 ± 0.006	18.210 ± 0.010
8013.144	15.963 ± 0.005	16.193 ± 0.005	16.630 ± 0.005	18.224 ± 0.010
8018.064	15.962 ± 0.003	16.205 ± 0.003	16.641 ± 0.005	18.219 ± 0.008
8018.065	15.963 ± 0.005	16.218 ± 0.003	16.625 ± 0.005	18.207 ± 0.010
8018.066	15.959 ± 0.005	16.202 ± 0.006	16.617 ± 0.006	18.210 ± 0.009
8018.066	15.959 ± 0.005	16.202 ± 0.006	16.617 ± 0.006	18.210 ± 0.009
8024.939	15.948 ± 0.006	16.211 ± 0.006	16.625 ± 0.006	18.241 ± 0.011
8024.939	15.958 ± 0.006	16.211 ± 0.006	16.624 ± 0.007	18.232 ± 0.011
8024.940	15.963 ± 0.007	16.205 ± 0.005	16.639 ± 0.009	18.226 ± 0.013
8044.009	15.963 ± 0.008	16.215 ± 0.011	16.653 ± 0.010	18.242 ± 0.011
8044.009	15.957 ± 0.010	16.185 ± 0.012	16.636 ± 0.010	18.231 ± 0.015
8044.010	15.960 ± 0.006	16.221 ± 0.007	16.646 ± 0.007	18.223 ± 0.010
8052.130	15.952 ± 0.007	16.212 ± 0.008	16.610 ± 0.010	18.209 ± 0.017
8052.131	15.952 ± 0.006	16.207 ± 0.008	16.634 ± 0.009	18.197 ± 0.016
8052.132	15.961 ± 0.007	16.230 ± 0.007	16.681 ± 0.010	18.230 ± 0.021
8055.948	15.972 ± 0.011	16.216 ± 0.013	16.636 ± 0.012	18.219 ± 0.017
8055.949	15.967 ± 0.007	16.213 ± 0.007	16.646 ± 0.008	18.252 ± 0.013
8055.949	15.958 ± 0.009	16.220 ± 0.009	16.630 ± 0.009	18.240 ± 0.011
8074.948	15.950 ± 0.005	16.209 ± 0.007	16.619 ± 0.005	18.230 ± 0.010
8074.948	15.932 ± 0.004	16.210 ± 0.005	16.618 ± 0.005	18.202 ± 0.009
8074.949	15.956 ± 0.004	16.206 ± 0.006	16.631 ± 0.007	18.226 ± 0.010

Continued on next page

Table A.2 – *Continued from previous page*

MJD	Image A	Image B	Image C	Image D
8092.872	15.934 ± 0.008	16.191 ± 0.008	16.597 ± 0.010	18.269 ± 0.014
8092.872	15.942 ± 0.007	16.196 ± 0.008	16.594 ± 0.008	18.216 ± 0.013
8092.873	15.953 ± 0.005	16.174 ± 0.007	16.614 ± 0.008	18.232 ± 0.015
8094.051	15.940 ± 0.006	16.204 ± 0.005	16.604 ± 0.007	18.199 ± 0.013
8094.052	15.936 ± 0.004	16.201 ± 0.006	16.616 ± 0.006	18.221 ± 0.012
8094.053	15.946 ± 0.005	16.177 ± 0.005	16.631 ± 0.007	18.211 ± 0.011
8116.953	15.983 ± 0.017	16.208 ± 0.024	16.622 ± 0.032	18.143 ± 0.085
8116.953	15.929 ± 0.021	16.119 ± 0.018	16.611 ± 0.040	18.349 ± 0.175
8116.954	16.032 ± 0.042	16.112 ± 0.042	16.767 ± 0.087	17.600 ± 0.158
8131.833	15.956 ± 0.005	16.231 ± 0.005	16.645 ± 0.005	18.206 ± 0.009
8131.833	15.968 ± 0.004	16.207 ± 0.004	16.629 ± 0.005	18.230 ± 0.010
8131.834	15.972 ± 0.005	16.230 ± 0.005	16.633 ± 0.005	18.226 ± 0.012
8137.927	15.980 ± 0.006	16.225 ± 0.006	16.642 ± 0.007	18.227 ± 0.011
8137.928	15.968 ± 0.005	16.233 ± 0.005	16.640 ± 0.005	18.229 ± 0.011
8137.928	15.973 ± 0.004	16.239 ± 0.004	16.640 ± 0.005	18.205 ± 0.008
8161.842	15.992 ± 0.007	16.269 ± 0.010	16.621 ± 0.010	18.192 ± 0.021
8161.843	15.990 ± 0.007	16.215 ± 0.007	16.616 ± 0.008	18.260 ± 0.021
8161.843	16.015 ± 0.005	16.240 ± 0.007	16.656 ± 0.006	18.325 ± 0.021
8196.840	15.961 ± 0.011	16.228 ± 0.010	16.797 ± 0.020	18.419 ± 0.070
8196.841	16.021 ± 0.010	16.349 ± 0.020	16.542 ± 0.016	18.108 ± 0.056
8196.841	15.967 ± 0.008	16.259 ± 0.010	16.740 ± 0.021	17.980 ± 0.035
8197.838	16.008 ± 0.008	16.252 ± 0.011	16.679 ± 0.019	18.427 ± 0.058
8197.839	16.023 ± 0.009	16.320 ± 0.012	16.742 ± 0.017	18.393 ± 0.053
8197.840	16.068 ± 0.007	16.290 ± 0.007	16.692 ± 0.010	18.439 ± 0.035
8270.199	16.014 ± 0.005	16.275 ± 0.005	16.632 ± 0.008	18.227 ± 0.020
8270.200	15.999 ± 0.005	16.256 ± 0.005	16.643 ± 0.006	18.156 ± 0.014
8270.201	16.019 ± 0.008	16.262 ± 0.008	16.645 ± 0.013	18.273 ± 0.017
8274.184	16.023 ± 0.007	16.305 ± 0.007	16.650 ± 0.009	18.258 ± 0.014
8274.184	15.999 ± 0.008	16.277 ± 0.008	16.625 ± 0.010	18.207 ± 0.013
8274.185	16.011 ± 0.006	16.255 ± 0.006	16.681 ± 0.013	18.266 ± 0.014
8274.191	16.004 ± 0.007	16.271 ± 0.009	16.681 ± 0.009	18.236 ± 0.014
8274.192	15.990 ± 0.007	16.261 ± 0.011	16.626 ± 0.008	18.199 ± 0.016
8274.192	15.986 ± 0.008	16.273 ± 0.010	16.666 ± 0.010	18.245 ± 0.015
8278.204	16.013 ± 0.005	16.252 ± 0.005	16.654 ± 0.005	18.229 ± 0.011
8278.205	16.018 ± 0.005	16.264 ± 0.006	16.657 ± 0.006	18.219 ± 0.011
8278.205	16.027 ± 0.005	16.259 ± 0.006	16.651 ± 0.007	18.262 ± 0.011
8279.204	16.003 ± 0.005	16.270 ± 0.005	16.640 ± 0.007	18.238 ± 0.015
8296.204	15.997 ± 0.008	16.246 ± 0.008	16.627 ± 0.009	18.202 ± 0.018
8296.204	15.990 ± 0.007	16.248 ± 0.007	16.606 ± 0.009	18.253 ± 0.017
8296.205	15.985 ± 0.006	16.236 ± 0.007	16.608 ± 0.008	18.203 ± 0.021
8304.186	15.995 ± 0.005	16.236 ± 0.006	16.631 ± 0.008	18.221 ± 0.022
8304.187	15.988 ± 0.007	16.239 ± 0.008	16.616 ± 0.009	18.247 ± 0.020
8304.187	15.992 ± 0.006	16.228 ± 0.008	16.625 ± 0.008	18.246 ± 0.024
8305.191	16.009 ± 0.005	16.269 ± 0.006	16.635 ± 0.006	18.254 ± 0.011
8305.191	15.997 ± 0.006	16.253 ± 0.006	16.625 ± 0.007	18.222 ± 0.014
8305.192	16.012 ± 0.006	16.235 ± 0.007	16.624 ± 0.012	18.335 ± 0.026
8307.145	16.005 ± 0.007	16.253 ± 0.007	16.588 ± 0.008	18.219 ± 0.014

Continued on next page

Table A.2 – *Continued from previous page*

MJD	Image A	Image B	Image C	Image D
8307.145	15.990 ± 0.008	16.246 ± 0.008	16.622 ± 0.009	18.299 ± 0.014
8307.146	16.003 ± 0.006	16.252 ± 0.007	16.610 ± 0.010	18.292 ± 0.015
8312.158	16.008 ± 0.008	16.259 ± 0.011	16.606 ± 0.010	18.275 ± 0.013
8312.158	15.996 ± 0.007	16.243 ± 0.007	16.587 ± 0.007	18.235 ± 0.012
8312.159	15.971 ± 0.009	16.240 ± 0.008	16.677 ± 0.014	18.267 ± 0.019
8317.169	15.978 ± 0.006	16.204 ± 0.006	16.611 ± 0.008	18.272 ± 0.011
8317.170	15.982 ± 0.007	16.222 ± 0.008	16.601 ± 0.010	18.215 ± 0.013
8317.170	15.987 ± 0.006	16.208 ± 0.006	16.599 ± 0.010	18.239 ± 0.012
8319.189	15.974 ± 0.007	16.222 ± 0.007	16.592 ± 0.009	18.231 ± 0.012
8319.189	15.984 ± 0.005	16.224 ± 0.004	16.597 ± 0.006	18.247 ± 0.010
8319.190	15.990 ± 0.004	16.225 ± 0.004	16.606 ± 0.005	18.274 ± 0.009
8323.217	15.988 ± 0.006	16.227 ± 0.006	16.611 ± 0.008	18.304 ± 0.011
8323.218	15.988 ± 0.007	16.221 ± 0.006	16.608 ± 0.007	18.280 ± 0.013
8323.218	15.983 ± 0.004	16.234 ± 0.004	16.596 ± 0.005	18.283 ± 0.009
8325.198	15.997 ± 0.005	16.229 ± 0.005	16.631 ± 0.007	18.294 ± 0.020
8325.199	15.986 ± 0.005	16.230 ± 0.005	16.659 ± 0.009	18.330 ± 0.024
8325.199	16.004 ± 0.003	16.229 ± 0.004	16.602 ± 0.006	18.277 ± 0.015
8334.173	15.997 ± 0.008	16.246 ± 0.008	16.613 ± 0.008	18.313 ± 0.013
8334.174	15.987 ± 0.011	16.233 ± 0.010	16.611 ± 0.013	18.308 ± 0.019
8334.175	15.994 ± 0.011	16.243 ± 0.010	16.602 ± 0.011	18.291 ± 0.014
8340.187	16.003 ± 0.013	16.248 ± 0.013	16.617 ± 0.014	18.332 ± 0.015
8340.188	16.006 ± 0.010	16.243 ± 0.009	16.625 ± 0.011	18.322 ± 0.016
8340.188	15.974 ± 0.011	16.214 ± 0.012	16.609 ± 0.010	18.308 ± 0.014
8349.168	16.031 ± 0.011	16.282 ± 0.011	16.691 ± 0.015	18.347 ± 0.015
8349.169	15.998 ± 0.008	16.248 ± 0.008	16.627 ± 0.009	18.296 ± 0.013
8349.170	16.011 ± 0.007	16.257 ± 0.006	16.662 ± 0.008	18.329 ± 0.011
8356.127	15.993 ± 0.011	16.244 ± 0.010	16.634 ± 0.013	18.300 ± 0.022
8356.127	15.998 ± 0.013	16.239 ± 0.012	16.623 ± 0.014	18.331 ± 0.021
8356.128	16.012 ± 0.012	16.239 ± 0.011	16.642 ± 0.015	18.364 ± 0.024
8366.216	16.000 ± 0.009	16.261 ± 0.009	16.630 ± 0.009	18.317 ± 0.012
8366.216	15.985 ± 0.008	16.264 ± 0.008	16.617 ± 0.008	18.293 ± 0.010
8366.217	15.987 ± 0.005	16.232 ± 0.005	16.630 ± 0.008	18.329 ± 0.010
8369.112	15.999 ± 0.011	16.224 ± 0.014	16.632 ± 0.012	18.305 ± 0.015
8369.113	16.007 ± 0.014	16.235 ± 0.014	16.613 ± 0.012	18.304 ± 0.012
8369.113	15.996 ± 0.012	16.229 ± 0.012	16.638 ± 0.014	18.326 ± 0.014
8373.209	15.990 ± 0.009	16.243 ± 0.010	16.619 ± 0.010	18.316 ± 0.011
8373.209	15.969 ± 0.008	16.221 ± 0.012	16.655 ± 0.008	18.330 ± 0.011
8373.210	15.998 ± 0.009	16.225 ± 0.009	16.638 ± 0.012	18.325 ± 0.015
8379.177	15.964 ± 0.015	16.252 ± 0.015	16.596 ± 0.018	18.305 ± 0.015
8379.178	15.969 ± 0.009	16.218 ± 0.010	16.599 ± 0.011	18.306 ± 0.012
8379.178	15.962 ± 0.010	16.228 ± 0.013	16.615 ± 0.015	18.297 ± 0.015
8384.077	15.952 ± 0.006	16.228 ± 0.006	16.602 ± 0.008	18.299 ± 0.017
8384.078	15.951 ± 0.005	16.239 ± 0.005	16.618 ± 0.008	18.337 ± 0.018
8384.078	15.973 ± 0.007	16.322 ± 0.009	16.470 ± 0.008	18.324 ± 0.023
8391.129	15.948 ± 0.008	16.198 ± 0.010	16.587 ± 0.008	18.342 ± 0.014
8391.130	15.963 ± 0.005	16.217 ± 0.005	16.576 ± 0.006	18.332 ± 0.011
8391.130	15.957 ± 0.008	16.215 ± 0.009	16.559 ± 0.010	18.322 ± 0.015

Continued on next page

Table A.2 – *Continued from previous page*

MJD	Image A	Image B	Image C	Image D
8395.109	15.996 ± 0.021	16.250 ± 0.020	16.625 ± 0.018	18.335 ± 0.021
8395.110	15.991 ± 0.015	16.217 ± 0.018	16.579 ± 0.016	18.239 ± 0.022
8395.110	15.980 ± 0.018	16.232 ± 0.022	16.608 ± 0.015	18.309 ± 0.022
8396.927	15.991 ± 0.014	16.255 ± 0.015	16.633 ± 0.018	18.278 ± 0.016
8396.927	15.963 ± 0.007	16.200 ± 0.005	16.608 ± 0.009	18.316 ± 0.011
8408.140	15.975 ± 0.008	16.230 ± 0.008	16.577 ± 0.010	18.310 ± 0.012
8408.141	15.954 ± 0.006	16.225 ± 0.008	16.571 ± 0.007	18.338 ± 0.015
8408.142	15.991 ± 0.007	16.237 ± 0.008	16.594 ± 0.007	18.338 ± 0.012
8410.129	15.926 ± 0.008	16.246 ± 0.010	16.501 ± 0.012	18.339 ± 0.033
8410.129	19.013 ± 0.180	15.637 ± 0.014	16.035 ± 0.011	18.292 ± 0.055
8410.130	15.919 ± 0.013	16.382 ± 0.017	16.359 ± 0.014	18.683 ± 0.089
8427.005	15.939 ± 0.007	16.197 ± 0.007	16.553 ± 0.008	18.292 ± 0.012
8427.007	15.934 ± 0.009	16.196 ± 0.010	16.317 ± 0.030	18.194 ± 0.010
8429.099	15.961 ± 0.012	16.188 ± 0.012	16.564 ± 0.011	18.305 ± 0.010
8429.099	15.951 ± 0.009	16.197 ± 0.009	16.563 ± 0.008	18.318 ± 0.013
8429.100	15.960 ± 0.006	16.207 ± 0.006	16.562 ± 0.008	18.336 ± 0.010
8452.887	15.955 ± 0.006	16.197 ± 0.006	16.564 ± 0.006	18.268 ± 0.010
8452.888	15.944 ± 0.006	16.195 ± 0.006	16.567 ± 0.007	18.267 ± 0.011
8452.888	15.949 ± 0.009	16.194 ± 0.008	16.561 ± 0.009	18.287 ± 0.012
8454.979	15.931 ± 0.004	16.196 ± 0.006	16.546 ± 0.006	18.235 ± 0.011
8454.980	15.923 ± 0.005	16.213 ± 0.005	16.547 ± 0.005	18.246 ± 0.009
8454.981	15.927 ± 0.005	16.198 ± 0.007	16.543 ± 0.006	18.237 ± 0.010
8458.906	15.833 ± 0.091	16.230 ± 0.110	17.057 ± 0.317	17.235 ± 0.385
8463.860	15.947 ± 0.008	16.195 ± 0.008	16.551 ± 0.008	18.262 ± 0.013
8463.861	15.956 ± 0.009	16.213 ± 0.008	16.561 ± 0.008	18.252 ± 0.013
8463.862	15.948 ± 0.008	16.217 ± 0.010	16.567 ± 0.007	18.272 ± 0.010
8463.867	15.959 ± 0.006	16.208 ± 0.006	16.559 ± 0.007	18.288 ± 0.010
8463.867	15.947 ± 0.011	16.196 ± 0.012	16.557 ± 0.011	18.252 ± 0.014
8463.868	15.950 ± 0.009	16.215 ± 0.010	16.567 ± 0.010	18.277 ± 0.012
8480.869	15.882 ± 0.006	16.314 ± 0.007	16.469 ± 0.008	18.226 ± 0.020
8480.870	15.937 ± 0.004	16.223 ± 0.005	16.505 ± 0.006	18.271 ± 0.010
8480.871	15.933 ± 0.003	16.201 ± 0.004	16.552 ± 0.004	18.268 ± 0.010
8480.872	15.924 ± 0.004	16.180 ± 0.004	16.628 ± 0.005	18.250 ± 0.013
8480.872	15.938 ± 0.005	16.201 ± 0.006	16.534 ± 0.005	18.253 ± 0.012
8481.905	15.957 ± 0.012	16.213 ± 0.013	16.538 ± 0.011	18.257 ± 0.015
8481.906	15.954 ± 0.011	16.208 ± 0.014	16.553 ± 0.010	18.242 ± 0.014
8481.906	15.972 ± 0.013	16.204 ± 0.014	16.559 ± 0.012	18.283 ± 0.014
8484.880	15.943 ± 0.006	16.198 ± 0.005	16.531 ± 0.006	18.257 ± 0.009
8484.880	15.926 ± 0.004	16.203 ± 0.005	16.510 ± 0.006	18.225 ± 0.008
8484.881	15.942 ± 0.004	16.179 ± 0.005	16.536 ± 0.005	18.263 ± 0.007
8489.917	15.907 ± 0.021	16.176 ± 0.023	16.608 ± 0.038	17.982 ± 0.084
8489.918	15.990 ± 0.025	16.104 ± 0.032	16.687 ± 0.065	18.646 ± 0.246
8489.918	15.917 ± 0.024	16.201 ± 0.029	16.515 ± 0.044	17.971 ± 0.120
8495.834	15.929 ± 0.004	16.194 ± 0.005	16.519 ± 0.006	18.260 ± 0.012
8495.834	15.936 ± 0.005	16.187 ± 0.006	16.547 ± 0.007	18.243 ± 0.014
8495.835	15.932 ± 0.005	16.197 ± 0.006	16.532 ± 0.006	18.241 ± 0.010
8497.840	15.930 ± 0.004	16.189 ± 0.004	16.532 ± 0.006	18.260 ± 0.009

Continued on next page

Table A.2 – *Continued from previous page*

MJD	Image A	Image B	Image C	Image D
8497.841	15.903 ± 0.004	16.250 ± 0.005	16.482 ± 0.006	18.187 ± 0.014
8497.842	15.914 ± 0.005	16.191 ± 0.005	16.542 ± 0.006	18.260 ± 0.011
8502.855	15.934 ± 0.009	16.203 ± 0.010	16.537 ± 0.009	18.231 ± 0.016
8502.856	15.945 ± 0.006	16.204 ± 0.006	16.523 ± 0.008	18.262 ± 0.014
8502.857	15.948 ± 0.006	16.186 ± 0.006	16.528 ± 0.006	18.245 ± 0.016
8506.874	15.920 ± 0.004	16.176 ± 0.005	16.501 ± 0.005	18.207 ± 0.011
8506.874	15.916 ± 0.003	16.174 ± 0.004	16.501 ± 0.003	18.192 ± 0.008
8506.876	15.925 ± 0.007	16.187 ± 0.008	16.496 ± 0.007	18.233 ± 0.011
8508.915	15.939 ± 0.003	16.191 ± 0.003	16.526 ± 0.005	18.268 ± 0.008
8508.915	15.931 ± 0.005	16.188 ± 0.005	16.514 ± 0.004	18.262 ± 0.007
8508.916	15.936 ± 0.004	16.198 ± 0.004	16.525 ± 0.004	18.254 ± 0.007
8518.847	15.855 ± 0.005	16.260 ± 0.007	16.552 ± 0.009	18.208 ± 0.018
8518.848	15.971 ± 0.007	16.211 ± 0.008	16.477 ± 0.009	18.242 ± 0.020
8518.848	15.912 ± 0.005	16.191 ± 0.006	16.545 ± 0.009	18.222 ± 0.017
8520.833	15.968 ± 0.003	16.226 ± 0.004	16.509 ± 0.006	18.239 ± 0.012
8520.834	15.937 ± 0.005	16.196 ± 0.006	16.521 ± 0.008	18.257 ± 0.014
8520.834	15.900 ± 0.007	16.110 ± 0.007	16.630 ± 0.011	18.245 ± 0.023
8525.846	15.948 ± 0.014	16.212 ± 0.015	16.531 ± 0.013	18.228 ± 0.017
8525.847	15.956 ± 0.007	16.209 ± 0.008	16.527 ± 0.007	18.230 ± 0.012
8525.848	15.991 ± 0.014	16.255 ± 0.014	16.541 ± 0.013	18.223 ± 0.016
8537.850	15.926 ± 0.004	16.199 ± 0.005	16.559 ± 0.006	18.218 ± 0.010
8537.851	15.944 ± 0.005	16.173 ± 0.004	16.555 ± 0.006	18.238 ± 0.012
8537.852	15.957 ± 0.003	16.191 ± 0.005	16.518 ± 0.005	18.269 ± 0.009
8541.880	15.948 ± 0.007	16.175 ± 0.007	16.509 ± 0.009	18.206 ± 0.018
8541.880	15.915 ± 0.005	16.190 ± 0.006	16.508 ± 0.007	18.199 ± 0.018
8541.881	15.925 ± 0.004	16.184 ± 0.003	16.514 ± 0.005	18.221 ± 0.013
8547.856	15.955 ± 0.005	16.202 ± 0.007	16.557 ± 0.009	18.209 ± 0.018
8547.857	15.964 ± 0.006	16.233 ± 0.007	16.506 ± 0.008	18.197 ± 0.018
8547.857	15.955 ± 0.005	16.198 ± 0.006	16.552 ± 0.005	18.236 ± 0.012
8556.849	15.943 ± 0.017	16.393 ± 0.031	16.295 ± 0.018	18.458 ± 0.092
8556.850	15.941 ± 0.008	16.182 ± 0.010	16.453 ± 0.012	18.196 ± 0.046
8556.851	15.956 ± 0.007	16.193 ± 0.007	16.521 ± 0.010	18.212 ± 0.027
8564.842	15.942 ± 0.011	16.203 ± 0.012	16.523 ± 0.012	18.227 ± 0.035
8564.843	15.965 ± 0.006	16.203 ± 0.008	16.534 ± 0.011	18.357 ± 0.033
8564.843	15.952 ± 0.009	16.204 ± 0.009	16.520 ± 0.010	18.164 ± 0.024

Note. The Modern Julian Days (MJD) column gives the date of observation relative to MJD = 50 000.